

Aus dem Bereich der Molekularen Zellbiologie
Theoretische Medizin und Biowissenschaften
der Medizinischen Fakultät
der Universität des Saarlandes, Homburg/Saar

Cardiac Calcium-Induced Calcium Release Failure Recordings, Analysis and Its Prevention

*Dissertation zur Erlangung des Grades eines
Doktors der Naturwissenschaften*
der Medizinischen Fakultät
der UNIVERSITÄT DES SAARLANDES

2011

vorgelegt von: Qinghai Tian

geb. am: 26.01.1980 in Liyi, Shangdong, China

Qinghai Tian

Institut für Molekulare Zellbiologie

Kirrbergerstr. Geb. 61

66424 Homburg/Saar, Deutschland

E-Mail: qinghai.tian@uniklinikum-saarland.de

敬献给我亲爱的父母

To my beloved parents

Zusammenfassung

Das Herz ist das Organ, welches das Blut rhythmisch durch den Körper pumpt. Wie entsteht der Herzschlag? Was passiert, wenn sich eine Herzkrankheit entwickelt? Und wie kann diese Fehlfunktion verhindert werden? In dieser Dissertation habe ich mich mit 3 Fragestellungen aus diesem Themenbereich befasst: i) Wie kann die Verlängerung des Aktionspotenzials durch ungeeignete Medikamentenanwendung schnell identifiziert werden? ii) Was passiert während der Umbauprozesse von isolierten Kardiomyozyten und wie können sie verhindert werden? und iii) Wie können Veränderungen der Erregungs-Kalzium-Kontraktions Kopplung in erkrankten Kardiomyozyten optisch identifiziert werden?

Die Beurteilung der Verlängerung von Aktionspotenzialen oder QT-Intervall Screens gewinnen zunehmend an Bedeutung für die Herz bezogene Sicherheit von allen neuen Medikamenten. Bisher wurden Effekte von Medikamenten nur an heterolog exprimierten hERG-Kanälen in immortalisierten Zelllinien untersucht, was einen hohen Grad der Automatisierung erlaubt, aber die Untersuchung auf ein einzelnes Protein limitiert. Durch Untersuchungen an primär isolierten adulten Kardiomyozyten können potentielle Probleme mit neuen Medikamenten besser abgeschätzt werden. Demgegenüber können adulte Kardiomyozyten nicht von automatisierten Patch-clamp Messstationen gehandhabt werden. Einige optische Spannungssensoren wurden bereits für ratiometrische Messungen beschrieben, aber beeinflussten immer das native Aktionspotenzial der Zellen. Die erste Fragestellung, die ich in dieser Dissertation betrachte, ist die Untersuchung der Aufnahmebedingungen und die Bestimmung der experimentellen Parameter, die optische QT-Intervall Screens ermöglichen. Meine Schlussfolgerung ist, dass optische QT-Screens einen Großteil an aufwändigen Tierversuche ersetzen können.

Kardiomyozyten durchlaufen signifikante Umbauprozesse, sowohl während der Entstehung von Krankheiten, als auch nach der Isolation vom Herzgewebe in vitro, was beispielsweise zum funktionellen Verlust in der Kalziumregulation führt. Untersuchungen der Umbauprozesse während der Kultur können Anhaltspunkte für das Verständnis ähnlicher Prozesse während der Entstehung von Krankheiten liefern. Durch die Evaluation der Effekte von Cytochalasin D (CytoD)

auf die elektrophysiologischen Eigenschaften und die Kalziumhomöostase ventrikulärer Myozyten, konnte ich eine optimale CytoD Konzentration herausfinden, welche sowohl die T-tubuläre Struktur als auch die wichtigsten funktionellen Charakteristika, wie Aktionspotenzial, Kalziumtransienten und vor allem auch die kontraktile Eigenschaften einzelner Myozyten über 3 Tage in Kultur erhält. Die optimierte CytoD Konzentration erhält auch die Architektur der Aktinfilamente, das T-tubuläre System und die synchronisierte Kalziumfreisetzung von ventrikulären Myozyten in Kultur. Diese Ergebnisse legen eine mögliche Verbindung zwischen der Zerstörung des Zytoskeletts und dem Umbau der T-Tubuli nahe und erlauben Einsichten in pathologische Prozesse im kranken Herzen.

Echtzeitaufnahmen schneller subzellulärer Kalziumfreisetzungseignisse in 2 Raumdimensionen haben zu bedeutenden Einsichten geführt und unser Verständnis solcher elementarer Prozesse stark gefördert. Allerdings hat das auch zu so hohen Aufnahmezeiten geführt, in denen das Rauschen zur Limitierung für die Interpretation der Daten wurde. Hier schlage ich einen Pixel-basierten Anpassungsansatz zur Datenanalyse von sehr schnellen konfokalen Kalziumaufnahmen vor, welcher erlaubt, Informationen zur zweidimensionalen Kalzium-induzierten Kalziumfreisetzung zu extrahieren. Dieser Ansatz ermöglicht uns bedeutende Fragen der kardialen Erregungs-Kontraktions Kopplung, wie die Arrhythmie bedingenden Vorläufer der mikroskopischen Kalziumalternanz, in Angriff zu nehmen. Der Pixel basierte Anpassungsansatz kann uns helfen, die aktuellen technischen Beschränkungen in der schnellen Lebendzellmikroskopie zu überwinden.

Abstract

The heart is the organ that beats rhythmically to pump blood throughout the entire body. How is the heart beat generated? What will happen if a heart develops diseases? And how can these dysfunctions be prevented? In this thesis I addressed three issues concerning these questions: i) how to quickly identify a prolongation of action potentials induced by inappropriate drug administrations? ii) what is occurring during the remodeling process of the isolated cardiomyocytes and how to prevent that? and iii) how to optically identify alterations of excitation-calcium-contraction coupling in the diseased cardiomyocytes?

Prolongation assessments of action potential, or QT-interval screens, are increasingly important for cardiac safety on all new medications. So far, effects of drugs are investigated only on heterologously expressed hERG K⁺ channels in immortalized cell lines, which allows for a high degree of automation but is limited to only one protein. Investigations with isolated primary adult cardiomyocytes can better predict the potential issues of new drugs. However, adult cardiomyocytes can not be handled by automated patch-clamp equipment. Several optical voltage sensors have been reported for ratiometric measurements of action potentials, but they all influenced the naive action potential. The first issue I intended to address in this thesis was to explore the recording conditions and define experimental settings that allowed optical QT-interval screens. My conclusion was that optical QT-screens can save lots of efforts that are needed in the intricate evaluations on animals.

Cardiomyocytes undergo significant remodeling during both the developments of diseases and in vitro culture, which, e.g. leads to a functional loss of calcium handling. Investigation of the remodeling processes during culture might provide some clues for the understanding of the processes in the disease development. By evaluating the effects of Cytochalasin D (CytoD) on the electrophysiological properties and calcium cycling of the ventricular myocytes, I figured out an optimized CytoD concentration to preserve the major functional characteristics of these cells, such as action potentials, calcium transients and importantly also the contractile properties of single myocytes over three days of culture. The optimized concentration of CytoD also preserved

the actin filament architecture, the T-tubule system, and the synchronous calcium release of ventricular myocytes in culture. These observations proposed a putative link between cytoskeleton disruption and T-tubular remodeling and shed light on the pathological processes inside the diseased hearts.

Real-time imaging of fast subcellular calcium release events in two spatial dimensions has yielded important insight and has greatly fostered our understanding of such elementary processes. However, it has also pushed the acquisition speeds to a level at which the noise has become limiting for the interpretation of the data. Here, I proposed a pixel-wise fitting approach of data analysis for high-speed confocal calcium data, which allows the extraction of two-dimensional calcium-induced calcium release information. This approach enabled us to tackle important questions of cardiac excitation-contraction coupling like the arrhythmogenic precursors of microscopic calcium alternans. The pixel-wise fitting approach may thus help to overcome the present technical limitations in high-speed live cell imaging.

Contents

Zusammenfassung	i
Abstract	iii
Contents	v
List of Figures	x
List of Tables	xii
List of Abbreviations	xiii
1 Introduction	1
1.1 Cardiac action potential and its underlying channels	1
1.1.1 Na ⁺ /K ⁺ -ATPase and resting membrane potential	2
1.1.2 Cardiac Na ⁺ channel and rapid membrane depolarization	3
1.1.3 Cardiac Ca ²⁺ channel and Ca ²⁺ -induced Ca ²⁺ release (CICR)	4
1.1.4 Cardiac K ⁺ channels and membrane repolarization	5
1.1.4.1 The transient outward current (I _{to})	5
1.1.4.2 The ultrarapid delayed rectifier K ⁺ current (I _{Kur})	6
1.1.4.3 The rapid delayed rectifier K ⁺ current (I _{Kr})	6
1.1.4.4 The slow delayed rectifier K ⁺ current (I _{Ks})	7
1.2 Cardiac Ca ²⁺ cycling	7
1.2.1 Ryanodine receptor (RyR)	8
1.2.2 Sarco/Endoplasmic Reticulum Ca ²⁺ -ATPase (SERCA)	10
1.2.3 Na ⁺ /Ca ²⁺ Exchanger (NCX)	10
1.2.4 Cardiac Ca ²⁺ cycling and Ca ²⁺ alternans	11
1.3 T-tubule membrane system and EC-coupling	12
1.4 Interactions between extracellular matrix, Z-disk and F-actin	13
1.5 Optical action potential measurements	14

1.6	The effects of CytoD in the culture of cardiomyocytes	16
1.7	Computer-aided analysis of cardiac Ca^{2+} signaling	17
2	Materials and Methods, Instruments and Data Analysis	19
2.1	Materials and Methods	19
2.1.1	Materials	19
2.1.2	Adult rat ventricular cardiomyocytes isolation	19
2.1.3	Adult mouse cardiomyocyte isolation	20
2.1.4	Neonatal rat cardiomyocyte isolation	21
2.1.5	Fura-2-based Ca^{2+} transient measurements	22
2.1.6	Indo-1-based Ca^{2+} transient measurements with caffeine	22
2.1.7	Fluo-4-based confocal Ca^{2+} measurements	23
2.1.8	The construction of adenovirus-based mermaid	24
2.1.9	Optical measurements of action potential	24
2.1.9.1	Di-8-ANEPPS-based measurements	24
2.1.9.2	Mermaid-based measurements	25
2.1.10	Emission spectrum measurements	25
2.1.10.1	Emission spectrum measurements of di-8-ANEPPS with KCNH2 cells	25
2.1.10.2	Emission spectrum measurements of Mermaid with COS cells	25
2.1.11	Patch-clamp measurements	25
2.1.12	Actin staining	26
2.1.13	T-tubule visualization	27
2.1.14	Sarcomere length measurements	27
2.2	Instruments	27
2.2.1	Imago video-imaging microscope	27
2.2.2	Retiga video-imaging microscope	27
2.2.3	Photodiode-based photometry setup	28
2.2.4	Leica TCS SP5 confocal microscope	29
2.3	Data Analysis	29
2.3.1	3D surface reconstruction	29
2.3.2	Optical AP duration analysis	29
2.3.3	Analysis of Ca^{2+} transients	29
2.3.4	Analysis of confocal line-scan images	30

2.3.5	Surface plotting	30
2.3.6	Analysis of T-tubule structure and actin staining	30
2.3.7	Data statistics	30
3	Results	31
3.1	Optical action potential measurements	31
3.1.1	Spectral properties of di-8-ANEPPS	31
3.1.2	Properties of the measurement system	31
3.1.3	Quantum efficiency	32
3.1.4	Evaluation of di-8-ANEPPS	34
3.1.5	Characterization of action potential prolongation in adult and neonatal cardiomyocytes induced by drugs	35
3.1.5.1	Traditional strategy of substance evaluation	36
3.1.5.2	Well-to-well strategy of substance evaluation	36
3.1.5.2.1	Substance evaluation with adult rat cardiomyocytes	37
3.1.5.2.2	Substance evaluation with neonatal rat cardiomyocytes	38
3.1.5.2.3	Summary of the application of di-8-ANEPPS	38
3.1.6	Properties of Mermaid and its application on rat adult cardiomyocytes	38
3.1.6.1	Protein structure and working principle	39
3.1.6.2	Expression pattern of Mermaid on rat ventricular myocytes	40
3.1.6.3	The response of mermaid to action potentials	42
3.1.6.4	Kinetic comparison of di-8-ANEPPS and Mermaid	43
3.1.7	Final remarks for this section	45
3.2	The effects of CytoD in the culture of cardiomyocytes	45
3.2.1	Dynamic changes of Ca ²⁺ transients of cardiomyocytes during long-term culture	45
3.2.2	Culture-mediated changes in Ca ²⁺ transients can be prevented by CytoD	46
3.2.3	Concentration-dependent action of CytoD on Ca ²⁺ cycling in adult cardiomyocytes	48
3.2.3.1	Concentration-dependent effects of CytoD on Ca ²⁺ cycling during 6 days of culture	48
3.2.3.2	Thorough investigation of the effects of 0.5 μM CytoD on cardiac Ca ²⁺ cycling	48

3.2.4	Optimized concentration of CytoD preserved the contraction of cardiomyocytes in culture	50
3.2.5	Effects of the optimized CytoD concentration on cardiac Ca^{2+} signaling . .	50
3.2.6	The optimized concentration of CytoD preserved the T-tubule membrane system in culture	53
3.2.7	CytoD prevented actin filaments reorganization during culture	54
3.2.8	Effects of CytoD on subcellular properties of Ca^{2+} release	56
3.2.9	Final remarks for this section	58
3.3	Computer-aided CICR analysis	58
3.3.1	Theoretical analysis of CICR signal	58
3.3.1.1	Components of measured signal	58
3.3.1.2	Global Ca^{2+} transient	59
3.3.1.3	Description of local Ca^{2+} transients	60
3.3.1.3.1	Fitting with GauConvExp	61
3.3.1.3.2	Fitting with ExpConvExp	62
3.3.1.3.3	Fitting with ExpConvdbExp	62
3.3.2	Fitting Strategies	63
3.3.3	High speed 2D imaging of cardiac Ca^{2+} imaging	64
3.3.4	Pixel-wise fitting	65
3.3.4.1	Comparison of different mathematical functions	65
3.3.4.2	Fitting results with ExpConvdbExp function	66
3.3.4.3	Pixel-wise reconstruction	67
3.3.4.4	Contraction perturbation	68
3.3.4.5	Reproducibility of pixel-wise fitting	69
3.3.5	Application of “pixel-wise” fitting in the study of subcellular cardiac Ca^{2+} signaling	71
3.3.5.1	Atrial myocyte EC-coupling	71
3.3.5.2	Reconstruction of the plasma membrane	72
3.3.5.3	Identification of EC-coupling sites	72
3.3.5.4	Analysis of membrane-CICR properties	73
3.3.6	RacET atrial myocyte displayed CICR failure	73
3.3.7	The role of subcellular Ca^{2+} handling for cardiac alternates	75
3.3.7.1	Rat ventricular CICR stability and algorithm reliability	75
3.3.7.2	CICR dynamics after acceleration of the stimulation	76

3.3.7.3	Subcellular Ca^{2+} handling in Ca^{2+} alternans	77
3.3.8	Final remarks for this section	80
4	Discussion	81
4.1	Optical recordings of action potential	81
4.1.1	Validated improvements	81
4.1.2	Comparison of adult with neonatal ventricular myocytes in QT-screen	82
4.1.3	Benefits of genetically encoded membrane potential sensors	83
4.1.4	Further perspectives about optical AP recordings	83
4.2	The effects of CytoD in the culture of cardiomyocytes	84
4.2.1	Rat ventricular myocytes undergo remodeling after isolation	84
4.2.2	Improved culture of adult cardiomyocytes with CytoD	86
4.2.3	Possible mechanisms underlying CytoD effects	87
4.2.4	CytoD as a pharmacological tool to study cardiomyocyte remodeling	88
4.2.5	Summary and perspectives	89
4.3	Computer-aided cardiac CICR analysis	89
4.3.1	High-speed/resolution confocal Ca^{2+} imaging and inherent problems	89
4.3.2	Algorithm design of “pixel-wise fitting”	89
4.3.2.1	Design of mathematical function for rodent cardiac Ca^{2+} transient	90
4.3.2.2	Reliability, reproducibility, extendability, efficiency and limitations of the fitting strategy	91
4.3.3	Biological relevance	92
4.3.4	Case study: role of Rac1 in left atrial EC-coupling	93
4.3.5	Case study: dynamics of ventricular Ca^{2+} handling	94
4.3.6	Summary and perspectives	96
	References	97
	Appendix A: Publications	119
	Appendix B: Acknowledgment	120
	Appendix C: Attachments	121

List of Figures

1.1	The excitation-calcium-contraction coupling in rodent cardiomyocytes	2
1.2	The interplay of cardiac ion channels during action potential	2
1.3	Cardiac Ca^{2+} cycling	8
1.4	Organization of SR, T-tubule and cytoskeleton	12
1.5	Interactions between Z-disk, costamere and ECM	14
2.1	Typical Ca^{2+} transient recording	22
2.2	Typical caffeine-induced Ca^{2+} transient recording	23
2.3	The design of imaging setups	28
3.1	Spectral properties of di-8-ANEPPS	32
3.2	Optical action potential measurement of di-8-ANEPPS loaded cardiomyocytes	33
3.3	Evaluation of di-8-ANEPPS-based measurements	35
3.4	Compounds structure	36
3.5	Problems in traditional strategy of substance evaluation	37
3.6	Well-to-well strategy of substance evaluation with adult myocytes	37
3.7	Comparison of neonatal and adult ventricular myocytes	39
3.8	Well-to-well strategy of substance evaluation with neonatal myocytes	39
3.9	The structure of Mermaid and its working principle	41
3.10	The expression pattern of Mermaid on ventricular myocytes	41
3.11	Comparison of Mermaid and di-8-ANEPPS emission spectra	42
3.12	Colocalization of Mermaid and di-8-ANEPPS	43
3.13	The response of Mermaid to action potentials	44
3.14	Comparison of di-8-ANEPPS and Mermaid kinetics	44
3.15	Dynamic changes of Ca^{2+} transients of cardiomyocytes during culture	46
3.16	Effects of CytoD (40 μ M) on Ca^{2+} transients and on membrane topology	47
3.17	Concentration response of CytoD effects on cardiac Ca^{2+} transients	49

3.18 The effects of optimal CytoD on Ca^{2+} transients	49
3.19 Effects of the optimal CytoD on the contraction of cardiomyocytes	51
3.20 Effects of the optimal CytoD on the components of Ca^{2+} cycling	52
3.21 Effects of the optimized CytoD concentration on T-tubule remodeling	54
3.22 The effects of CytoD on cardiac cytoskeleton	55
3.23 CytoD effects on subcellular Ca^{2+} release	57
3.24 Illustration of the principal strategy of model-based fitting	59
3.25 Local Ca^{2+} transient events	60
3.26 Algorithm work-flow chart for ExpConvdbExp function	63
3.27 Raw data example from high resolution imaging on confocal microscope	64
3.28 Pixel-wise fitting with different mathematical functions	66
3.29 Pixel-wise fitting of Ca^{2+} transients	67
3.30 Comparison of raw and reconstruction of Ca^{2+} transients	68
3.31 Temporally unlimited interpolation of Ca^{2+} transients	69
3.32 Contraction effects on ExpConvdbExp-based pixel-wise fitting	69
3.33 Reproducibility of pixel-wise fitting	70
3.34 Flow chart of membrane-CICR coupling analysis	71
3.35 Normalization of membrane staining	72
3.36 Identification of CICR sites	72
3.37 RacET atrial myocyte displayed CICR failure	74
3.38 Rat ventricular CICR stability	76
3.39 CICR dynamics upon pulse acceleration	77
3.40 Analysis of Ca^{2+} alternans with pixel-wise fitting	79

List of Tables

3.1	Effects of test compounds on APs in cardiomyocytes	40
3.2	Reproducibility of pixel-wise fitting	70
3.3	Coupling analysis of CICR-membrane for RacET myocytes	75

List of Abbreviations

[Ca ²⁺] _i	Intracellular Ca ²⁺ concentration
a.u.	Arbitrary Unit
AP	Action Potential
APD	Action Potential Duration
Ca ²⁺	Calcium ion
CaMKII	Calmodulin-dependent Protein Kinase II
CCD	Charge-Coupled Device
CICR	Ca ²⁺ -induced Ca ²⁺ Release
CPVT	Catecholaminergic Polymorphic Ventricular Tachycardia
CytoD	Cytochalasin D, an alkaloid produced by <i>Helminthosporium</i> and other molds.
DAD	Delayed Afterdepolarizations
DIV	Day In Vitro
E _m	Membrane potential
EAD	Early Afterdepolarizations
EC-coupling	Excitation-Contraction coupling
ECG	Electrocardiogram
ECM	Extracellular Matrix
FFT	Fast Fourier Transform

Fluo-4/AM	Fluo-4-acetoxymethyl ester
Fura-2/AM	Fura-2-acetoxymethyl ester
HEPES	4-(2-hydroxyethyl)-1-piperazineethanesulfonic acid
hERG	Human <i>Ether-à-go-go</i> Related Gene
HTS	High Throughput Screening
i.p.	Intraperitoneal injection
Indo-1/AM	Indo-1-acetoxymethyl ester
JP-2	Junctophilin type 2
K ⁺	Potassium ion
LQTS	Long QT Syndrome
LTCC	L-type Ca ²⁺ Channel
ms	Millisecond
Na ⁺	Sodium ion
NCX	Sodium/Calcium Exchanger
PKA	Protein Kinase A
PMT	Photo Multiplier Tube
QRS	The Q, R, and S waves in ECG
qSAR	quantitative Structure-Activity Relationship
QT-interval	Time between the start of the Q wave and the end of the T wave in ECG
RacET	A mouse strain that constitutively expresses Rac1 protein in the heart.
RyR	Ryanodine Receptor
SERCA	Sarco/Endoplasmic Reticulum Ca ²⁺ -ATPase
SN	Signal-to-Noise Ratio
SR	Sarcoplasmic Reticulum

STED	Stimulated Emission Depletion microscopy
TdP	Torsade de Pointes
VSD	Voltage Sensitive Domain
WT	Wild Type mouse strain

Chapter 1

Introduction

The heart pumps blood rhythmically to ensure circulation throughout the entire body, supplying oxygen (O_2) and nutrients while removing metabolic wastes and carbon dioxide (CO_2). The entire blood circulation is driven by a well-coordinated heart beat generated by the four chambers of the heart, which are made up of cross-striated muscle, the myocardium. The initiating event in a heart beat is an electrical stimulus, the action potential (AP), which is primarily generated by the pacemaker cells located in the Sinoatrial Node (SA Node). The SA Node cells undergo spontaneous depolarization regularly, and the following excitation wave proceeds via gap junctions from cell to cell. For this the depolarizing current spreads from one cell to another, pushing the membrane potential (E_m) of the latter cell beyond the threshold for an AP¹⁵. This excitation wave propagates through the atria, to the Atrioventricular Node (AV Node), and finally via the His-Purkinje conduction system to the ventricle in a well-coordinated manner¹³⁰.

During the AP, Ca^{2+} ions flow into cardiomyocytes which will induce Ca^{2+} release from the intracellular Ca^{2+} -storing organelle, the sarcoplasmic reticulum (SR), and leads to an increase of the intracellular Ca^{2+} concentration ($[Ca^{2+}]_i$). This transient $[Ca^{2+}]_i$ increase induces rhythmic actin/myosin interaction, which results in cardiomyocyte shortening and subsequent myocardium contraction. The entire process, from the AP to the Ca^{2+} transient, and finally to the contraction, is referred to excitation-contraction coupling (EC-coupling)¹⁴, as illustrated in figure 1.1.

1.1 Cardiac action potential and its underlying channels

The AP is a membrane potential waveform that is determined by a complex interplay of many ion channels and transporters, such as Na^+ channels, K^+ channels, Ca^{2+} channels, Na^+/K^+ -ATPase and Cl^- channels, as shown in figure 1.2, which will be discussed in the following.

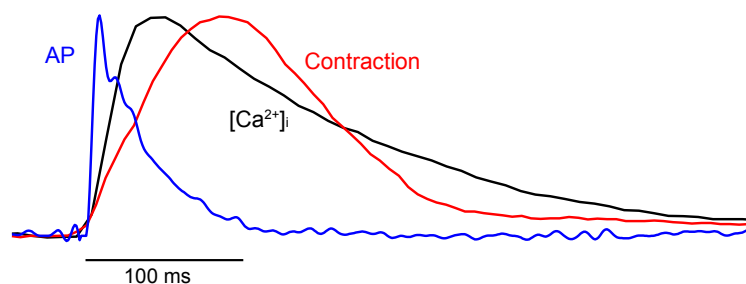


Figure 1.1: The excitation-calcium-contraction coupling in rodent cardiomyocytes. All the data, including action potential signal (blue, labeled as “AP”), $[Ca^{2+}]_i$ signal (black) and contraction (red) were measured optically on rat adult ventricular myocytes. Both the optical AP and $[Ca^{2+}]_i$ measurements in cardiomyocytes will be discussed in this thesis.

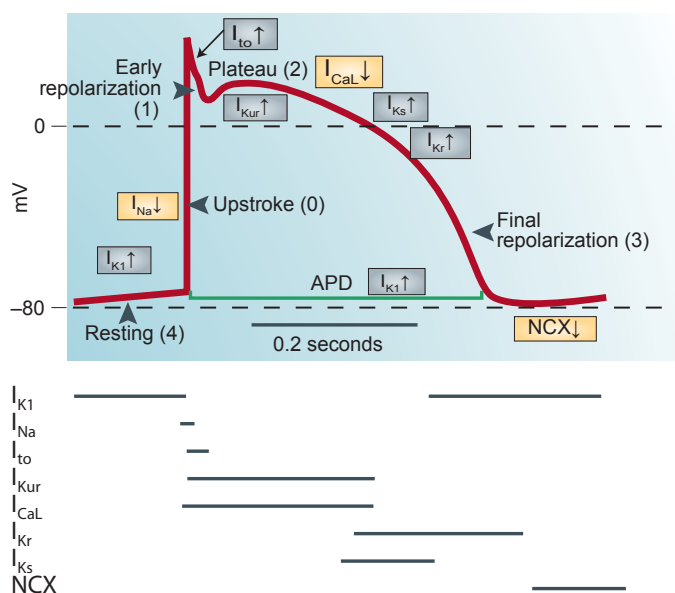


Figure 1.2: The interplay of cardiac ion channels during action potential for a typical human ventricular cell. The five phases of an AP are also labeled out with their traditional names. I_{K1} , intermediate conductance K^+ current contributed by Kir2.1 channels; I_{to} , transient outward K^+ channel current; I_{Kur} , ultra-rapid delayed rectifier K^+ channel current; I_{CaL} , L-type Ca^{2+} channel current; I_{Ks} , slow delayed rectifier K^+ channel current; I_{Kr} , rapid delayed rectifier K^+ channel current; I_{Na} , Na^+ channel current; I_{CaL} , L-type Ca^{2+} channel current; NCX, Na^+/Ca^{2+} Exchanger channel current. Taken from Nattel et. al, Nat Rev Drug Discov, 2006, 5:1034-1049¹⁴⁶ with some modifications.

1.1.1 Na^+/K^+ -ATPase and resting membrane potential

The Na^+/K^+ -ATPase is made up of two subunits, a catalytic α subunit that couples ATP hydrolysis to ion transport and a glycoprotein β subunit responsible for maturation, assembly, and membrane targeting of the Na^+/K^+ -ATPase¹⁵⁷. So far, four α -subunit isoforms and at least three β -subunit isoforms of the Na^+/K^+ -ATPase have been identified in mammals. Of the 4 α -isoforms, $\alpha 1$ predominates in cardiac cells, especially in rodent hearts¹⁵⁷. It is widely reported that the Na^+/K^+ -ATPase is regulated by the cAMP-Protein Kinase A (PKA) signaling cascade, which is initiated by the ac-

tivation of the sympathetic nervous system via cardiac β -adrenergic receptors and subsequent cAMP formation²¹⁰.

At the resting state of the action potential, Na^+/K^+ -ATPase consumes 20 ~ 30% of the cellular ATP production to actively transport 3 Na^+ out of and 2 K^+ into the cell, which establishes and maintains the electrochemical gradients for both Na^+ and K^+ .

Since the resting membrane is preferentially permeable to K^+ , the membrane potential can be calculated according to the Nernst equation,

$$E_m = \frac{RT}{zF} \ln \left(\frac{[\text{K}]_o}{[\text{K}]_i} \right) = -89 \text{ mV} \quad (1.1)$$

In practice, the membrane of cardiomyocyte is also permeable, although to a much less degree, to the Na^+ , Ca^{2+} and Cl^- , resulting in a resting membrane potential of about -82 mV¹⁵.

The Na^+ gradient across the cell membrane maintained by the Na^+/K^+ -ATPase enables the rapid upstroke of the action potential. It is also very important in other cell functions, such as maintaining cell volume, and secondary active transport of other solutes, e.g., the transcellular transport processes in intestine, glands, and kidney.⁹⁸

1.1.2 Cardiac Na^+ channel and rapid membrane depolarization

Cardiac Na^+ channels belong to the voltage-dependent Na^+ channel family and usually consist of a transmembrane pore-forming α -subunit and an ancillary modulatory β -subunit. The primary α -subunit of hNav1.5, which is encoded by the SCN5A gene and expressed specifically in the heart, is made up of four internally homologous domains (DI-DIV), each of which consists of six transmembrane α -helical segments (S1 to S6)¹⁷². Segments S5 and S6 form the ion pore for each domain, and the segment S4 is positively charged and responsible for the voltage sensing. The β_1 -subunit increases the level of protein expression on cell membrane and alters the gating of neuronal Na^+ channel, but remains elusive for the cardiac Na^+ channel.

The Na^+ channel plays a central role in the excitability of cardiomyocytes and proper conduction of the electrical impulse within the heart. When the membrane rapidly depolarizes from resting potential (-82 mV) towards about -50 mV, the Na^+ channel will be the first channel to be activated during the AP. An influx of Na^+ ions commences, thereby further depolarizing the cell membrane during AP overshoot, and ultimately brings E_m to about +20 mV.

Gene mutations in cardiac Na^+ channels have been associated with long QT syndrome (LQTS), Brugada syndrome, and some diseases in primary cardiac conduction system⁶⁷. LQTS is a multi-loci congenital (and acquired) cardiac disorder characterized by a prolonged rate corrected QT

interval inducing syncope and risk of sudden death. In type 3 of LQTS, mutations that suppress fast Na⁺ channel inactivation result in a population of channels entering a gating mode with recurrent openings throughout the AP plateau, and thus prolong action potential duration (APD)^{56,174,226}. The Brugada syndrome is a genetic disease that is characterized by abnormal electrocardiogram (ECG) findings and an increased risk of sudden cardiac death. Reduced activity or loss-of-function of Na⁺ channels will result in Brugada syndrome^{31,38}. Drugs that block Na⁺ channels, such as flecainide and encainide, can produce marked heterogeneity of APDs, which increases the mortality in patients after myocardial infarction⁹⁵.

Antiarrhythmic agents are a group of pharmaceuticals that are used to suppress cardiac arrhythmias. According to the Singh Vaughan Williams classification, these antiarrhythmic agents have been classified into five classes based on the primary mechanisms of their antiarrhythmic effects. Quinidine is one of the class I antiarrhythmic agents that primarily blocks the fast inward Na⁺ current (I_{Na}) and results in decreased depolarization (decreased V_{max}) in the upstroke phase (figure 1.2). Quinidine has been used successfully to treat idiopathic ventricular fibrillation, Brugada syndrome, and Short QT syndrome²⁴².

1.1.3 Cardiac Ca²⁺ channel and Ca²⁺-induced Ca²⁺ release (CICR)

Cardiac Ca²⁺ channels usually comprise three different subunits, the primary α_1 -subunit, the ancillary β -subunit and $\alpha_2\delta$ -subunit²². Two α_1 -subunit isoforms have been identified in the heart, the α_1C -subunit for the L-type Ca²⁺ channel (LTCC, long lasting) and the α_1H -subunit for T-type (high threshold or tiny) channel. LTCC is expressed throughout the heart, while the T-type channel is limited to SA node, AV node, atrium and specialized conducting system¹⁵⁰. The β -subunits have some ancillary functions, such as trafficking of α -subunit proteins and facilitating the activation and inactivation of the channels, etc. The $\alpha_2\delta$ -subunit may help α_1 -subunits to locate onto the cell membrane¹⁷⁴.

Just like the cardiac Na⁺ channel α -subunit, the α_1C -subunit contains four motifs (I-IV) and every motif is made of six transmembrane segments (S1-S6). The S4 segment is responsible for voltage sensing, S5 and S6 are the pore-forming segments. The α -interaction domain (AID) where the β -subunit binds locates between motif I and II. Those regulatory sites, including Ca²⁺-dependent inactivation, channel facilitation and PKA phosphorylation, can be found in the C-terminal part of the channel²².

LTCCs have multiple functions during an AP. When the depolarization during the AP reaches voltages positive to around -30 mV, Ca²⁺ channels open and gate Ca²⁺ into the cytosol, which prolongs the AP plateau. In addition this initial rise in cytosolic Ca²⁺ triggers further release

of Ca^{2+} from the intracellular Ca^{2+} storing organelle, the SR. This process is referred as Ca^{2+} induced Ca^{2+} release (CICR) and will be discussed in more details below.

LTCCs have also been related to arrhythmia. AP prolongation can increase the amplitude of the Ca^{2+} transient, activating CaM kinases that subsequently phosphorylate LTCCs⁴, and thus promote arrhythmogenic early afterdepolarizations (EAD) and delayed afterdepolarizations (DAD)¹³¹. Supportive evidence for such a process comes from a mutation G406R in the α_1 -subunit (CaV1.2) that produces maintained inward Ca^{2+} currents by a nearly complete loss of voltage-dependent channel inactivation. This delays AP repolarization and increases the risk of arrhythmia²⁰².

1.1.4 Cardiac K^+ channels and membrane repolarization

During the cardiac AP there are four types of voltage-gated K^+ channels that contribute to outward repolarization currents, comprising a transient outward current (I_{to}) and three delayed rectifier currents (I_{Kur} , I_{Kr} and I_{Ks}). Those K^+ channels control the amplitudes and durations of action potentials in the myocardium and are primary determinants of the AP repolarization (figure 1.2). They will be introduced in the following.

1.1.4.1 The transient outward current (I_{to})

Rapidly activating and inactivating transient outward K^+ currents (I_{to}) are identified in most mammalian cardiomyocytes. Molecular and biophysical analysis have identified two pore-forming subunits, Kv4.2 and Kv4.3, for the fast component of I_{to} ($I_{\text{to,f}}$), and one (Kv1.4) for the slow component. Several β -subunits and interacting proteins, including the Kv Channel-Interacting Protein 2 (KChIP2) and the major iron-regulated protein (MiRP) subfamily (MiRP1 and MiRP2) have also been identified and play an important role in regulating I_{to} . These molecular basics, their related physiological roles and mechanisms have been reviewed thoroughly recently¹⁴⁷.

In most species, I_{to} plays a pivotal role in the early phase of action potential repolarization (Phase 1 in figure 1.2). In human and canine, I_{to} only partially repolarizes the membrane leading to the phase 2 plateau⁷⁰. In rodents, the expression of I_{to} increases with animal growth^{105,224}. In adulthood, a high density of I_{to} dominates all phases of AP repolarization, and suppresses the rapid component of the delayed rectifier current I_{Kr} , resulting in the characteristic short triangular shape of cardiac action potentials in mice and rats (see figure 1.1)^{148,154}.

I_{to} has been reported to be involved in several heart diseases. A 30% reduction in the mRNA expression and current density of Kv4.3 was found in human heart failure¹⁰². In the Brugada

syndrome, one of the I_{to} regulatory proteins, MiRP, contains mutations, suggesting a contribution of I_{to} in the development of the disease⁵⁴.

I_{to} can be blocked by many anti-arrhythmic agents, such as quinidine, flecainide and propafenone²²⁸. The most common compound is 4-aminopyridine (4-AP), which is usually used to identify I_{to} ¹⁰⁴.

1.1.4.2 The ultrarapid delayed rectifier K^+ current (I_{Kur})

Besides I_{to} , the second type of voltage-activated K^+ channels is the ultrarapid delayed rectifier, I_{Kur} , that is mainly found in human atrium and in rodents. In rat ventricles their expression rapidly decrease postnatally⁷⁵. In adult mice the contribution of I_{Kur} to AP duration appears to be limited⁶⁶. Thus this current is not considered further in this thesis.

1.1.4.3 The rapid delayed rectifier K^+ current (I_{Kr})

I_{Kr} is the major repolarizing current in phase 3 of an AP. The “*ether-à-go-go*” gene, hERG, encodes the pore-forming α -subunit underlying I_{Kr} ¹⁸⁴. hERG K^+ channels contains six transmembrane domains (denoted S1-S6), with a voltage-sensor at S4 domain and the pore-forming domain between S5 and S6¹⁵⁵. hERG also needs a β -subunit to fulfill its function as I_{Kr} -conducting channel. One of those β -subunits is MiRP1, that helps hERG to behave like native cardiac I_{Kr} channels in their gating, unitary conductance, regulation by K^+ , and distinctive biphasic inhibition by the class III antiarrhythmic drug E-4031¹.

The inactivation of hERG K^+ channels is very fast¹⁹⁷, while its deactivation is very slow²⁴⁷. Due to the slow deactivation, hERG channels remain open for tens of milliseconds after AP repolarization, but conduct little current since the electrochemical gradient for K^+ is minimal at the normal resting membrane potential, which can help to suppress succeeded premature AP, and hence arrhythmia²¹⁷.

hERG receives the most interest both from academia and pharmaceutical industry due to its special structure and important functions. Nearly 300 different mutations in hERG have been found in patients with LQTS type 2¹⁶⁰ (See also the Inherited Arrhythmia Database sponsored by Cardiovascular Genetics, New York University). Meanwhile mutations in MiRP1 have also been associated with long QT syndrome and ventricular fibrillation¹. Drug-induced hERG channel blockage also leads to delayed AP repolarization and hence to long QT-intervals, which promotes EADs and a transient functional block of the heart²¹⁷. More than 60 drugs have been reported to induce long QT-intervals and in most cases a “Torsade de Pointes” (TdP) was reported⁸¹.

From this group terfenadine and cisapride have been withdrawn from the market by the Food and Drug Administration (FDA) in the USA because the risk of lethal ventricular arrhythmias was believed to outweigh the pharmacological benefits of these compounds²¹⁷. Drug authorities and pharmaceutical industry now pay more attention to the potential side effects of new drugs^{45,217}.

Great efforts have been dedicated to understand the drug sensitivity of hERG channels. From the structural point of view, the hERG channel has a pore module with a very large cavity, allowing it to accommodate a very large range of compounds or drugs¹⁸⁵. The rapid inactivation of opened hERG channels¹⁹⁷ prevents drug dissociation, thus stabilizes drug binding. Multiple aromatic amino acids surrounding the pore also seem to facilitate high-affinity binding of drugs to the channel^{185,217}.

1.1.4.4 The slow delayed rectifier K⁺ current (I_{Ks})

I_{Ks} is conducted by a channel that is constituted of one α -subunit KvLQT1²²⁵ and one β -subunit MinK¹⁸³. I_{Ks} only contributes a small current to the AP repolarization, but provides an important safety mechanism preventing excessive and dangerous lengthening of repolarization. Therefore, down-regulation, genetic loss of function or pharmacological inhibition of I_{Ks} does not manifest a marked repolarization elongation, but makes the repolarization less stable and the heart vulnerable towards repolarization abnormalities and consequently TdP arrhythmias^{99,173}. Mutations in KvLQT1 have been confirmed to induce long QT syndrome and increase the risk of sudden cardiac death²²⁵.

The interplay of all those ion channels constitutes the complex AP (figure 1.2), which serves as a trigger for subsequent Ca²⁺ release from the SR, finally initiating a contraction. In the last two decades most of the proteins for those currents have been identified and characterized extensively^{67,174}. This has helped a lot in understanding the channelopathy-related cardiac diseases, including genetic mutation or drug induced QT-interval prolongations^{160,217} and arrhythmias¹⁸⁵.

1.2 Cardiac Ca²⁺ cycling

Ca²⁺ is the most ubiquitous second messenger in intracellular signaling cascades and is thus involved in almost all biological processes⁴¹. In the muscle, Ca²⁺ plays another essential role: the activation of contraction. As discussed above, an AP allows for an initial Ca²⁺ influx via LTCC, which in turn induces additional Ca²⁺ release from the SR. For restoration of resting Ca²⁺ concentration, Ca²⁺ will be pumped back into the SR by the Sarcoplasmic/Endoplasmic Reticulum

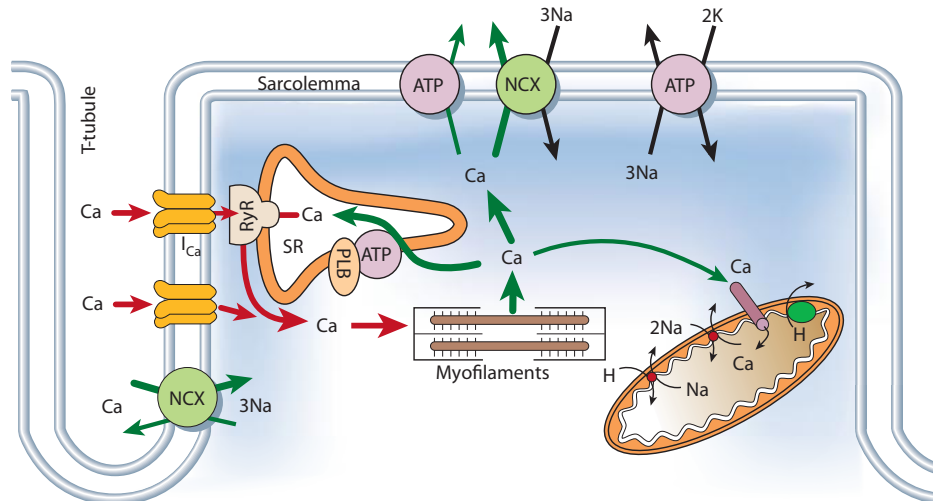


Figure 1.3: Cardiac Ca^{2+} cycling. Taken from Donald M. Bers, *Nature*, 2002, 415:198-205¹⁴ with some modifications. Please refer to the detailed information in the text.

Ca^{2+} -ATPase (SERCA) and transported out of the cell via the $\text{Na}^{+}/\text{Ca}^{2+}$ -Exchanger (NCX)^{14,18}. The entire process is illustrated in figure 1.3, and will be explained in more detail in the following sections.

1.2.1 Ryanodine receptor (RyR)

A steep Ca^{2+} gradient of more than four orders of magnitude across the SR membrane, maintained by the SERCA, allows for rapid intracellular Ca^{2+} increase. The ryanodine receptor (RyR) is the primary cardiac Ca^{2+} release channel located in the SR membrane, via which Ca^{2+} ions diffuse out into the cytosol²⁴⁶.

Three RyR isoforms have been identified and cloned. RyR2 is the predominant isoform in cardiomyocytes¹⁷⁸. On the level of genome, RyR2 consists of 102 exons, encoding a protein of 4967 amino acids. Usually four RyR monomers constitute a homotetramer channel with a molecular mass of about 2200 kDa, which is believed to be the largest ion channel identified so far. Four-fifths of each RyR protein from the amino terminus is cytoplasmic and serves as a scaffold for protein-protein interactions that modulate RyR channel function. The one-fifth from the carboxy terminus forms the luminal and membrane spanning domains with the channel pore module. The region that interlinks the outer cytoplasmic domain to the transmembrane domain undergoes major conformational changes during the opening and closing of the channel¹¹⁷.

Unlike the physical protein-protein interaction between $\text{Ca}_v1.1$ and RyR1 in skeletal muscle, in cardiomyocytes the coupling of $\text{Ca}_v1.2$ (LTCC) and RyR2 relies on spatial proximity between the two proteins. This gap is determined by special proteins, such as junctophilin-2 (JP-2)⁶³.

Usually 10 ~ 25 LTCCs and 100 ~ 200 RyRs are clustered together and constitutes a local Ca²⁺ signaling complex, or couplon¹⁸. Each of these RYR clusters can release Ca²⁺ independently of each other. They are thus called Ca²⁺ release units (CRU). When an AP arrives, LTCCs open, allowing extracellular Ca²⁺ influx that increases the local Ca²⁺ in the cleft between LTCC and RyR to 10 ~ 20 μM. Thereafter, approximately 6 ~ 20 RyRs will open at each couplon, which raises the cleft Ca²⁺ to 200 ~ 400 μM. Ca²⁺ diffuses from the cleft to the cytosol to activate the myofilaments¹⁸. The ratio of the released Ca²⁺ via RyR over the influxed Ca²⁺ via LTCC is usually referred as EC-coupling gain. The rodent EC-coupling gain (~ 13) is much higher than that of human, rabbit and guinea pig (~ 2.3). Every CRU is independent of its neighbors, and for a healthy EC-coupling, all 20000 CRUs in the cell would be activated simultaneously¹⁸.

Beside direct Ca²⁺ activation during CICR, RyR2 can also be modulated by other ions, small molecules and proteins, including ATP, Ca²⁺/calmodulin (CaM), calsequestrin 2 (CSQ2), FKBP 12.6, PKA, Calmodulin-dependent Protein Kinase II (CaMKII), reactive oxygen species and reactive nitrogen species, etc. RyR2 has been reported to bind CaM in a ratio of 1:4 to 1:7. Upon binding, Ca²⁺-dependent RyR2 activation is shifted to a higher Ca²⁺ concentration, which decreases its Ca²⁺ sensitivity¹¹. Reduced CaM-RyR2 affinity promotes spontaneous local Ca²⁺ release, leading to lethal arrhythmias²³⁹. CSQ2 is a RyR binding protein that locates in the SR lumen and acts as Ca²⁺ storage center and Ca²⁺ sensor. It can increase the open probability of RyR2 and thus facilitate Ca²⁺ release during high heart rates²³². Loss of CSQ2 promotes exercise-induced cardiac death caused by polymorphic ventricular tachycardia (CPVT)^{109,164}. FKBP12.6 is another RyR2 high affinity binding protein, which can stabilize the closed state of the channel¹³⁵. FKBP12.6 deficiency results in cardiomyopathy and ventricle septal defects that mimic human congenital heart disorder^{117,190}. RyR2 also forms complexes with PKA and CaMKII, and can be phosphorylated at amino acid S2808 and S2814, respectively, which leads to increased channel activity or open probability of the channel^{227,230,231}, affecting EC-coupling gain. RyRs contain more than 80 cysteines per monomer with approximately 25 ~ 50 in the reduced state. An additional six to eight are considered hyperreactive, making them suitable for modification by reduction/oxidation. Reactive oxygen species, thiol oxidation agents, S-nitrosothiols and NO/ONOO⁻ donor SIN-1 increase RyR channel open probability or stimulate channel activity, while reagents that reduce thiols decrease RyR activity²⁴⁸.

Mutations in RyR2 are also the source of human disease. So far 53 mutations that induce CPVT and 5 mutations that induce arrhythmogenic right ventricular dysplasia type 2 (ARVD2) have been identified^{19,117} (See also the Inherited Arrhythmia Database sponsored by Cardiovascular Genetics, New York University).

1.2.2 Sarco/Endoplasmic Reticulum Ca²⁺-ATPase (SERCA)

SERCA pump is a 110-kDa single transmembrane protein localized in the SR membrane. Three SERCA genes have been identified (SERCA1, SERCA2 and SERCA3), and show a very high homology. SERCA2 encodes two isoforms, SERCA2a (997 aa) and SERCA2b (1042 aa). SERCA2a distributes predominantly in cardiomyocytes, while SERCA2b is expressed in both excitable and non-excitable cells at low levels. Protein crystallization has identified 10 transmembrane motifs (M1 ~ M10) and a cytoplasmic protein anchor domain (A domain), a phosphorylation domain (P domain) and a ATP-binding N-domain¹⁵⁹.

The SERCA pump utilizes the energy derived from ATP hydrolysis to overcome the Ca²⁺ gradient and to transport Ca²⁺ across the SR membrane in a stoichiometry of 2 Ca²⁺ for 1 ATP. The active Ca²⁺ pumping serves a dual function: lowering the cytosolic Ca²⁺ to cause muscle relaxation and restoring SR Ca²⁺ content for the next beat.

SERCA pump activity can be regulated in several different ways, including small molecules, regulating factors and molecular modifications. Thapsigargin, a sesquiterpene lactone from the plant *Thapsia garganica*, is reported to be able to block SERCA activity²³⁸ and is used extensively as a pharmacological tool in basic research. Phospholamban (PLB) is a small protein (52 amino acids) that binds to SERCA and regulates its activity^{129,194}. Unphosphorylated PLB is positively charged in the cytoplasmic end and binds to SERCA to inhibit its activity. Upon phosphorylation, the positive charges of the cytoplasmic PLB end are neutralized which leads to the dissociation of PLB from SERCA and to the release of its inhibitory effects²⁰⁷. Sarcolipin is another novel SR protein that has been shown to regulate SERCA pump activity⁷. However, its precise role in muscle physiology is less well understood.

SERCA plays a key role in ensuring normal Ca²⁺ cycling and hence contractility in the working myocardium, and indeed much of the contractile dysfunction observed in cardiac hypertrophy and heart failure has been attributed to rather modest reductions in SERCA activity^{51,152,163}. Consistent with this idea, contractile dysfunction in heart failure can be reversed by overexpression of SERCA2a in failing myocytes⁵³. Increased SERCA expression has also been reported to increase Ca²⁺ alternans threshold⁴⁹, which will be introduced later in the Ca²⁺ alternans section of this thesis.

1.2.3 Na⁺/Ca²⁺ Exchanger (NCX)

A second cytosolic Ca²⁺ removal process is the NCX. Ca²⁺ extrusion by NCX across the sarcolemma is the major mechanism to balance Ca²⁺ influx through the LTCC. The stoichiometry of

ion transport by NCX is 3 Na⁺ for 1 Ca²⁺, which is electrogenic. NCX contributes a very small amount of Ca²⁺ influx in its reverse mode (outward current) during the upstroke phase of a Ca²⁺ transient, and a small Ca²⁺ efflux in its forward mode (inward current) during Ca²⁺ removal phase. Both the outward and inward currents contribute to the shape of the action potential¹⁹⁵.

NCX also plays an important role in the generation of DADs. Spontaneous Ca²⁺ release from the SR in between electrical beats can induce NCX forward mode resulting in a depolarizing inward current, often referred as the transient inward current. This current depolarizes the membrane potential leading to the arrhythmogenic DADs. In case DADs are superthreshold, they can trigger an action potential that can disturb the rhythm of the heart when conducted further in the tissue²²¹. Despite this apparent essential role of NCX in physiology and/or pathophysiology, NCX knockout mice showed only a very mild phenotype with rather normal global contractions and Ca²⁺ handling⁹⁴.

1.2.4 Cardiac Ca²⁺ cycling and Ca²⁺ alternans

Cardiac alternans refers either to contractile alterations or to AP alterations that occur on every other beat, characterized by the alterations of T-wave in ECG and QRS interval¹¹⁸. T-wave alternans is now believed to be induced by cellular AP restitution alternans¹⁵⁶. Alternans in the cellular repolarization has been proposed to foster pathological heterogeneities in the electrophysiological properties of cardiac tissue. Such inhomogeneities are a well known substrate for cardiac arrhythmia²²³.

Restitution alternans is due to abnormalities of ionic currents during the repolarization of cellular APs, that could be altered by modulations in intracellular Ca²⁺ handling. In isolated cardiomyocytes APD alternans can be abolished by interventions that affect Ca²⁺ cycling, including RyR inhibition, LTCC inhibition, SR depletion and buffering of cytosolic Ca²⁺^{65,145}. These reports suggest an important role of cellular Ca²⁺ alternans in the development of arrhythmia, and support the notion that Ca²⁺ transient alternans might be a mechanism of repolarization alternans¹¹⁸.

There is also some evidence for cellular Ca²⁺ alternans being independent of AP duration alternans⁴⁹. Overexpressing SERCA2a increases the threshold of cellular alternans⁴⁹, implying a role of SR Ca²⁺ reuptake in the development of cardiac alternans. SR Ca²⁺ release has been suggested as another important candidate that may account for Ca²⁺ alternans in single cells. During high frequency pacing, direct measurements of SR Ca²⁺ contents shows that Ca²⁺ alternans does not necessarily require SR Ca²⁺ content alternans, but rather depends on the RyR recovery from inactivation/adaptation¹⁶¹. Maneuvers that increase Ca²⁺ release via RyR decrease mechanical alternans⁵⁷. Alternans induced by acute ischemia occurs at much slower

heart rates than those of normal control animals, which also suggests RyR dysfunction as the cause¹⁶⁷. Local inhibition of RyR function by acidosis or the local anesthetic tetracaine can also produce Ca^{2+} alternans^{50,120}. These studies highlight the dysfunction of RyR channel as a primary mechanism of Ca^{2+} transient alternans, irrespective of SR Ca^{2+} load. Taken together, it is clear that RyR dysfunction is an important mechanism of alternans, independent of the rate of Ca^{2+} cycling¹¹⁸.

1.3 T-tubule membrane system and EC-coupling

During the cardiac action potential, Ca^{2+} influx across the cell membrane via LTCC triggers the release of more Ca^{2+} from the SR by activating coupling RyRs in the adjacent SR membrane. SERCA works continuously to pump Ca^{2+} back to the SR, the NCX also takes part in Ca^{2+} extrusion by utilizing the electrochemical Na^+ gradient across the membrane. Evidence has been presented that those key proteins involved in the EC-coupling locate predominantly at the T-tubules²⁷.

T-tubules are invaginations of the surface membrane that occur at each Z-line, and branch within the cell to form a complex network with both transverse and longitudinal elements¹⁹⁸. The organization of T-tubule, SR, cytoskeleton and related coupling is illustrated in figure 1.4. This arrangement ensures rapid and uniform spread of APs into the cell interior such that the first steps of EC-coupling are synchronized. A particular proximity between LTCC and RyR at the plasma membrane and junctional SR, respectively, also referred to as a couplon²⁰³, further increases the reliability of these early steps of EC-coupling, as illustrated in figure 1.1. The spatial arrangement

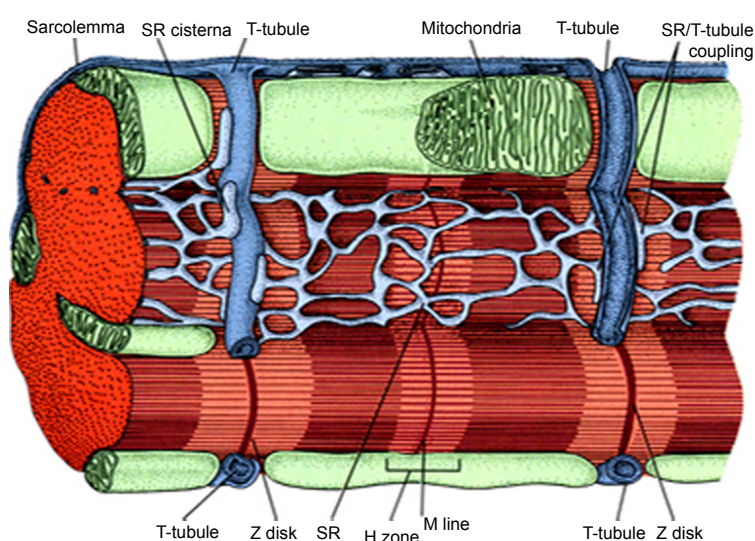


Figure 1.4: Organization of SR, T-tubule and cytoskeleton. Modified from Don W. Fawcett et al., *The Journal of Cell Biology*, 1969, 42:1-45.

of T-tubules also enables the rapid Ca^{2+} extrusion, since no part of the cytoplasm is more than 1 μm from the nearest T-tubule and its Ca^{2+} removal pathways¹⁵¹.

The way T-tubules are tethered to Z-lines remains elusive, however, there are several proteins reported to be involved in this interaction such that the structure of T-tubule is organized and stabilized. Spectrin is one candidate of these intermediate proteins¹⁰³. Another cytoskeletal protein family is ankyrins, which also target Na^+/K^+ -ATPase and $\text{Na}^+/\text{Ca}^{2+}$ exchanger to the T-tubule and play an important role in EC-coupling^{80,140}. Furthermore, it is also reported that T-tubules are linked to the SR by some specific skeletal proteins, like JP-2⁶³, which plays an important role in the development from hypertrophy to advanced heart failure²³³.

Emerging evidence suggests the important role of T-tubules in heart failure. Significant T-tubule loss in ventricular myocytes is visible in a canine model of tachycardia-induced heart failure^{10,82}. Disruption of t-tubules in transverse direction has also been reported in a case of human tachycardia-induced heart failure³⁶. Loss of T-tubules displays a reduced ability to trigger SR Ca^{2+} release in ventricular myocytes from spontaneously hypertensive rats that develop heart failure²⁰⁰. This phenomenon is also visualized in ventricular myocytes from human failing hearts, where a loss of T-tubules reduces the synchrony of SR Ca^{2+} release¹²². In summary, current evidence from small and large animal models suggests that a rearrangement or a partial loss of t-tubule structures can constitute an important factor contributing to dyssynchronous cellular Ca^{2+} release and impaired Ca^{2+} handling in myocardial remodeling. T-tubule alterations appear early and may progress during the process of myocardial remodeling⁸⁴.

1.4 Interactions between extracellular matrix, Z-disk and F-actin

Cardiac extracellular matrix (ECM) is composed of fibrous proteins, such as collagen and elastin that serve as steel reinforcements for the myocardium. Two types of glycosaminoglycans (glycoproteins and proteoglycans) serve as the space filling concrete. The exact ECM composition of the heart varies with age and physiological status, which is dynamically regulated in a normal myocardium, and dysregulation can lead to severe pathologies^{43,229}.

The ECM provides mechanical support to the heart for translating the force generated by individual myocytes into organized contraction force that allows pumping blood. To effectively transmit force, striated muscle contains specialized periodic membrane-associated plaques known as costameres that anchor Z-disks to the sarcolemma. ECM-costamere interactions are mediated by another type of protein linkages, laminin-integrin linkage and laminin-sarcoglycan linkage. Costameres co-distribute with the Z-line and the M-line, and coordinately transduce contractile

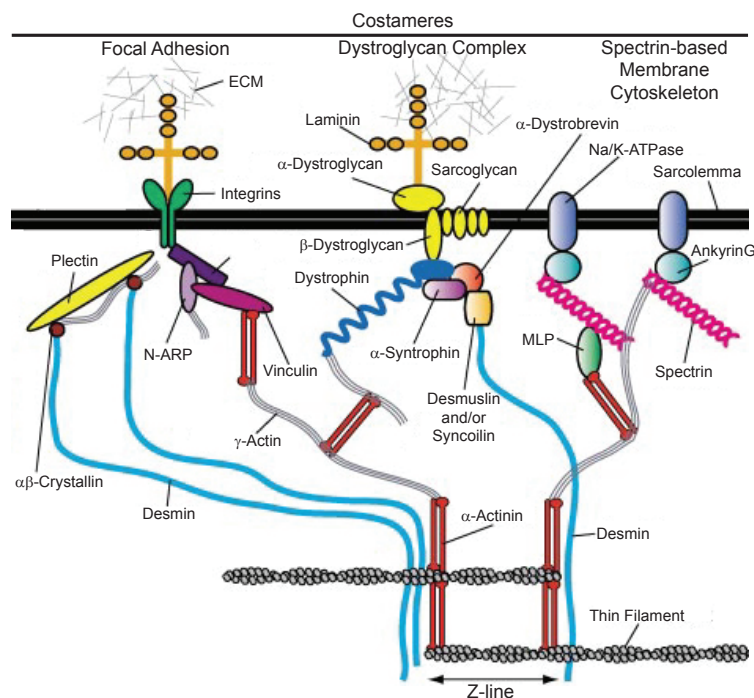


Figure 1.5: Interactions between Z-disk, costamere and ECM. Figure was modified from Clark et. al, Annual Review of Cell and Developmental Biology, 2002,18:637-706.

force from the Z-line to the basement membrane, and latterly to connective tissues in ECM^{42,89}. In this F-actin/Z-disk/ECM linkage complex, anti-parallel F-actins are interlinked to α -actinin, a F-actin binding protein located in the Z-disk¹⁹⁶. The α -actinin subsequently binds to γ -actin and finally to costameres. Detailed Z-disk, costamere and ECM interactive bindings are illustrated in figure 1.5.

The ECM is not only a scaffold that provides support for cells, but it also facilitates chemical signaling during myocardial homeostasis and remodeling. For example, changes in ECM components influence cardiac contractile function by influencing bidirectional signaling from integrins (i.e., inside out signaling as well as outside in signaling)²⁵ and induce hypertrophic response¹²⁴. The laminin-dystroglycan-dystrophin signaling cascade seems to be important for the response to increased pressure¹⁰¹. These signaling pathways exemplify the importance of signaling from the ECM to cardiomyocytes for physiological homeostasis and pathological responses.

1.5 Optical action potential measurements

In EC-coupling the action potential is the initiating event, which is also essential to understand the basic physiology and pathology of cardiomyocytes. The recording of cellular APs is usually performed with the patch-clamp technique, which was developed in late 1970's and early 1980's.

Today the patch-clamp technique is still the gold standard for cellular AP recording¹⁸¹.

Since the early 1990's, several new approaches in drug discovery have changed the pursuit of new drug candidates. Combinational chemistry has accelerated the production of large and diverse sets of novel organic compounds, which enables extensive and quantitative characterization of structure-activity relationship (qSAR)⁶⁰. Molecular cell biology and genetics have allowed identification of many new biological targets, as well as their *in vitro* expression that can be used in High Throughput Screening (HTS)⁹⁷. With automatic screening robots, large amount of "hits" can be generated much faster than before. To evaluate those compound hits in the following qSAR as well as "lead" compound optimization, drug safety issues are increasingly important. In here, cardiotoxicity, especially drug-hERG interactions, have gained a high priority that need extensive testing¹⁶⁶. Thus high-speed evaluation of those hits or lead derivatives is highly desired in pharmaceutical industry.

Within recent years a number of approaches to automatize patch-clamp measurements have been successfully commercialized. Examples are the SyncroPatch (Nanon Technologies, Munich, Germany), the FlyScreen (flyion, Tübingen, Germany) or the PatchXpress (Molecular Devices, Sunnyvale, USA) for the patch-clamp approach and the MEA96 (Multi Channel Systems, Reutlingen, Germany) as a general electrophysiological recorder. All these systems are primarily designed to investigate so called immortalized cell lines, that follow a well defined handling routine. These immortalized cell lines are good options when studying heterologously expressed proteins, such as hERG. However, these cell lines can only characterize no more than one channel, while leaving out all other channels that contribute to the AP in cardiomyocytes.

When it comes to more specific physiological or pathological questions primary isolated cells are a much more appropriate approach. This holds especially true for excitable cells such as cardiomyocytes. Due to easier isolation and cell handling neonatal cells are often preferred. For adult cardiomyocytes a highly reproducible isolation procedure is now available¹⁰⁰. However, although isolated adult cardiac myocytes can be cultured for one week without major dedifferentiation²¹⁹, the shape and fragility of isolated cardiomyocytes do not allow a reliable handling in suspension that is as necessary for use in the commercially available automated cellular electrophysiology setups. An alternative approach is a contact-free measurement based on an optical readout of molecular sensors. These sensors are probed by light and changes in photon responses are translated into values for the electrical (membrane) potential.

According to the mechanisms of sensing voltage change, potentiometric sensors can be classified into four groups:

I: Redistribution dye. The dyes exhibit potential-dependent changes in their transmembrane

distribution, which leads to a large fluorescence change (typically 100% change per 100 mV). However, the redistribution process is too slow, usually seconds or minutes range, to be used for the AP recording⁸⁷.

II: Stark-effect-based dyes. Those dyes are exclusively based on the Stark-effect*¹¹³. These sensors such as ANNINE dyes⁶², which are fast enough to follow APs, display a 25% intensity change per 100 mV, but are not ratiometric and show strong photobleaching³².

III: A third group of sensors are electrochromic small molecules^{87,106,192}. Following changes in the electromagnetic field surrounding the probes, the distribution of an extensive intramolecular conjugated electron system is modulated and translated into changes in the fluorescent properties of the probe that can be measured. This type of intramolecular electron redistribution can take place within microseconds, and is fast enough to follow action potentials. Since the arrangement of the electronic structure happens inside the fluorophore, its magnitude is very small, usually in the range of 10% fluorescence change per 100 mV. Typical dyes, such as RH-237¹⁴², di-4-ANEPPS¹⁰⁷, and di-8-ANEPPS⁷⁸ (figure 3.1A), are widely used in neurology³³ and cardiology.

IV: Genetically encoded sensors. These sensors usually consist of one domain for voltage-sensing and at least one fluorophore for signal readout, such as SPARC⁶ and voltage-sensitive fluorescent protein (VSFP)¹⁸⁰. Some sensors contain two fluorophores that make up a Förster resonance energy transfer (FRET) pair, such as FlaSh⁷⁴ and Mermaid²¹⁴.

I deployed and evaluated a di-8-ANEPPS-based ratiometric read-out of the membrane potential that allows the registration of single cellular action potentials of adult cardiomyocyte and hence the use of that method in automated high content screens, e.g. QT-screens. With such an approach I investigated the electrophysiological differences between adult and neonatal rat ventricular myocytes. Finally, the technique was extended for the genetically encoded potential sensor Mermaid to allow for more flexible screening modes including chronic applications of test substances.

1.6 The effects of CytoD in the culture of cardiomyocytes

Cytochalasin D (CytoD) is a fungal metabolite that suppresses cytokinesis by blocking formation of contractile microfilament structures that results in multinucleated cell formation, reversible

*The Stark effect is the shifting and splitting of spectral lines of atoms and molecules due to the presence of an external static electric field.

inhibition of cell movement, and the induction of cellular extrusion³⁷.

In cardiac myocytes it is believed to act as a F-actin disruptor^{9,20,35,215,237}. In such studies CytoD was used along diacetyl monoxime (DAM) and butanedione monoxime (BDM) as a mechanical uncoupler on the organ level⁹, in tissue^{20,237} and with isolated myocytes³⁵. However, other reports suggested that in adult ventricular myocytes CytoD instead stabilizes the actin cytoskeleton^{40,119}. Using 40 μM CytoD as a cell culture supplement, a positive effect of CytoD on the morphology of cardiomyocytes was reported in these studies.

One of the aims of the thesis was to investigate how CytoD affects the morphology and function of adult cardiomyocytes in culture and whether and how CytoD can be used as a routine supplement in single cell models of cardiomyocytes.

1.7 Computer-aided analysis of cardiac Ca²⁺ signaling

In confocal microscopy, line scanning is currently the most popular recording mode for investigations of cellular CICR dysfunctions on cardiomyocytes, such as EC-coupling dyssynchrony^{50,122}, Ca²⁺ alternans⁴⁶ and Ca²⁺ sparks¹⁶². The scanning speed of line scan can be quite high, usually into the kHz range, however, its spatial information is limited to, just as its name implies, a single line.

With the new development of fluorescent probes and advancements of opto-mechanical imaging approaches²²², high-speed/high-resolution living cell imaging of subcellular signaling events has greatly fostered our understanding of their physiology as well as their pathophysiology. In cardiomyocytes in particular, such new techniques enable researchers to follow the fast subcellular CICR during EC-coupling. With cardiac CICR taking place on the millisecond timescale and the requirement of two dimensions (2D) in scanning a whole cell, pixel dwell time is down well below the microsecond time domain. Such limited pixel dwell times unavoidably result in image data associated with a rather low signal-to-noise ratio that has started limiting progress, especially when the pattern of Ca²⁺ being released is the focus of interest.

Traditionally, image quality can be improved by sophisticated generic algorithms attempting to reduce the noise in the image data, such as filtering in spatial domain or frequency domain. Unavoidably, this changes the amplitude and/or kinetic properties of recorded CICR signals and often also functionally reduces the spatial resolution. New Ca²⁺ signaling data analysis strategies have emerged in the last few years to overcome such drawbacks of those traditional methods, such as deconvolution techniques²⁴⁰, template matching¹⁸⁶, model-based fitting^{69,73} and sequential Monte Carlo methods²²⁰. All these methods are designed for single pixel Ca²⁺ transients analy-

sis.

Here, an analytical approach is introduced to achieve better signal-to-noise data by describing the time course of Ca²⁺ signals with very few and basic assumptions and subsequent pixel-wise fitting of such equations to the recorded data. The CICR information of the entire cardiomyocyte can be extracted to reveal subcellular details of EC-coupling that help answering the “where”, “how much” and “how fast” of the local Ca²⁺ signaling both in physiology and pathophysiology. Simultaneously, this strategy also ultimately enables us to achieve movies of cardiac Ca²⁺ transients with noise being reduced greatly.

Chapter 2

Materials and Methods, Instruments and Data Analysis

2.1 Materials and Methods

2.1.1 Materials

All drugs or compounds, including quinidine*, 4-AP[†] and E-4031[‡], were purchased from Sigma-Aldrich (Heidenheim, Germany) and dissolved in 100% DMSO to 10 mM as stock. CytoD was also purchased from Sigma-Aldrich, but its stock solution was 40 mM to keep the DMSO as low as 0.1% when diluting to 40 μ M was used.

Di-8-ANEPPS was purchased from Invitrogen (Darmstadt, Germany) and dissolved in 20% pluronic F-127 (also from Invitrogen, to 5 mM as stock). Fura-2/AM, Indo-1/AM and Fluo-4/AM (all from Invitrogen) were solved in 20% pluronic F-127 (1 mM as stock).

2.1.2 Adult rat ventricular cardiomyocytes isolation

Adult cardiomyocyte isolation and culture was performed as described previously¹⁰⁰. Briefly, adult male Wistar rats (6 ~ 12 weeks old, 200 ~ 400 g) were handled and sacrificed in accordance with the Guide for the Care and Use of Laboratory Animals published by the US National Institutes of Health (NIH Publication No. 85-23, revised 1996). The rat was anesthetized by an intraperitoneal injection (i.p.) of a mixture of 137 mg/kg Ketamine hydrochloride (Ursotamin[®], Serumwerk, Bernburg, Germany) and 6.6 mg/kg Xylazine hydrochloride (Rompun[®], Bayer Health Care, Leverkusen, Germany). After the rat went to sleep, 20 mg/kg dihydrate sodium citrate was injected

* Short name for 6'-methoxy-a-(5-vinyl-2-quinuclidinyl)-4-quinoline methanol.

[†] Short name for 4-aminopyridine.

[‡] Short name for 1-[2-(6-methyl-2-pyridyl)ethyl]-4-(4-methylsulfonyl-aminobenzoyl)-piperidine.

to prevent blood clot. Then the rat was killed by decapitation.

The heart was flushed with 10 ml of ice-cold Ca^{2+} -free solution (CFS, components in mM: 134 NaCl, 11 Glucose, 4 KCl, 1.2 MgSO_4 , 1.2 Na_2HPO_4 , 10 HEPES, pH 7.35), removed, attached to a Langendorff apparatus and perfused retrogradely with O_2 saturated CFS (37 °C) containing 200 μM EGTA at a rate of 4 ml/min for 5 min. The perfusate was then changed to O_2 saturated CFS (37 °C) containing 2 mg/ml Collagenase Type II (Worthington Biochemical Corp., Lakewood, NJ, USA) or 0.17 mg/ml Liberase TM (Roche Diagnostics Deutschland GmbH, Mannheim, Germany) for 25 min.

The ventricles were removed, minced and placed in O_2 saturated CFS. After sedimentation, the resulting pellet was mixed and resuspended in 20-25 ml of O_2 saturated CFS and incubated in 37 °C water bath for 5 min. The pellet was mixed and resuspended again in 20 ~ 25 ml of O_2 saturated low- Ca^{2+} solution containing 50% of CFS and 50% of Ca^{2+} containing solution (CCS, equals CFS plus 0.09% DNase and 200 μM Ca^{2+}) and incubated as above. Furthermore, the supernatant was discarded, the pellet was resuspended in 20-25 ml of O_2 saturated CCS and incubated as above. Now, rat ventricular myocytes were released from the soft tissue by gentle trituration.

The cell suspension was plated into in 12-well plate with cover slips, which were coated with extracellular matrix proteins (ECM gel from Engelbreth-Holm-Swarm mouse sarcoma, diluted to 12.5% in M199 medium, Sigma-Aldrich, Heidenheim, Germany), they were allowed to settle down for approximately 1 h in medium M199 (with Earle's salts and L-glutamine, from PAA Laboratories, Pasching, Austria), 100 $\mu\text{g/ml}$ Penicillin (PAA Laboratories, Linz, Austria), 100 $\mu\text{g/ml}$ Streptomycin (PAA Laboratories, Linz, Austria) and 50 $\mu\text{g/ml}$ Kanamycin (PAA Laboratories, Linz, Austria). The medium was supplemented with 870 nM insulin, 65 nM transferrin and 29 nM Na-selenite (Sigma-Aldrich, Heidenheim, Germany) (ITS supplemented medium). The myocytes were cultured in an incubator at 37 °C with a 5% CO_2 atmosphere. One hour after plating the medium was changed for fresh medium supplemented with ITS.

2.1.3 Adult mouse cardiomyocyte isolation

Mouse adult myocyte preparation was adapted from the rat preparation. Mice (FVB/N or RacET) were handled and sacrificed in accordance with the Guide for the Care and Use of Laboratory Animals published by the US National Institutes of Health (NIH Publication No.85-23, revised 1996). Briefly, animals were anesthetized (0.1 ml/10 g body weight) with a mixture of 8.5% ketamine hydrochloride, 7.5% xylazine hydrochloride and 84% NaCl i.p.. Afterwards, we injected citrate (2 $\mu\text{l/g}$ body weight) i.p. and the animal was killed by decapitation. Ice-cold CFS was injected in both

ventricles to arrest the heart and to remove blood. Then the heart was cannulated to allow a retrograde Langendorff-perfusion with CFS (O_2 saturated, with 200 μ M EGTA) at room temperature for 5 min. Following a 0.1 mg/ml Liberase TM perfusion (in CFS) at 37 °C for 12 min, the atria were cut away and placed into 1 ml CFS (same as CFS, but without EGTA, 37 °C). Thereafter, the extracellular Ca^{2+} concentration was increased by repetitive addition of 50 μ l CCS (oxygenated, 37 °C) for ten times in 5 min intervals. The atria were triturated in the wells of the 12-well plate (with cover slips coated with extracellular matrix, Sigma-Aldrich, St. Louis, USA). After 1 hour for the cell to settle down, the supernatant was discarded and finally 1 ml medium M199 was added. The myocytes were cultured in an incubator at 37 °C with 5% CO_2 and saturated humidity.

2.1.4 Neonatal rat cardiomyocyte isolation

Neonatal cardiomyocyte isolation and culture was performed as described previously³⁹. Briefly, 4 ~ 6 neonatal or one day old rat pups were anesthetized with ice, killed by decapitation, the hearts were removed and put into ice-cold isolation buffer (in mM: 116 NaCl, 20 HEPES, 0.8 Na_2HPO_4 , 5.6 Glucose, 5.4 KCl and 0.8 $MgSO_4$, pH 7.35). The hearts were washed once with isolation buffer and cut into 0.5 mm³ pieces. The tissue pieces were transferred into enzyme solution consisting of isolation buffer plus 0.6 mg/ml Pankreatin (P3292, from Porcine Pancreas, Sigma-Aldrich, Heidenheim, Germany) and 0.4 mg/ml Collagenase Type II ((Worthington Biochemical Corp., Lakewood, NJ, USA) and incubated in 37 °C water bath with gentle agitation for 20 minutes. The resulting supernatant from the first digestion was discarded. Then the heart tissue pieces were digested for another 5 times as described above. Every time when collected, the resulting supernatant was centrifuged (600 g for 5 minutes) and resuspended immediately in F10 complete medium (Invitrogen GmbH, Karlsruhe, Germany) containing 10% horse serum (Fisher Scientific GmbH, Schwerte, Germany), 5% FCS (PAA Laboratories, Linz, Austria) and 100 μ g/ml Penicillin/Streptomycin. Finally, all the 5 times of cell suspensions were combined together, plated into a 75 cm² flask, and incubated for 2 hours in 37 °C. After that, the supernatant was centrifuged as described above, and the cell pallet was resuspended in F10 complete medium. The cells were counted and plated onto ECM-coated cover slips in 12-well plates at a density of 5×10^4 /ml*well. The neonatal myocytes were cultured in an incubator at 37 °C with a 5% CO_2 atmosphere, and the medium was changed in every 2 days till use.

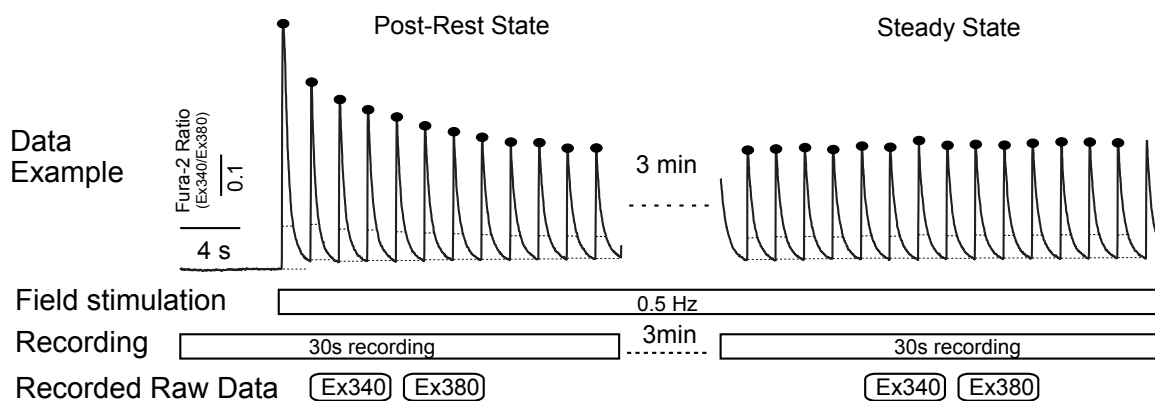


Figure 2.1: Typical Ca^{2+} transient recording. Illustration for Fura-2/AM-based Ca^{2+} transient measurements. Upper panel, typical data sample, with detected peaks (black dots), 80% of Ca^{2+} transient duration (black line under each peak) and the diastolic Ca^{2+} concentration (red line at the bottom of each peak). Lower panel shows the application of field stimulation, the camera recording activity and the final recorded data files (Ex340 and Ex380 stand for the recordings with excitations at 340 nm and 380 nm). For detailed protocol information, please refer to section 2.1.5. For the algorithms used here, refer to section 2.3.3.

2.1.5 Fura-2-based Ca^{2+} transient measurements

Fura-2/AM (Invitrogen GmbH, Darmstadt, Germany) was dissolved (1 mM stock solution) with DMSO containing 20% Pluronic F-127 (Invitrogen GmbH, Darmstadt, Germany). Before use, the dye was diluted with Tyrode (components in mM: 140 NaCl, 5 KCl, 10 Glucose, 10 HEPES, 1.8 CaCl_2 , 1.0 MgCl_2 , pH 7.35) to 1 μM . The cells were incubated in the dye solution for 30 min and incubated in fresh Tyrode for another 10 ~ 15 min for dye de-esteration. After that, the coverslips were transferred onto the stage of a video-imaging setup (TE2000-U, Nikon, Tokyo, Japan). A fast monochromator was used for alternating excitation of Fura-2 (340 nm and 380 nm) while the emitted fluorescence was collected through a long pass filter (>515 nm) onto a fast CCD camera (4 × 4 binning, 10 ms exposure time, Imago-QE Camera, TILL Photonics, Graefelfingen, Germany). Image acquisition was performed at 64 frames/second (see figure 2.3A). Two 30-second recordings were performed within a three-minute interval. About 5 ~ 10 seconds after the first recording began, field stimulation was started to induce Ca^{2+} transients at 0.5 Hz during the entire experiment (both recordings and interval). The entire protocol is illustrated in figure 2.1.

2.1.6 Indo-1-based Ca^{2+} transient measurements with caffeine

Indo-1/AM (Invitrogen GmbH, Darmstadt, Germany) was dissolved to a 1 mM stock solution with DMSO containing 20% Pluronic F-127 (Invitrogen GmbH, Darmstadt, Germany). Before use, the stock solution was diluted with Tyrode to a final concentration of 2.5 μM . The cells were incubated

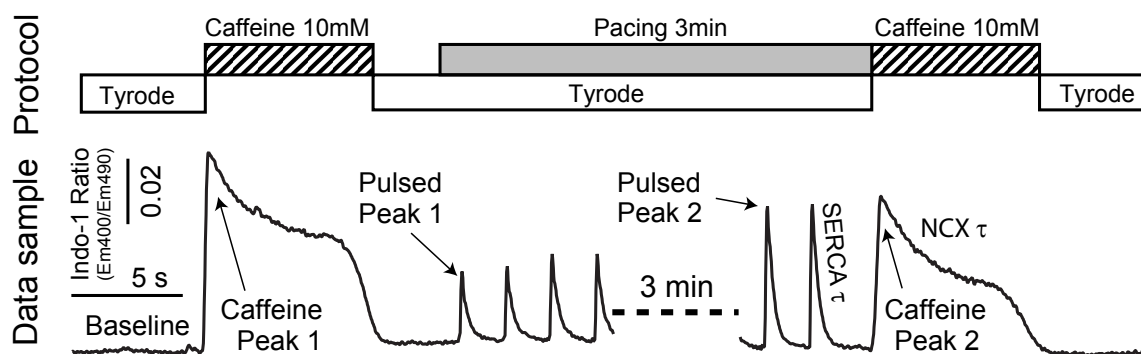


Figure 2.2: Typical caffeine-induced Ca^{2+} transient recording. Illustration of field simulation and video recording data is shown for double application of 5-second 10 mM caffeine. For detailed protocol information, please refer to section 2.1.6.

in the dye solution for 30 min followed by fresh Tyrode for dye de-esteration for another 10 ~ 15 min. After that the coverslips with the cells were mounted in a perfusion chamber on the stage of a video imaging setup (TU2000, Nikon, Tokyo, Japan). Excitation of Indo-1 was achieved with a monochromator at 355 nm while the emitted fluorescence was detected simultaneously at around 405 nm and 490 nm with an image splitter (450 nm) and the CCD detector of a fast camera (Retiga-2000R, QImaging, Surrey, BC, Canada). Images (200×150 pixels) were acquired at 40 frames/second (see figure 2.3A). The routine caffeine protocol is depicted in figure 2.2 and comprised two recording periods during which brief caffeine pulses (5 seconds, 10 mM) to elicit Ca^{2+} transients. The first caffeine transient was evoked under resting conditions, while the second one under steady-state conditions.

2.1.7 Fluo-4-based confocal Ca^{2+} measurements

Fluo-4/AM (Invitrogen GmbH, Darmstadt, Germany) was dissolved to a 1 mM stock solution with DMSO containing 20% Pluronic F-127 (Invitrogen GmbH, Darmstadt, Germany). Before use, the stock solution was diluted with Tyrode to a final concentration of 1 μM . Cardiomyocytes were incubated in the dye solution for 30 min followed by fresh Tyrode for dye de-esteration for another 10 min. In experiments when membrane staining was performed in parallel, 1.0 μM di-8-ANEPPS was included into the Fluo-4 loading solution. Following de-esterification, the coverslips with cells were mounted into a custom-build recording chamber on the stage of a Leica TCS SP5 confocal microscope (see section 2.2.4). Excitation was performed with the 488 nm laser line of an Argon-Krypton mixed gas laser. For single emission recordings, the detection bandwidth was adjusted to 495 nm ~ 650 nm while for simultaneous dual emission recordings two detection channels were selected (495 nm ~ 540 nm for the Fluo-4 emission and 560 nm ~ 650 nm for the di-8-ANEPPS emission).

2.1.8 The construction of adenovirus-based mermaid

Adenoviruses encoding for Mermaid were constructed as previously described for genetically encoded Ca^{2+} sensors¹⁰⁰. In short, generation of recombinant Adenoviruses was accomplished by using the Transpose-AdTM adenoviral vector system (MP Biomedicals, USA). pCR259 Adenovirus transfer vectors encoding Mermaid were transformed in HighQ-1 Transpose-AdTM 294 competent cells, a bacterial cell line carrying the Transpose-AdTM 294 plasmid and a plasmid encoding a trans-acting Tn7 transposase. After a Tn7-based transposition, recombinant adenoviral genome was purified from bacteria and transfected into the QBI-HEK 293 cell line using Lipofectamine 2000 (Invitrogen, Darmstadt, Germany). In this cell line, the recombinant Adenoviruses were generated and propagated with a MOI (multiplicity of infection) between 10 ~ 50. The pcDNA3-Mermaid vector was kindly provided by Dr. Atsushi Miyawaki (RIKEN, Wako, Saitama, Japan).

2.1.9 Optical measurements of action potential

2.1.9.1 Di-8-ANEPPS-based measurements

Di-8-ANEPPS (Invitrogen, Darmstadt, Germany) was dissolved in DMSO to a 5 mM stock concentration. For adult cardiomyocytes, 1 μl di-8-ANEPPS (5 μM in the final solution, 0.1% DMSO) and 2 μl testing drug (or compound to be detected) stock solution or vehicle were diluted in 1 ml Tyrode simultaneously, and freshly isolated cardiomyocytes (day 0 in vitro, DIV0) were incubated with this solution for 7 minutes. After that, the dye was washed away with fresh Tyrode containing the same concentration of testing drug. Then the coverslips were mounted in recording chambers on the stage of an inverted microscope (TE2000-U, Nikon, Tokyo, Japan). Imaging was performed through a 40 \times oil immersion objective (Plan Fluor, N.A.=1.30, Nikon, Tokyo, Japan). The cells were field stimulated with square pulses (5 mV, 5 ms duration) at a frequency of 0.5 Hz. Thirty cells were selected randomly and 5 APs were recorded for each cell. For neonatal cells, electrically coupled cells (the coupling between cells forms spontaneously usually at DIV5 or DIV6) were used, and the dye loading was performed for 20 min without test compound or vehicle. In that case, cells were exposed to the testing drug or vehicle for 5 min before recording after dye loading. Then the myocytes were field stimulated at a frequency of 1 Hz, and 30 cell clusters were selected randomly and 5 APs were recorded for each cell.

2.1.9.2 Mermaid-based measurements

After isolation, adult cardiomyocytes were immediately transduced with adenoviruses coding for Mermaid. Forty-eight hours after infection, cells were treated with 20 mM BDM (Sigma-Aldrich, Heidenheim, Germany) for 10 min before recordings. The entire environment and all the solutions were pre-warmed to 37 °C, and the cells were transferred onto the microscope stage and electrically paced. If a test compound was used, usually 3 APs before compound application and 3 APs 2 minutes after application were recorded on the same cell.

2.1.10 Emission spectrum measurements

2.1.10.1 Emission spectrum measurements of di-8-ANEPPS with KCNH2 cells

CHO/KCNH2 (CHO/hERG) cells (kindly provided by Dr. Udo Kraushaar, INM Reutlingen, Germany) growing on coverslips were loaded with di-8-ANEPPS at 5 μ M for 20 min in normal Tyrode solution, and mounted on a Nikon TE2000-U microscope (Nikon, Tokyo, Japan) in a custom-made chamber. Similar to the measurements with cardiomyocytes, the CHO cells were excited at 460 nm, but here the fluorescence was guided to a spectrometer (USB2000, OceanOptics, Ostfildern, Germany). Emission spectra from cells in normal Tyrode (5.4 mM KCl) and in high K⁺ Tyrode (in mM: 25.4 NaCl, 120 KCl, 10 Glucose, 10 HEPES, 1.8 CaCl₂ and 1 MgCl₂, pH 7.35) were recorded under the same spectrometer configurations (integration time: 500 ms, no spectrum average).

2.1.10.2 Emission spectrum measurements of Mermaid with COS cells

The emission spectrum measurements of Mermaid with COS cells were similar to the measurements with CHO/KCNH2 cells, except that the COS cells were infected by adenoviruses expressing Mermaid protein 48 hours prior to the experiment.

2.1.11 Patch-clamp measurements

Thick-walled borosilicate glass (GB200-8P; Science Products GmbH, Hofheim, Germany) and a horizontal puller (DMZ-Universal Puller, Zeitz Instruments, Martinsried, Germany) were used for producing patch pipettes (2.5 ~ 3.5 M Ω). The electrophysiological control of the experiment as well as recording of the data was carried out with an EPC 10 patch-clamp amplifier (HEKA Elektronik, Lambrecht, Germany) controlled by "Patchmaster" software (2.40, HEKA Elektronik). All experiments were performed at room temperature (22 ~ 25 °C). The patch pipettes were filled with an intracellular solution (in mM): 135 KCl, 10 NaCl, 0.1 EGTA, 2 MgCl₂, 10 HEPES and 6

MgATP, at pH 7.3. The extracellular solution was Tyrode. The liquid junction potential (4.1 mV) was taken into account by the patch-clamp amplifier while we routinely compensated the series resistance to about 60 ~ 75%. After breaking the cell membrane under the patch pipette the cells were given 3 minutes for exchanging the pipette solution and the cytoplasm. Action potentials of isolated cardiac myocytes were triggered by applying positive currents into the cells via the patch pipette (3 ~ 5 ms, 200 ~ 1300 pA). The data were sampled at 50 kHz and digitally filtered at 10 kHz and 2.8 kHz (Bessel filters).

2.1.12 Actin staining

Actin visualization was performed on fixed cells at the indicated time points after cell isolation. Cells were fixed in 4% paraformaldehyde (in PBS) for 10 min, followed by a washing step in PBS. Permeabilization was performed in 0.5% Triton X-100 (in PBS) for 10 min. After a washing step in PBS, the cells were blocked by a 20 min incubation in 5% bovine serum albumin (in PBS). Thereafter, the cells were probed with 0.5 μ M ATTO-647N phalloidin (Atto-Tec GmbH, Siegen, Germany) for 2 hours at room temperature. Finally, the myocytes were washed with PBS, mounted in ProLong Gold Antifade reagent (Invitrogen, Darmstadt, Germany) and stored at 4 °C until visualization.

Super-resolution imaging was performed on a TSC SP5 STED (stimulated emission depletion) with an HCX Plan APO 100 \times oil immersion objective (Leica Microsystems GmbH, Wetzlar, Germany). For an initial overview of the actin staining (ATTO-647N phalloidin) and membrane visualization (GPI-YFP) we used the microscope's conventional confocal mode (excitation: 635 nm and 488 nm laser lines, respectively). Emissions were collected in the spectral range of 648 ~ 700 nm (ATTO dye) and 495 ~ 594 nm (YFP). Images were despeckled and for the merge of the channels the individual intensity was adjusted and a red and green lookup-table was applied using ImageJ (Wayne Rasband, NIH, Bethesda, USA). A rescan of the actin staining at higher magnification was performed in the microscope STED mode. While the probe was excited with a pico-second pulsed 635 nm laser (PDL800-B, PicoQuant GmbH, Berlin, Germany) stimulated emission was induced by a femto-second laser (MaiTai, Newport Corp., Irvine, USA). STED images were deconvolved by custom made algorithms based on a linear Tikhonov deconvolution implemented in MatLab (MathWorks, Ismaning, Germany).

2.1.13 T-tubule visualization

For the T-tubule visualization of living cardiomyocytes, cells were loaded with di-8-ANEPPS (dye 5 μ M, DMSO 0.1%, pluronic F-127 0.02%) in EGTA (10 mM)-supplemented Ca^{2+} -free Tyrode for 20 ~ 30 min. For the visualization on fixed cells, cardiomyocytes were transduced with adenoviruses coding for GPI-YFP overnight, and incubated for another 48 hours. After that the cells were transferred onto the Leica TCS SP5 microscope (refer to section 2.2.4) and Z-stacks were acquired with a Leica 63 \times Plan APO oil immersion objective (N.A.=1.4).

2.1.14 Sarcomere length measurements

Real-time sarcomere length changes were monitored with a fast camera (sampling rate 240 Hz, MyoCam, IonOptix Corp., Milton, USA) from electrically stimulated cells maintained on coverslips by using an edge-detection approach by the Ion Wizard software (IonOptix Corp., Milton, USA). The system directly stores sarcomere length changes that were further analyzed in Igor Pro software (WaveMetrics Inc., Oregon, USA) with custom-made macros (included in the attached CD-ROM).

2.2 Instruments

2.2.1 Imago video-imaging microscope

The Imago microscope system was based on an inverted microscope (TE-2000, Nikon, Tokyo, Japan) equipped with a CCD camera (Imago-QE, TILL Photonics GmbH, Gräfelfing, Germany), as illustrated in figure 2.3A. A monochromator (Polychrome IV, TILL Photonics GmbH, Gräfelfing, Germany) was used to generate the desired excitation wavelengths which were reflected by a dichroic mirror (splitting edge at 470 nm) and focused onto the cells with a 20 \times oil objective (CFI Plan Fluor, Nikon, Tokyo, Japan). For Fura-2 measurements, the emission was collected by the same objective, filtered with a 480 nm long pass filter and recorded with a CCD camera (Imago, see figure 2.3A). Both the camera and the monochromator were controlled by the Digital Signal Processor (DSP)-driven Imaging Controlling Unit (ICU, TILL Photonics GmbH, Gräfelfing, Germany), which was connected to a computer and operated with TILLvisION v4.0 software.

2.2.2 Retiga video-imaging microscope

The Retiga system was quite similar to the Imago system, except that a different Nikon TU-2000 microscope (Nikon, Tokyo, Japan) and Polychrome V (TILL Photonics GmbH, Gräfelfing,

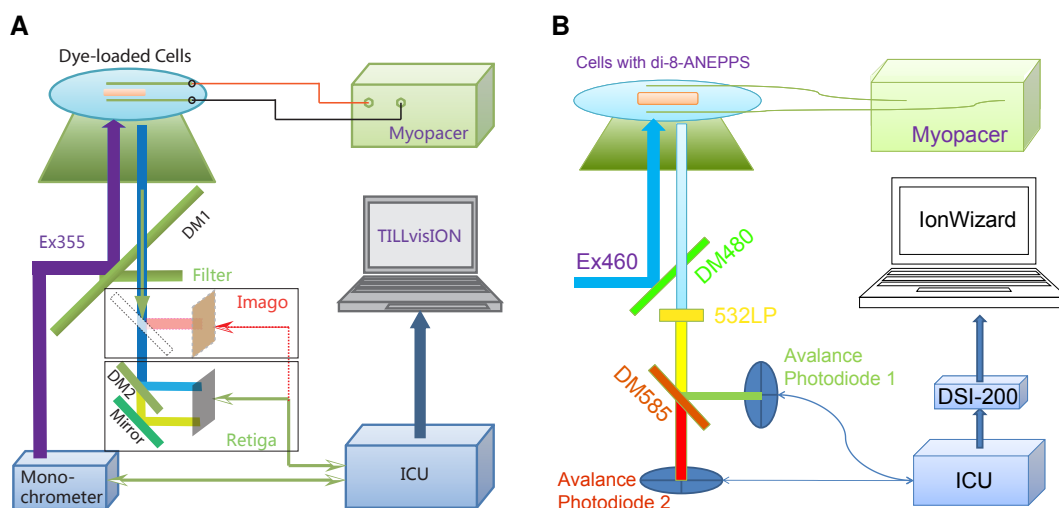


Figure 2.3: The design of imaging setups. **A**, the basic design of the Imago and Retiga video-imaging setups. The system consists of a Polychrome IV or V, a Nikon TE-2000 or TU-2000 inverted microscope and an ICU (central controlling unit). For detailed information, see section 2.2.1 and 2.2.2. **B**, basic design of photometry system. See section 2.2.3 for detailed information.

Germany) were used, as shown in figure 2.3A. The excitation light source was set to 355 ± 7 nm, the cutting edge of dichroic mirror 1 (DM1, the excitation dichroic) was 370 nm, and the emission fluorescence at $390 \sim 420$ nm and $470 \sim 500$ nm were recorded with a CCD camera (Retiga-2000R, QImaging Corp., Surrey, BC, Canada).

2.2.3 Photodiode-based photometry setup

The optical system used for the measurement of APs from neonatal or adult cardiomyocyte based on an inverted microscope (TE2000-U, Nikon, Tokyo, Japan). For the measurements of di-8-ANEPPS, an excitation light (460 ± 7 nm) from a monochromator (Polychrome IV, TILL Photonics, Gräfelfing, Germany) was reflected by a dichroic mirror (splitting at 485 ± 12 nm), and focused to the dye-loaded cells through an immersion objective ($40\times/1.30$ S Fluor - for adult cells; $20\times/0.75$ Plan Fluor - for neonatal cells). The emitted fluorescence was collected by the same objective, and filtered with 532 nm long pass filter (532DCLP, Semrock, Rochester, USA). Then the fluorescence was split into two channels with a 580 nm dichroic mirror (580DCLP, splitting at 580 ± 5 nm, Chroma, Bellows Falls, USA). The two emissions were detected by Avalanche photodiodes (TILL Photonics, Gräfelfing, Germany), then the signals were sampled and digitized at 1 kHz with DSI-200 (IonOptix Inc., Milton, USA) and recorded with IonWizard Software (IonOptix Inc., Milton, MA, USA). For Mermaid measurements, 532DCLP was removed and the 585DCLP was replaced with a 532 nm dichroic mirror (LP532RU, Semrock, Rochester, USA). The entire system is illustrated in figure 2.3B.

2.2.4 Leica TCS SP5 confocal microscope

The Leica TCS SP5 II (Leica Microsystems GmbH, Wetzlar, Germany) was based on an inverted epifluorescence microscope, with build in high-speed laser scanning head (8000 lines per second). For excitation of both, di-8-ANEPPS and Fluo-4, the 488 nm line of an Argon-Krypton mixed gas laser was used. Laser line selection was performed by a computer operated acusto-optical tunable filter (AOTF). The entire microscope design allowed experimental operation in a filterless mode. The primary dichroic was substituted by an acusto-optical beam splitter (AOBS) and detection was achieved with a highly sensitive, two-channel SP prism spectrometer. Control of the experiments as well as the microscope was performed with Leica Application Suite software (ver. 2.4).

2.3 Data Analysis

2.3.1 3D surface reconstruction

Image stack were deconvolved with AutoDeblur software (Media Cybernetics, Inc., Maryland, USA), and 3D reconstructed in Imaris (Bitplane AG, Zurich, Switzerland).

2.3.2 Optical AP duration analysis

All fluorescence data were analyzed in Igor Pro software (WaveMetrics Inc., Oregon, USA) running custom-made macros. Briefly, 4 ~ 5 action potentials' raw data from two channels (532 nm ~ 585 nm and 585 nm ~ 700 nm) were averaged, ratioed and AP duration at 70% recovery (APD_{70}) was calculated. The resulting APD_{70} for different concentrations of individual compounds were fitted with sigmoidal function in GraphPad Prism (GraphPad Software, Inc., La Jolla, CA, USA) to get the final 50% inhibition concentration (IC_{50}) value.

2.3.3 Analysis of Ca^{2+} transients

Ca^{2+} transients recorded with Fura-2/AM were analyzed in Igor Pro (WaveMetrics Inc., Oregon, USA) software running custom-made macros, as illustrated in figure 2.1. All macros are included in the supplementary CD-ROM.

For the analysis of Ca^{2+} transients recorded with Indo-1/AM, both the electrically stimulated Ca^{2+} transients and the caffeine-induced Ca^{2+} transients were analyzed in Igor Pro (WaveMetrics Inc., Oregon, USA) software running custom-made macros, as illustrated in figure 2.2. All macros are included in the supplementary CD-ROM.

For the analysis of Ca^{2+} transients measured with Fluo-4/AM, I used custom-made programs in MatLab 2009a (Mathworks, Ismaning, Germany) and the dip_image toolbox (Quantitative Imaging Group, Faculty of Applied Sciences, Delft University of Technology). Detailed information will be discussed in the text.

2.3.4 Analysis of confocal line-scan images

For the analysis of line-scan recordings of Fluo-4/AM loaded cardiomyocytes I used custom-made programs in MatLab (Mathworks, Ismaning, Germany). Calculation characterization of the dyssynchrony index was performed following a basic approach detailed in a previous publication¹²³. The corresponding programs are included in the attached the CD-ROM.

2.3.5 Surface plotting

All the surface plots in this thesis were created with ImageJ (Wayne Rasband, NIH, Bethesda, USA) and its interactive 3D Surface Plot plugin.

2.3.6 Analysis of T-tubule structure and actin staining

The Fourier power analysis of the T-tubule staining and the F-actin staining were done in Igor Pro (WaveMetrics Inc., Oregon, USA) with custom-made macros (included in the supplementary CD-ROM).

2.3.7 Data statistics

When applicable, all data differences presented in this thesis were analyzed with unpaired student's t-test, and all the error bars represent mean \pm S.E.M (plotted with GraphPad Prism software). All statistics represent data from more than 25 cells from 3 different animals, if not stated otherwise.

Chapter 3

Results

3.1 Optical action potential measurements

3.1.1 Spectral properties of di-8-ANEPPS

Previous studies revealed that di-8-ANEPPS (figure 3.1A) showed a fast temporal response upon changes of membrane potential³³ and a diminished tendency of internalization⁹¹. Furthermore, di-8-ANEPPS can be utilized in a ratiometric manner⁷⁸. Based on those characteristics, di-8-ANEPPS was chosen to optically measure cardiac action potentials. Its spectral properties and its response to potential changes were first confirmed with hERG-expressing Chinese Hamster Ovary (CHO/hERG) cells. Cell depolarization was induced with high concentrations of K⁺ (from 5.4 mM to 120 mM), and caused a significant blue-shift of the emission spectrum, as shown in figure 3.1B. The resulting difference spectrum displayed a positive peak in the range of 500 ~ 580 nm, and a negative peak at 580 ~ 700 nm (figure 3.1C).

3.1.2 Properties of the measurement system

Based on the results of figure 3.1C, a dichroic mirror centered at 585 nm was used to split the emission of di-8-ANEPPS into two separate channels. A long pass emission filter (532 nm) served to eliminate autofluorescence (contribution to the white part of the positive peak in figure 3.1C, autofluorescence data not shown here). The set-up for these measurements was described before (figure 2.3B).

As expected from the spectral blue-shift of di-8-ANEPPS (figure 3.1B and 3.1C), the intensity of the green channel (532 ~ 585 nm) increased upon depolarization (figure 3.2A), and the signal of the red channel (582 ~ 700 nm) decreased (figure 3.2B). When excitation at 460 nm (\pm 3.5 nm) was used, the depolarization induced change in the signal of green channel was 6%, and

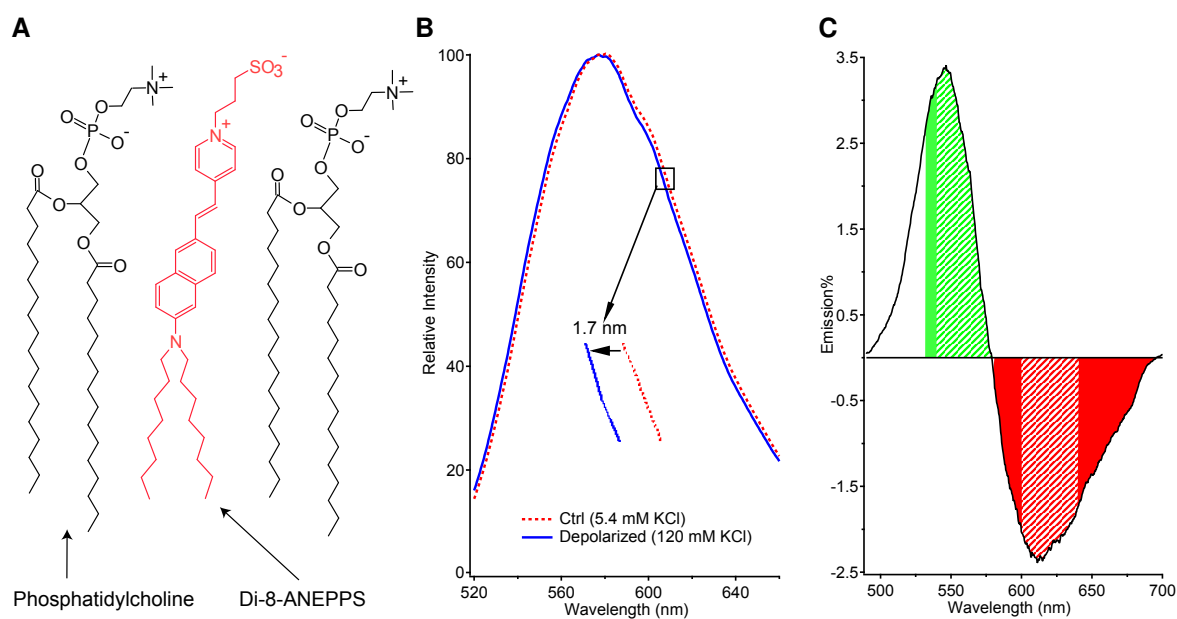


Figure 3.1: Spectral properties of di-8-ANEPPS. **A**, di-8-ANEPPS structure and proposed localization in a lipid bilayer. Di-8-ANEPPS inserts into the cell membrane with its two long $-\text{CH}_2-$ chains, with its conjugative chemical group at the outer membrane to sense potential changes. The figure was modified from a previous report by Klymchenko et. al¹⁰⁶. **B**, after stained with di-8-ANEPPS, CHO/hERG cells were depolarized with Tyrode containing 120 mM KCl. The raw spectra before and after the high concentration of KCl were recorded. **C**, difference spectrum of di-8-ANEPPS before and after membrane depolarization.

4% in the red channel, resulting in a final ratio change of 10% \sim 12% (figure 3.2C). The signal coefficient variation (CV) of typical recordings from this setup was around 0.15%, so the final Signal-to-Noise ratio (SN) was above 50*, which was good enough to follow an cardiac AP, as shown in figure 3.2.

Here both the signals from the green channel (figure 3.2A) and from the red channel (figure 3.2B) displayed significant “humps” (slow peaks indicated with arrows) subsequent to the quick peak (the sharp spikes in figure 3.2C). These signals originated from the cellular contraction. In single channel mode, or intensity-based mode, such signals could not be diminished since contraction is an inherent feature of cardiac cells. However, in the ratiometric mode, such signals were canceled out after ratioing since they showed equal behaviors in both channels (figure 3.2C).

3.1.3 Quantum efficiency

Photomultiplier tubes (PMT) are used extensively in photometry systems⁷⁸. However, the quantum efficiency of a PMT is low, usually less than 35%¹⁶⁸. Here we used more sensitive Avalanche

*SN was calculated according to the formula: $\text{SN} = \mu/\sigma$, where μ represents the mean value of a signal and σ represents the standard deviation.

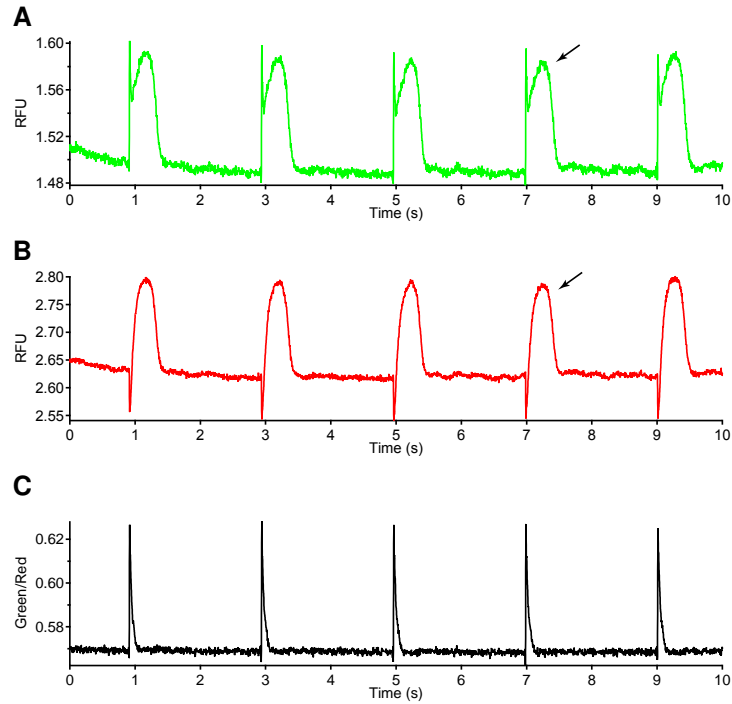


Figure 3.2: Optical action potential measurement of di-8-ANEPPS loaded cardiomyocytes. Rat ventricular myocytes were loaded with di-8-ANEPPS and repetitively stimulated. Raw signals from the green channel (532 ~ 585 nm, shown in **A**) and the red channel (585 ~ 700 nm, shown in **B**) were recorded simultaneously, the ratioed signal was calculated and is shown in **C**. Arrows in panel A and B show the contraction effects.

Photodiodes as photon detectors, whose quantum efficiency was above 85%. Furthermore, with optimized filters the photon detection efficiency Q of the systems was increased greatly. This could be calculated as follows:

$$Q = \frac{\int_{\lambda_{C_1}} E_{Anepps} q_{C_1} d\lambda + \int_{\lambda_{C_2}} E_{Anepps} q_{C_2} d\lambda}{\int_{480nm}^{700nm} E_{Anepps} d\lambda} \quad (3.1)$$

where E_{Anepps} represented the fluorescence emission spectrum of di-8-ANEPPS, λ for the spectral range with the subscript C_1 and C_2 referring to the green and red detection channel, respectively.

Hardy et al. used a rubidium bialkali photomultiplier and a S20 photomultiplier, both of which had a quantum efficiency of 12 ~ 13%⁷⁸. Together with their filter sets, their Q was less than 0.10. Whereas the quantum efficiency of the Avalanche Photodiodes used in our setup was about 90% in the green channel and 86% in the red channel (supplier information), the calculated Q was 0.84, almost an order of magnitude more efficient than Hardy's apparatus.

Based on the figure 3.1B and 3.1C, it was apparent that the central area of the di-8-ANEPPS spectrum (570 ~ 590 nm) had the highest contribution to the photon counts of both the green

channel and red the channel, but the lowest contribution to their ratio change. The following equation allowed the calculation of the ratio change ΔR in response to depolarization:

$$\Delta R = \frac{\int_{\lambda_{C1}} E_{depolarized} d\lambda / \int_{\lambda_{C2}} E_{depolarized} d\lambda}{\int_{\lambda_{C1}} E_{resting} d\lambda / \int_{\lambda_{C2}} E_{resting} d\lambda} - 1 \quad (3.2)$$

here the $E_{resting}$ and $E_{depolarized}$ were the fluorescence spectrum of di-8-ANEPPS in the resting and depolarized state of the cells, respectively. For other symbols refer to equation 3.1. Optimized filters were used in Hardy's apparatus to eliminate the central spectrum area of di-8-ANEPPS emission, and their ratio change was 6.2%. In our setup we could obtain a ratio change of 6.1%. From this it was apparent that the detection bandwidths of the green channel and the red channel could be widened without compromising the ratio change of the di-8-ANEPPS signal.

The optimized detection bandwidths of di-8-ANEPPS signal and the increased photon detection efficiency enabled us to record individual cellular action potentials of cardiomyocytes without data averaging at an acquisition speed of 1000 Hz. Furthermore, dye-loading could also be shortened (here 7 min vs. 20 min in Hardy et al). This also minimized the potential effects of di-8-ANEPPS itself (if any) on the AP. Typical traces from such an experiment are presented in Figure 3.2.

3.1.4 Evaluation of di-8-ANEPPS

As for other sensors, the question arises to what extent the sensor disturbs the native system. To address this question, the APs of cardiomyocytes recorded with di-8-ANEPPS were compared with signals recorded with the gold standard, the patch-clamp technique. This was done by combining a patch-clamp setup with the optical AP-recording setup, with which Dr. Martin Oberhofer induced an AP via a patch pipette and I simultaneously recorded the AP. Figure 3.3A displays that APs measured with both methods were superimposable. Even the stimulation artifact could be recorded nicely with this optical approach (see arrow in figure 3.3A).

In order to directly translate the properties of optically recorded APs into real APD values, it was essential to establish a linear relationship between the ratio changes of di-8-ANEPPS and the changes of the real membrane potential. As figure 3.3B shows, the application of linear voltage ramps clearly showed a linear response of the fluorescent probe.

The next important question to address was, whether di-8-ANEPPS itself would alter the properties of cardiac APs. Hardy et al. reported that di-8-ANEPPS did not affect resting membrane potential and AP amplitude, but the AP duration⁷⁸. We therefore compared APDs obtained from optical recordings (hashed bars in figure 3.3C) with those measured in patch-clamp experiments

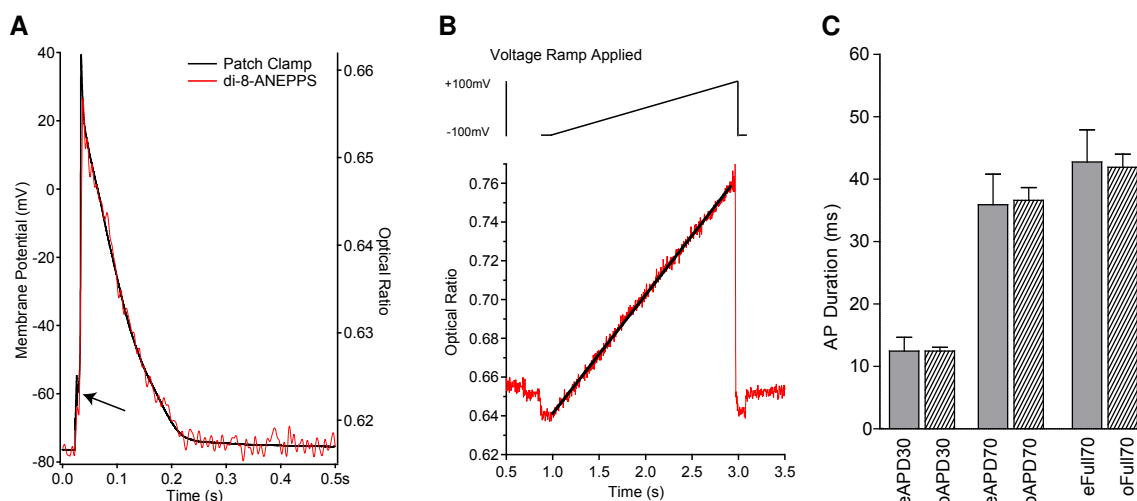


Figure 3.3: Evaluation of di-8-ANEPPS-based measurements. Panel **A** compares AP recordings by photometry (red trace) with those by simultaneous patch-clamp measurements (black trace). **B**, the fluorescence ratio (red trace) showed a linear relationship to the linear voltage ramp (black trace on the top). Panel **C** depicts a comparison of optical (prefix “o”) APDs and these measured by patch-clamp (prefix “e”) in two population of rat cardiomyocytes. Full₇₀ represents the sum of upstroke time and decay time. oAPD were from 214 cells/8 rats, eAPD from 94 cells/14 rats. The electrophysiological data in A and B and partial data in C and were recorded by Dr. Martin Oberhofer, the rest electrophysiological data in C were recorded by Ms. Sara Pahlavan.

(gray bars in figure 3.3C). There was no significant difference between these two methods. From these results we concluded, that under these optimized experimental conditions (more sensitive detectors, wider detection wavelengths and decreased dye loading time) di-8-ANEPPS enabled optical AP recordings without altering AP properties.

3.1.5 Characterization of action potential prolongation in adult and neonatal cardiomyocytes induced by drugs

The next question I addressed was, whether such an approach could be adapted to evaluate the effects of various drugs on the kinetic properties of cardiac APs. Within such experiments, I also wanted to investigate whether the kinetic properties of APs changed differently in adult and neonatal cardiomyocytes. All this should eventually enable us to address the question whether AP recordings by optical methods could be developed into a screening approach for QT-interval evaluation.

For this, a set of substances (quinidine^{175,236}, 4-AP^{105,228} and E-4031^{201,211}, shown in figure 3.4) with well-known effects on cardiac APs was chosen to (i) evaluate whether optical AP recordings could indeed identify characteristic changes in APs and (ii) investigate potential differences between adult and neonatal cardiomyocytes.

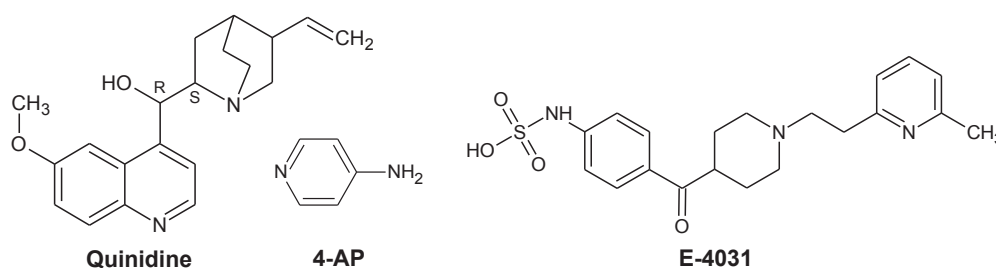


Figure 3.4: Compound structures of quinidine, 4-aminopyridine (4-AP) and E-4031.

3.1.5.1 Traditional strategy of substance evaluation

Traditionally, three-step protocols are used to investigate the effects of test substances on AP characteristics. A pre-application recording of APs is usually followed by measurements of APs in the presence and finally after washout again in the absence of the test substance. However, such a complex and long-lasting protocol could not be employed for the optical recordings due to the following considerations:

- i Illumination toxicity. Long lasting excitation of di-8-ANEPPS loaded cardiomyocytes resulted in changes of the AP properties (see figure 3.5A). Most likely, photochemical byproducts (e.g. radicals) could account for such changes.
- ii Long lasting pacing resulted in unexpected changes in the AP properties, that might be due to minute changes in the autofluorescence or spatial arrangement of the myocytes in the recording window. Repetitive contraction-relaxation cycles could slightly move the cell on the coverslip. (See figure 3.5B).
- iii APs displayed altered properties after washout of test substances that should be readily reversible, such as quinidine. Such problems might result from effects described under (ii). (See figure 3.5C).

Due to these reasons, it was very difficult to get reliable data (figure 3.5), which led to a very low rate of successful experiments (less than 20%). Furthermore, the traditional protocol was time-intensive with minimum 5 minutes to finish an entire protocol of substance evaluation. A even worse problem was that a substance application could affect the basal AP of the next cell, such that only one cell could be used for every coverslip/well, which was very inefficient.

3.1.5.2 Well-to-well strategy of substance evaluation

In order to perform an efficient substance evaluation, I picked a work flow that based on a well-to-well procedure. In this strategy, one well or coverslip served as the “control”, another one was

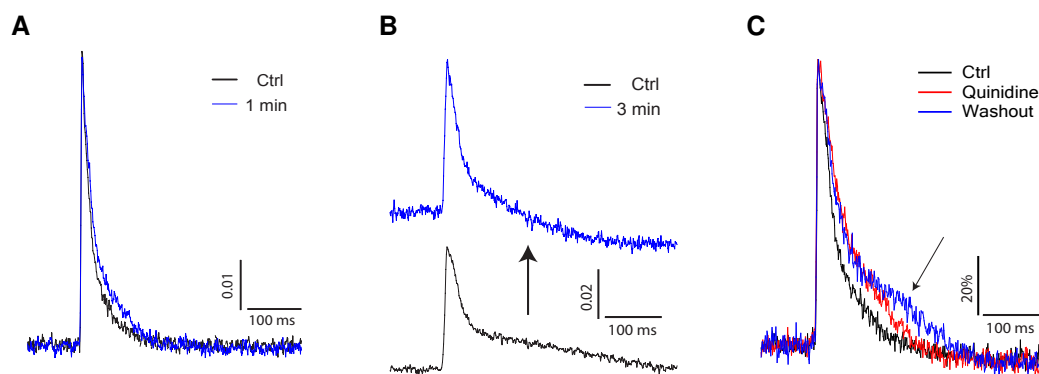


Figure 3.5: Problems in traditional strategy of substance evaluation. Panel **A** shows the AP difference after 1 minute of illumination and pacing on mouse ventricular myocyte. **B** shows the action potential differences after 3 minutes of pacing (without illumination) on rat ventricular myocyte. **C**, quinidine (10 μM) was tested with a traditional strategy of substance evaluation. Arrow shows the unexpected changes of the measured AP.

treated with specific concentrations of compounds to serve as the “treatment”. For every well or coverslip 20 ~ 30 cells were measured at random, and all the APD values were averaged and used as the final APD value. This strategy represented a screening-compatible strategy, and could be scaled up easily if faster readout devices or approaches could be adapted.

3.1.5.2.1 Substance evaluation with adult rat cardiomyocytes

In our manual procedure all the operations including selecting single myocytes, adjusting the focus, starting the illumination, starting the recording and stopping the illumination, could be accomplished in 30 ~ 40 seconds, that is, 30 recordings would need less than 20 minutes. Possible time-dependent AP alterations in the same well were minimized, since a safe time window was 30 minutes (data now shown).

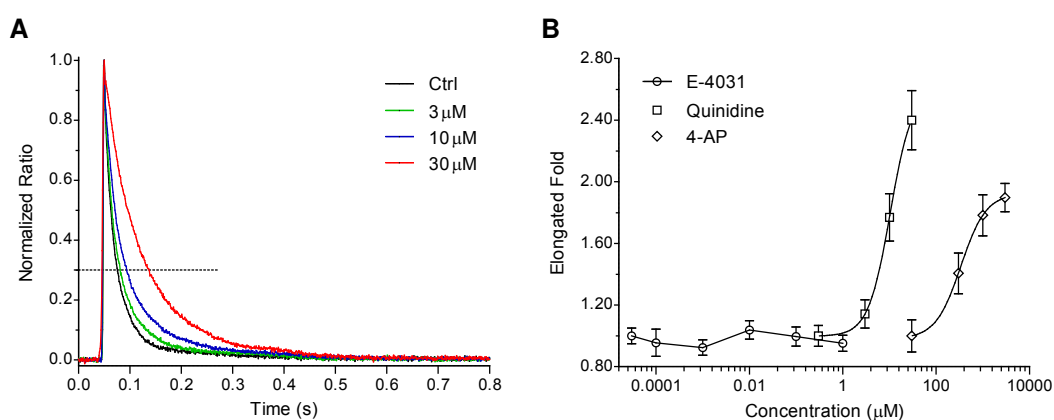


Figure 3.6: Well-to-well strategy of substance evaluation with adult myocytes. **A**, averaged traces of APs with quinidine treatments on rat adult ventricular myocytes; dashed line shows the position of APD₇₀. **B**, concentration response curves of quinidine, E-4031 and 4-AP with adult rat ventricular myocytes.

As depicted in figure 3.6A, quinidine prolonged AP in a concentration-dependent manner. The final IC_{50} for AP prolongation was $10.36 \mu\text{M}$ (figure 3.6B). At this IC_{50} concentration, the average AP was prolonged from 30.0 ms to 53.8 ms, increased by 79.6%. 4-AP also showed a concentration-response behavior with an IC_{50} of $340 \mu\text{M}$ (figure 3.6B). For E-4031 there was no concentration-dependent effect on adult rat ventricular myocytes (figure 3.6B).

3.1.5.2.2 Substance evaluation with neonatal rat cardiomyocytes

As described above, neonatal cardiomyocytes are a popular cellular model, since handling of these cells is really simple. Therefore, the next question I addressed was whether the strategy developed so far also worked with neonatal cardiomyocytes. Unfortunately, in initial test recordings I observed that cell-to-cell variability of neonatal cardiomyocytes was increased when compared to adult cells (see the independent neonatal clusters in figure 3.7B). Interestingly, this variability did apparently depend on the coupling status of the cells: cells in small clusters displayed a large variability while cells in large coupled areas depicted a rather tight distribution of AP parameters (figure 3.7Bb). This was most likely due to some instabilities in the electrophysiological properties of individual cells or small clusters that were stabilized and synchronized by concerted activity of large cell areas.

Therefore, AP recordings of neonatal cells were performed only after the majority of the cells were electrically coupled, as shown in figure 3.7Ab, and identified by the spontaneous beating of very large areas of neonatal myocytes. As depicted in figure 3.8B, quinidine showed a concentration-response curve with neonatal cardiomyocytes (IC_{50} was $8.70 \mu\text{M}$), that was in a very good agreement with the findings for adult cells (figure 3.8B). At the IC_{50} , the APD_{70} was changed from 287.3 ms to 347 ms (20.8% increase), an effect that was much lower than that for adult cells (79.6%). For 4-AP similar results were obtained with neonatal cells (figure 3.8B). Different to the effects with adult myocytes, E-4031 showed a concentration-response curve (figure 3.8B) on neonatal myocytes with an IC_{50} of 11.4 nM.

3.1.5.2.3 Summary of the application of di-8-ANEPPS

Table 3.1 summarizes the major findings of this part of my thesis.

3.1.6 Properties of Mermaid and its application on rat adult cardiomyocytes

Recently, a promising genetically encoded biosensor, the “Mermaid”, became available²¹⁴. Such biosensors possess a number of advantageous properties over traditional chemical sensors in long-term usage, for example repetitive recordings of the same cell over days.

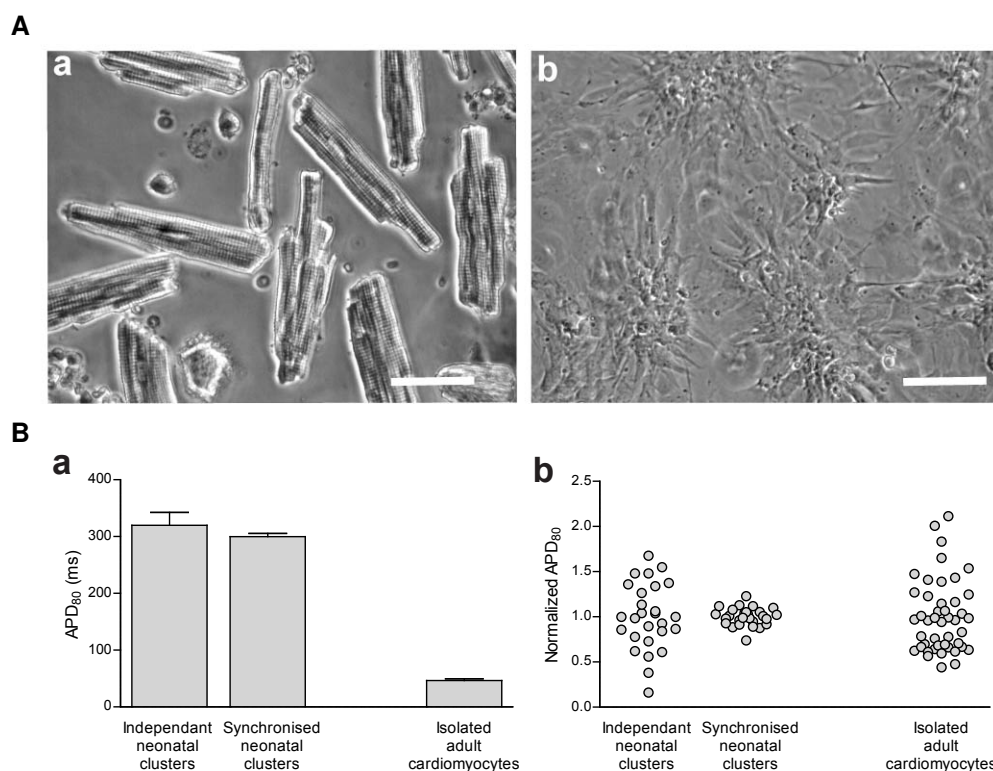


Figure 3.7: Comparison of neonatal and adult ventricular myocytes. Panel **A** shows morphologies of adult (a) and neonatal (b) rat ventricular myocytes. Scale bar, 50 μm . Panel **B** depicts the APD₈₀ from the neonatal and adult ventricular myocytes (a), and their distributions (b).

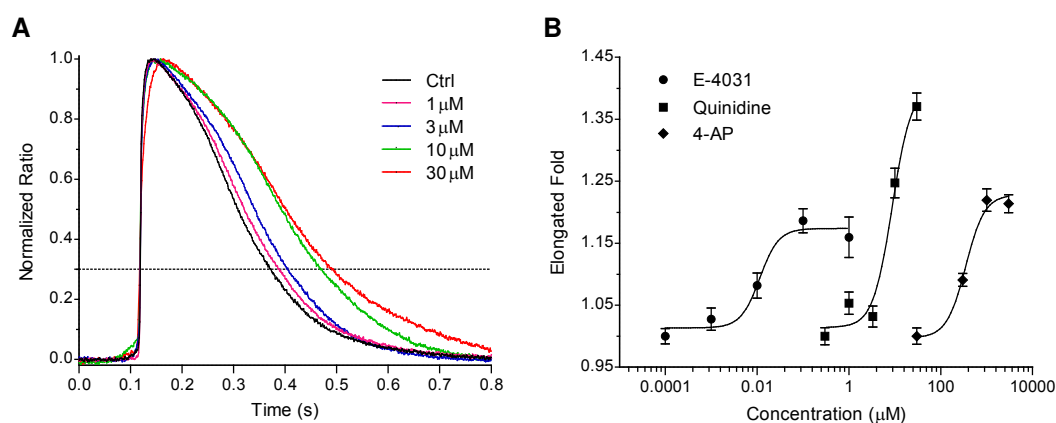


Figure 3.8: Well-to-well strategy of substance evaluation with neonatal myocytes. **A** depicts representative traces averaged from 20 ~ 30 individual APs from the same preparation in the presence of quinidine at the given concentrations. Dashed line shows the position of APD₇₀. **B** summarizes concentration-response relationships for the substances listed in the symbol legend.

3.1.6.1 Protein structure and working principle

Mermaid protein comprised a voltage-sensitive domain (VSD) followed by two fluorescent proteins in tandem²¹⁴. These two fluorophores, mKUG and mKO κ , constitute a Förster Resonance Energy Transfer (FRET) pair and respond to the conformation changes of the VSD. The VSD in-

Table 3.1: Effects of test compounds on APs in cardiomyocytes

Items	Cell Type	E-4031	4-AP	Quinidine
IC ₅₀ (μM)	Adult	–	339.8	10.36
	Neonate	0.0114	349.6	8.697
Resting APD ₇₀ (ms)	Adult	29.29	45.97	36.33
	Neonate	278.0	277.7	291.5
APD ₇₀ @IC ₅₀ (ms)	Adult	–	67.64	65.32
	Neonate	300.3	309.8	347.9
Maximum APD ₇₀ Prolongation folds	Adult	–	0.943	1.596
	Neonate	0.160	0.231	0.387
Analyzed preparations	Adult	3	3	3
	Neonate	3	3	3
Number of analyzed cells	Adult	≥ 360	≥ 210	≥ 160
	Neonate	≥ 410	≥ 290	≥ 290

serts into the cell membrane, and consequently responds to the voltage changes across the cell membrane, as shown in figure 3.9A. Since it was a FRET based construct, it allowed ratiometric measurements and hence had the potential to be used with cardiomyocytes, such that contraction artifact could be diminished.

For expression of genetically biosensors in cardiac myocytes, viral systems need to be applied since conventional transfection techniques only give low protein expression. We thus constructed an adenovirus based on the original plasmid provided by the Miyawaki Group²¹⁴. Transfection into COS cells resulted in strong expression of the voltage sensor construct in the plasma membrane enabling us to characterize fluorescence properties similar to those approaches described for di-8-ANEPPS (see figure 3.1). Similar to the small molecular dye, Mermaid also displayed a “ratiometric” behavior: upon depolarization of Mermaid expressing COS cells, the mKUG fluorescence decreased while the that of mKOκ increased (see figure 3.9A) resulting in a difference spectrum as illustrated in figure 3.9B. Based on these spectral results we picked a dichroic mirror centered at 532 nm to separate the donor fluorescence (green channel) from the acceptor signal (red channel).

3.1.6.2 Expression pattern of Mermaid on rat ventricular myocytes

Similar to di-8-ANEPPS, Mermaid was used with an photometric approach. For this it was essential to verify the membrane localization of Mermaid. Cardiomyocytes were transduced with the Mermaid virus and the subcellular distribution was investigated with high-resolution confocal microscopy.

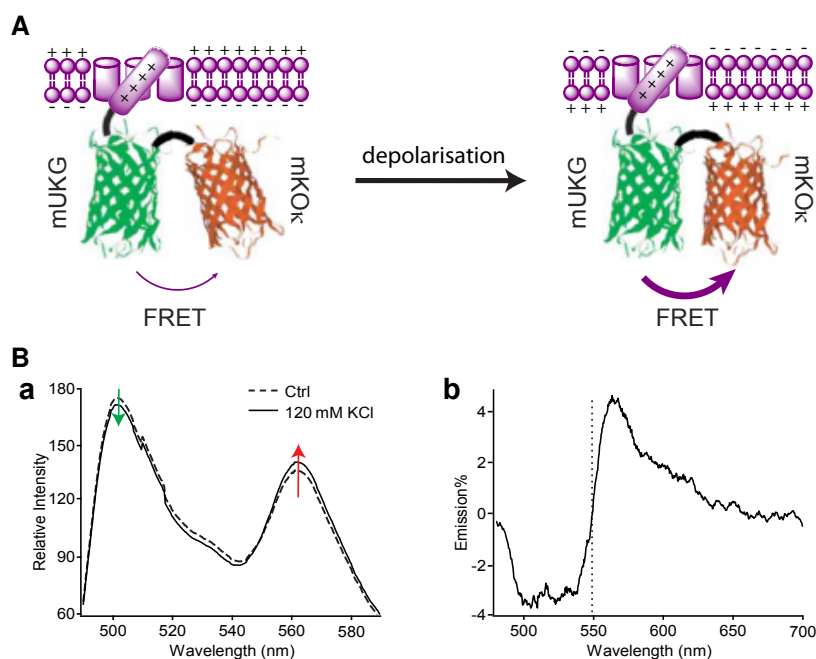


Figure 3.9: The structure of Mermaid and its working principle. **A**, Mermaid comprises a voltage sensing domain and a FRET pair, mKUG and mKO κ . At resting state, the FRET was weak; when the cell membrane was depolarized, the distance between the two fluorophores decreased, resulting in higher FRET efficiency. **B**, the emission spectra of Mermaid in normal (5.4 mM, average of 6 cells) and high concentration of K⁺ (120 mM, average of 6 cells) and their difference spectrum are shown in B(a) and B(b), respectively. Arrows in B(a) show the changing direction of the spectra upon depolarization. Spectra were measured on COS cells transduced with Mermaid-adenovirus.

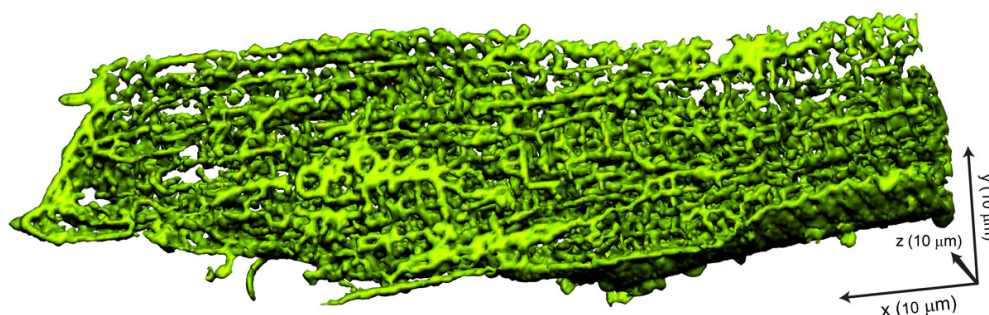


Figure 3.10: The expression pattern of Mermaid on ventricular myocytes. Rat ventricular myocytes were infected with Mermaid-adenovirus immediately after being isolated. Three days later, these myocytes were scanned on a confocal microscope, and their 3D structures were rendered.

The resulting z-stacks were deconvolved and subjected to surface 3D rendering (see section 2.3.1). Figure 3.10 illustrates a typical myocyte expressing Mermaid. From the morphology of the surface rendered object it appeared rather likely that Mermaid preferentially localized in the plasma membrane, highlighting the complex structure of the T-tubular system.

To confirm the distribution of Mermaid, we investigated co-localization of Mermaid with di-8-ANEPPS, which is well known to specially label the cell membrane¹⁹⁸. However, the emission

spectra of di-8-ANEPPS and Mermaid overlapped severely, as shown in figure 3.11. Fortunately we could identify two spectral regions in which either di-8-ANEPPS fluorescence (660 ~ 720 nm) or Mermaid fluorescence (480 ~ 498 nm) dominated. Emission at those spectral regions were used to evaluate co-localization (see figure 3.11).

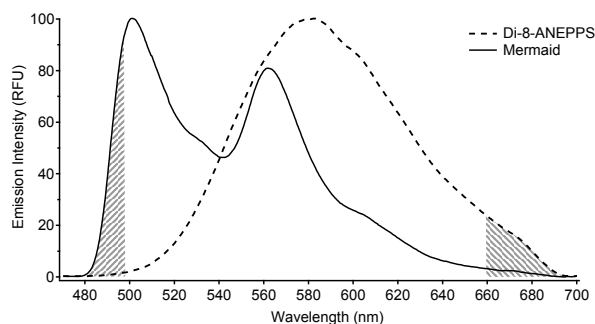


Figure 3.11: Comparison of Mermaid and di-8-ANEPPS emission spectra. Hashed parts at 480 ~ 498 nm and 660 ~ 720 nm denote spectral regions in which Mermaid and di-8-ANEPPS fluorescence dominated.

Figure 3.12 summarizes the results of such a co-localization study. While panel A and B depict the good spectral separation for Mermaid (figure 3.12A) and di-8-ANEPPS (figure 3.12B) when used individually, figure 3.12C illustrates the superimposition of the emission bands in cells stained with di-8-ANEPPS and expressing Mermaid. There were distinct differences in the distribution, most notably in the perinuclear regions where mermaid fluorescence dominated. This result was not entirely unexpected since Mermaid is an expressed protein and its fluorescence ought to appear on the Golgi apparatus surrounding the nuclei before correct targeting of the protein into the plasma membrane. A statistical analysis (data not shown) indicated that around 20 ~ 30% of the Mermaid fluorescence did indeed originate from non-membrane (i.e. di-8-ANEPPS free) locations. This fluorescence will not contribute to the changes induced by the membrane potential since most likely these locations are not connected to the plasma membrane. In addition, we could find vesicles that were Mermaid positive but di-8-ANEPPS negative, most likely there were Golgi-transport vesicles, but in general they were rather sparse.

3.1.6.3 The response of mermaid to action potentials

Since Mermaid was expressed mainly on the membrane of adult cardiomyocytes, I next examined the response of Mermaid to APs in adult cardiomyocytes. At room temperature, Mermaid did not show any response to AP despite of clear contractions (data not shown).

Thus all the kinetic experiments of Mermaid were performed at 37 °C with 20 mM BDM[†] to

[†]2,3-butanedione monoxime.

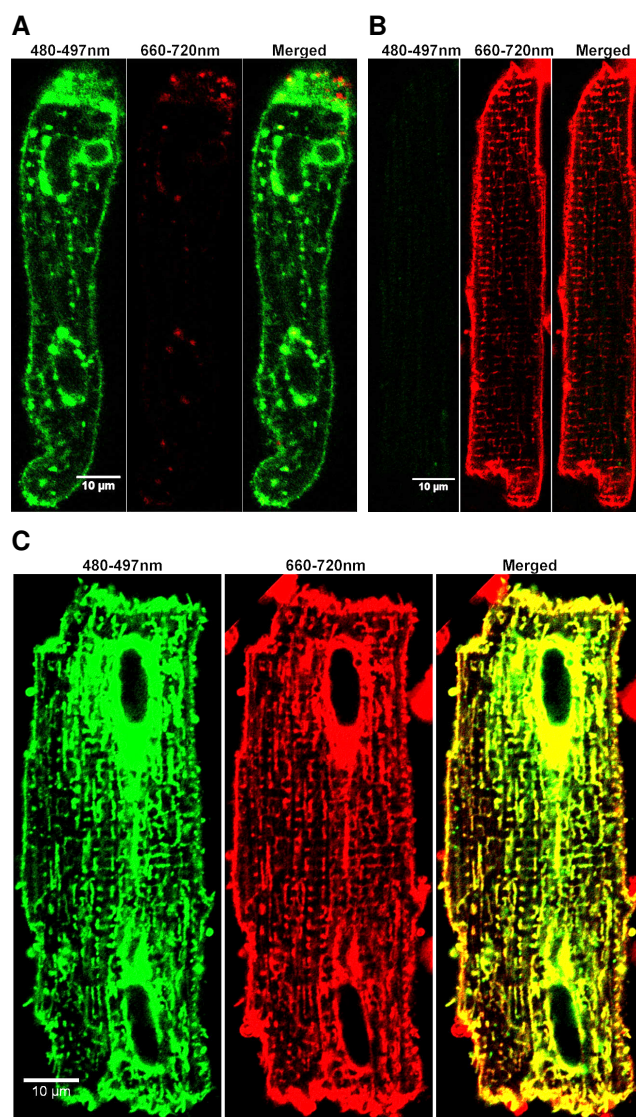


Figure 3.12: Colocalization of Mermaid and di-8-ANEPPS. **A**, Mermaid only. **B**, di-8-ANEPPS only. **C**, Cells transfected with Mermaid and loaded with di-8-ANEPPS.

completely inhibit cell contraction¹⁵³. The signals from the donor channel and the acceptor channel displayed opposite intensity changes upon membrane depolarization, resulting in a ratioed trace that looked like a typical rodent AP (figure 3.13A). It was also notable that the intensity signal bleached quickly during the measurements, while the ratioed signal almost neutralized the distortions in the raw signals. Further measurements showed that Mermaid was able to discriminate the prolongation of AP induced by 10 μM quinidine, as shown in figure 3.13B.

3.1.6.4 Kinetic comparison of di-8-ANEPPS and Mermaid

Our observations, that Mermaid was not able to follow APs at room temperature, highly implied potential kinetic problems for Mermaid. In comparison to di-8-ANEPPS, in which electrons shift

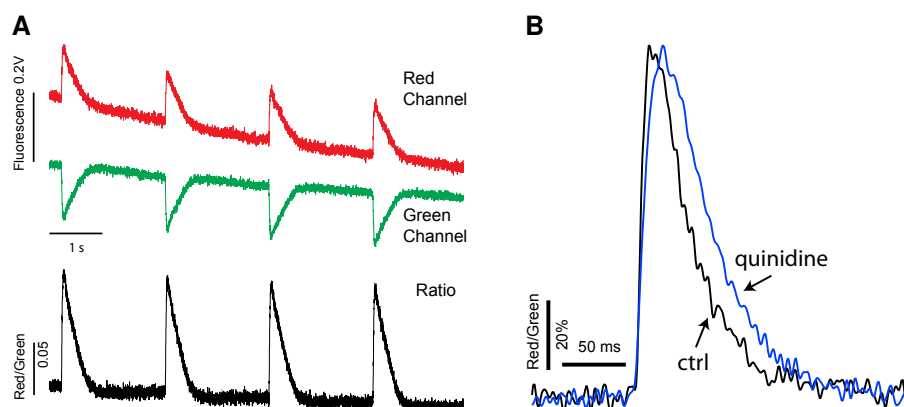


Figure 3.13: The response of Mermaid to action potentials. **A**, two days after the transfection with Mermaid-adenovirus, adult rat ventricular were steadily paced with field stimulation and excited with at 460 nm. The emission of Mermaid was split at 532 nm and the resultant two channels were recorded simultaneously. The raw signals and their ratio are shown in top panel and bottom panel, respectively. **B**, APs signals measured with Mermaid from the same myocyte before and after the application of 10 μ M quinidine.

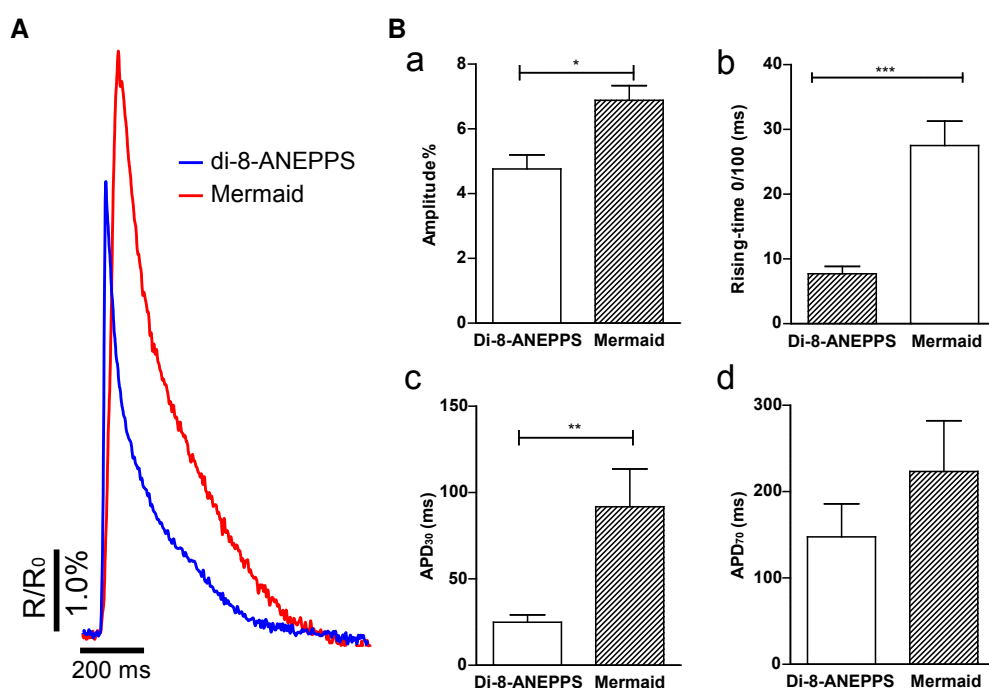


Figure 3.14: Comparison of Mermaid and di-8-ANEPPS kinetics. Panel **A** shows the comparison of the AP signals measured with Mermaid (average of APs from 4 cells) and di-8-ANEPPS (average of APs from 7 cells). Panel **B** shows the AP amplitudes (a) and kinetic behaviors of the AP signals measured with Mermaid and di-8-ANEPPS, including the upstroke time (b), APD₃₀ (c) and APD₇₀ (d).

in response to membrane potential changes, in the Mermaid protein the two fluorophores most likely were twisted against each other, a rearrangement that is thought to be much slower.

I therefore designed experiments to compare the kinetic properties of Mermaid expressing

and di-8-ANEPPS labeled cardiomyocytes. For this I recorded typical APs from both kind of cells under otherwise identical conditions and superimposed them (see figure 3.14A). From this direct comparison I concluded that Mermaid indeed displayed a significantly slower kinetic response in both, the upstroke and repolarization phase of the AP. A statistical comparison can be found in figure 3.14B. I was particularly surprised about the vastly prolonged repolarization of the AP signals.

3.1.7 Final remarks for this section

In this section I compared a small molecule and a genetically encoded sensor for membrane potential changes and found that the small molecule sensor was superior in both kinetic responses and ease-of-application. Di-8-ANEPPS changes displayed a linear relationship to the membrane potential over the entire potential range investigated. Under our optimized recording conditions this dye did not affect the shape of the AP itself. In contrast, the Mermaid signal illustrated a rather distorted AP, most likely due to a rather slow kinetic response, that would be rather difficult to deconvolve since the upstroke was affected to a lesser degree than the repolarization phase.

3.2 The effects of CytoD in the culture of cardiomyocytes

3.2.1 Dynamic changes of Ca²⁺ transients of cardiomyocytes during long-term culture

After isolation, adult cardiomyocytes undergo significant remodeling both in structure¹³⁷ and in function⁷⁷. As a direct consequence of this remodeling, Ca²⁺ transients, the key mediator between AP and contraction, decrease gradually¹². To illustrate and investigate such remodeling processes, I evaluated the amplitude of electrically evoked steady-state Ca²⁺ transients in Fura-2 loaded ventricular myocytes from adult rat hearts that were plated onto ECM-coated coverslips and cultured in serum-free medium supplemented with ITS (see Materials and Methods).

A camera-based video imaging system was designed to measure Ca²⁺ transients from multiple cardiomyocytes simultaneously. Subsequently those data were processed with custom-made macros in Igor Pro software to automatically calculate physiological parameters, including amplitudes, basal Ca²⁺ concentrations and 80% duration of the Ca²⁺ transients, which enabled us to characterize the Ca²⁺ cycling of cardiomyocytes quickly and to analyze large amount of data in a reasonably short time (see Materials and Methods for more details).

Figure 3.15A depicts typical transients recorded during the first 3 days in vitro and shows that

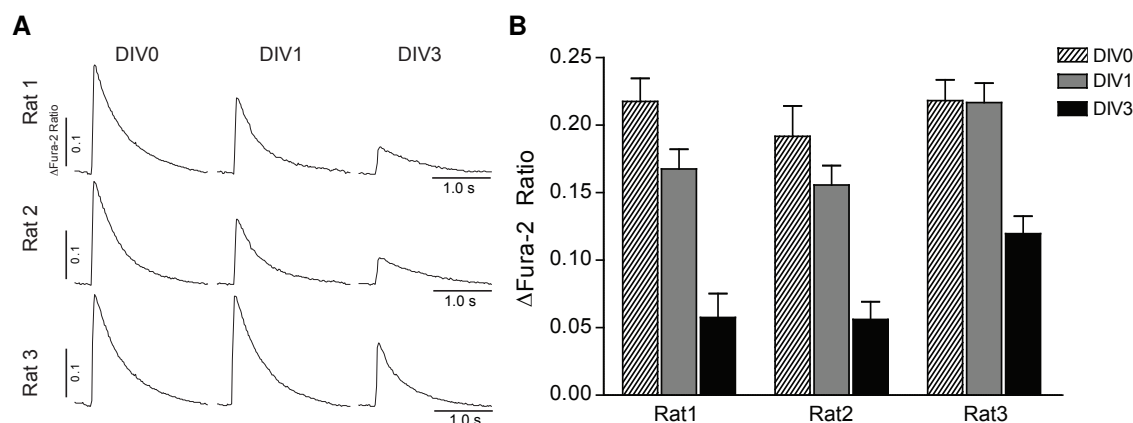


Figure 3.15: Dynamic changes of Ca²⁺ transients of cardiomyocytes during culture. Panel **A** shows the typical Ca²⁺ transients of adult rat ventricular myocytes at DIV0, DIV1 and DIV3. Panel **B** shows the amplitudes statistics of the Ca²⁺ transients measured at DIV0, DIV1 and DIV3 from ventricular myocytes of three different rats.

the amplitude was decreasing with culture time. This finding was also representative for a greater population of myocytes and rat hearts (figure 3.15B). At DIV3, the amplitude was usually reduced by almost 60%.

This part of my thesis describes experiments to investigate the remodeling processes as well as a novel approach to prevent or at least minimize such processes.

3.2.2 Culture-mediated changes in Ca²⁺ transients can be prevented by CytoD

In the past, several groups have reported an approach to minimize such culture-dependent remodeling processes. Interestingly, it was reported that CytoD (40 μM) was able to suppress remodeling of isolated adult cardiomyocytes up to 96 hours¹¹⁹. In addition to Ca²⁺ cycling, CytoD could also preserve the actin cytoskeleton, as well as the distribution of LTCCs and RyRs up to 48 hours¹¹⁹. However, no quantitative data on Ca²⁺ cycling or possible mechanisms were provided or investigated.

Usually high concentrations of CytoD (e.g. 20 ~ 40 μM) were used as F-actin disruptor or mechanical uncoupler^{9,20,237}. But this seemed to be controversial: CytoD (40 μM) disrupts F-actin³⁵, while it was also reported to preserve the F-actin structure¹¹⁹. I thus set out to investigate those possible actions and address the question whether CytoD would indeed help in preserving morphology and function of cultured adult cardiomyocytes. My starting point was the concentration described in the literature: 40 μM. I again used the Ca²⁺ transients as a readily available integrating parameter for cardiomyocytes function. Figure 3.16 summarizes such data. While at DIV0 Ca²⁺ transients were not significantly altered by the CytoD, the decreasing transient amplitude reported for DIV3 cells was diminished, myocytes cultured in the presence of CytoD displayed an

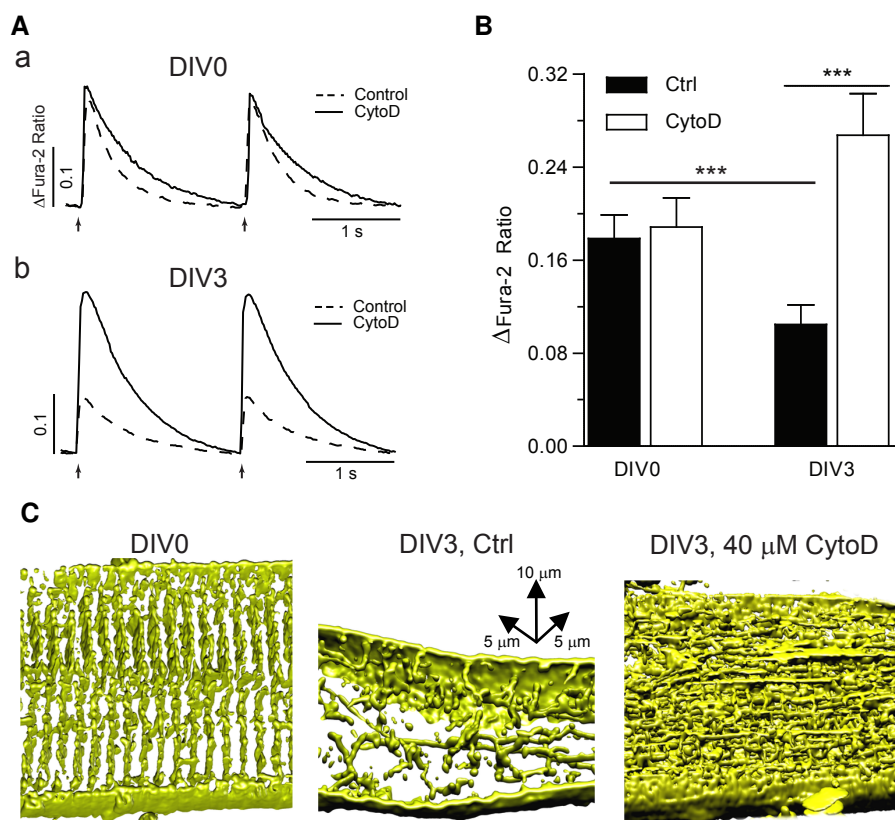


Figure 3.16: Effects of CytoD (40 μ M) on Ca^{2+} transients and on membrane topology. **A**, typical traces of Ca^{2+} transients at DIV0 (a) and DIV3 (b) from rat ventricular myocytes cultured with or without 40 μ M CytoD. Arrows show the electrical stimulation pulses. **B**, statistics of the 40 μ M CytoD effects on the amplitudes of Ca^{2+} transients. **C**, T-tubule structure reconstructions for representative cells from DIV0 and DIV3.

even higher amplitude than that found originally at DIV0 (see figure 3.16Aa vs. b; see also figure 3.16B).

Since cardiac EC-coupling is majorly influenced by the microarchitecture of the T-tubular system and a rapid loss of T-tubules during myocytes culture was already reported earlier¹²², we wondered how 40 μ M CytoD would interact with this T-Tubular remodeling. For this, I reconstructed the T-tubular system of ventricular myocytes after labeling the plasma membrane with di-8-ANEPPS as detailed in figure 3.16C. The results illustrate that in the absence of CytoD (figure 3.16C, middle panel) T-tubules were largely lost while CytoD was able to prevent this effect (compare left and right panel in figure 3.16C). Nevertheless, a detailed analysis of the plasma membrane topology revealed that in the presence of such a high concentration of CytoD their regular arrangement was apparently diminished leading to what we called “membrane crowding”. In addition, 40 μ M CytoD also altered the AP as investigated in simultaneous patch-clamp experiments. Both APD_{30} and APD_{50} were significantly prolonged (experiments performed by Ms. Sara Pahlavan, data not shown).

3.2.3 Concentration-dependent action of CytoD on Ca^{2+} cycling in adult cardiomyocytes

Thus up to now, a concentration of 40 μM CytoD displayed both beneficial effects (preservation of Ca^{2+} cycling) and unwanted effects (T-tubular crowding). I thus wondered whether such effects were indeed concentration-dependent and in the end one could find an “optimized” CytoD concentration that would allow preservation of Ca^{2+} cycling, T-tubule architecture and AP characteristics, but avoid introducing extra effects like T-tubule crowding. Therefore, I set up an experimental series to investigate the lowest possible CytoD concentration that optimally preserved Ca^{2+} cycling. This series would consist of two steps: (i) finding an optimal concentration by means of Ca^{2+} transient amplitude screening (see above), and (ii) thorough in-depth analysis of the identified CytoD concentration to verify its action.

3.2.3.1 Concentration-dependent effects of CytoD on Ca^{2+} cycling during 6 days of culture

Rat adult ventricular myocytes were cultured for 6 days either in the absence (Ctrl condition) or in different concentrations of CytoD (ranging from 0.04 to 1.2 μM). Steady-state Ca^{2+} transients were analyzed and their amplitudes displayed a concentration and culture-dependent modulation, as summarized in figure 3.17. It was apparent that there was no single optimal concentration that can preserve the Ca^{2+} cycling from DIV0 to DIV6. When considering DIV3 (filled black circles) the intersection with the DIV0 curve (open circles in figure 3.17B) represented an optimal concentration of 0.4 ~ 0.6 μM . In contrast, when we considered the DIV6 data (open squares) a concentration well above 1.0 μM appeared to preserve the amplitude the best.

Expression of exogenous proteins in cardiomyocytes with an adenoviral system as already introduced for Mermaid (see above) never required longer culturing than 3 days. I thus set out to consider the concentration response curve at that time point for determination of the optimal CytoD concentration. From this I concluded, that a concentration of 0.5 μM CytoD as a culture supplement could be considered optimal.

3.2.3.2 Thorough investigation of the effects of 0.5 μM CytoD on cardiac Ca^{2+} cycling

As explained above the second set of experiments ought to provide an in-depth analysis of the effects of the optimal CytoD concentration on Ca^{2+} cycling. For this I employed a post-rest behavior protocol that comprised two recording periods. The first period included a resting time after which electrical stimulation was started. Stimulation continued in the absence of fluorescence

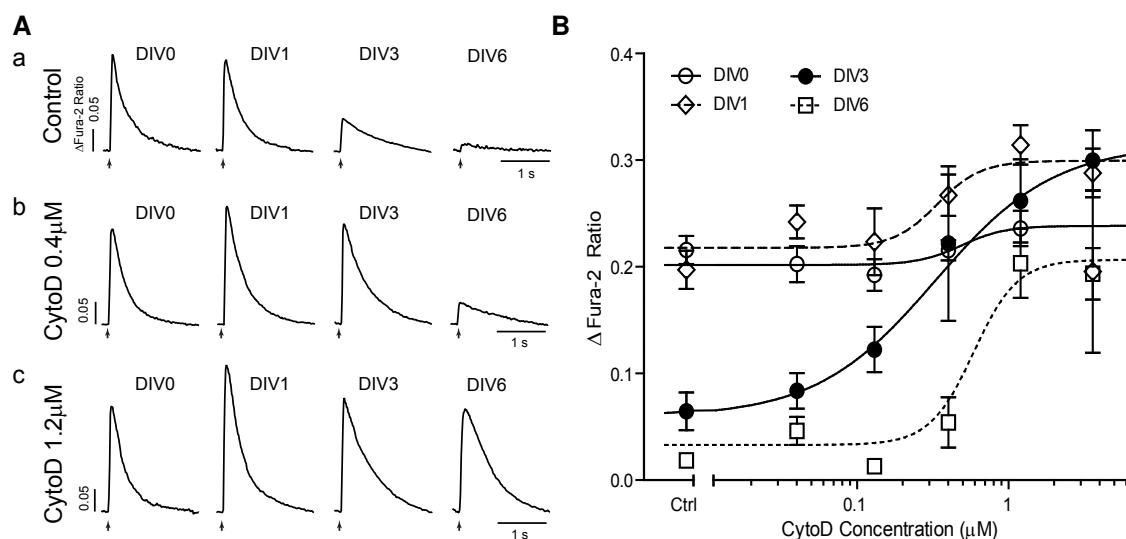


Figure 3.17: Concentration response of CytoD effects on cardiac Ca^{2+} transients. **A**, typical traces of Ca^{2+} transients from cardiomyocytes cultured with control (a), 0.4 μM (b) and 1.2 μM (c) CytoD at DIV0, DIV1, DIV3 and DIV6. Arrows show the electrical field stimulations. **B**, concentration response curve (sigmoidal) fitting of CytoD effects on the amplitudes of Ca^{2+} transients. Shown data was from one animal, two additional experiment replica confirmed these results. Experiments were performed by Ms. Katharina Oleinikow.

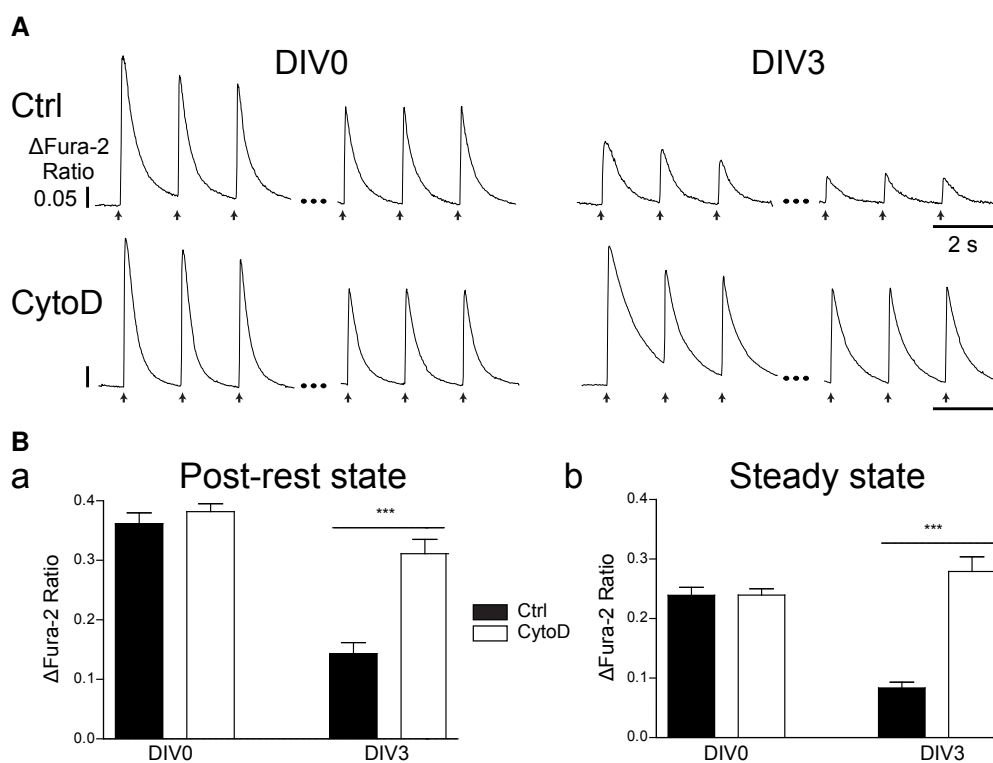


Figure 3.18: The effects of optimal CytoD on Ca^{2+} transients. **A**, typical traces of Ca^{2+} transients from cardiomyocytes treated with the optimal concentration of CytoD (0.5 μM) at DIV0 and DIV3; Arrows show the electrical field stimulations. **B**, statistics of the effects by the optimal concentration of CytoD on the amplitudes of post-rest (a) and steady-state (b) Ca^{2+} transients at DIV0 and DIV3.

excitation to gain steady-state conditions (3 minutes) after which a final recording period allowed investigation of steady-state Ca^{2+} cycling (see figure 2.1 for more details).

Figure 3.18 summarizes such experimental results performed at DIV0 and DIV3 in the absence and presence of 0.5 μM CytoD in the culture medium. It was apparent that under both conditions, post-rest and steady-state, the presence of CytoD in the culture medium preserved the amplitude of electrically evoked Ca^{2+} transients. It should be noted here that albeit CytoD was present in the culture medium, it was washed out before the cells were loaded with Fura-2/AM, thus the actual experiments were performed in the absence of CytoD under all conditions. These results highlighted and supported the beneficial action of 0.5 μM CytoD as a medium supplement during the culture of adult rat ventricular myocytes. In the following I used that concentration and investigated its action on Ca^{2+} removal mechanisms and cellular contractility.

3.2.4 Optimized concentration of CytoD preserved the contraction of cardiomyocytes in culture

Since CytoD was always used as a mechanical uncoupler and EC-coupling disruptor, and now I already knew that it could preserve Ca^{2+} cycling, I wondered whether the optimal concentration of CytoD would affect the contraction of cardiomyocytes.

As the typical contraction traces (figure 3.19A) show, the optimal concentration of CytoD did not disrupt, but did preserve the contraction of cardiomyocytes, similar to the preservation of the Ca^{2+} transients. Subsequent statistics of the contraction amplitudes confirmed these results (figure 3.19B). Furthermore, even the kinetics of contraction were well preserved with the optimal concentration of CytoD, as shown in figure 3.19C, including the time to full contraction, the post-rest duration of 80% full contraction (CD_{80}) and the steady state CD_{80} .

Based on these results, I concluded that the optimal concentration of CytoD could preserve the Ca^{2+} cycling of cardiomyocytes up to 3 days, while leaving the contraction untouched.

3.2.5 Effects of the optimized CytoD concentration on cardiac Ca^{2+} signaling

To further characterize the effects of the optimized CytoD concentration on cardiac Ca^{2+} signaling, I developed a detailed function profiling with caffeine (figure 3.20). For this a protocol combining field stimulation and brief caffeine applications was used to characterize various components in Ca^{2+} handling, as illustrated in figure 2.2. In this protocol several different parameters could be investigated simultaneously: i) amplitudes of Ca^{2+} transients in steady state; ii) SR Ca^{2+} contents in steady state from the amplitude of caffeine-induced Ca^{2+} transients; iii) NCX activity during

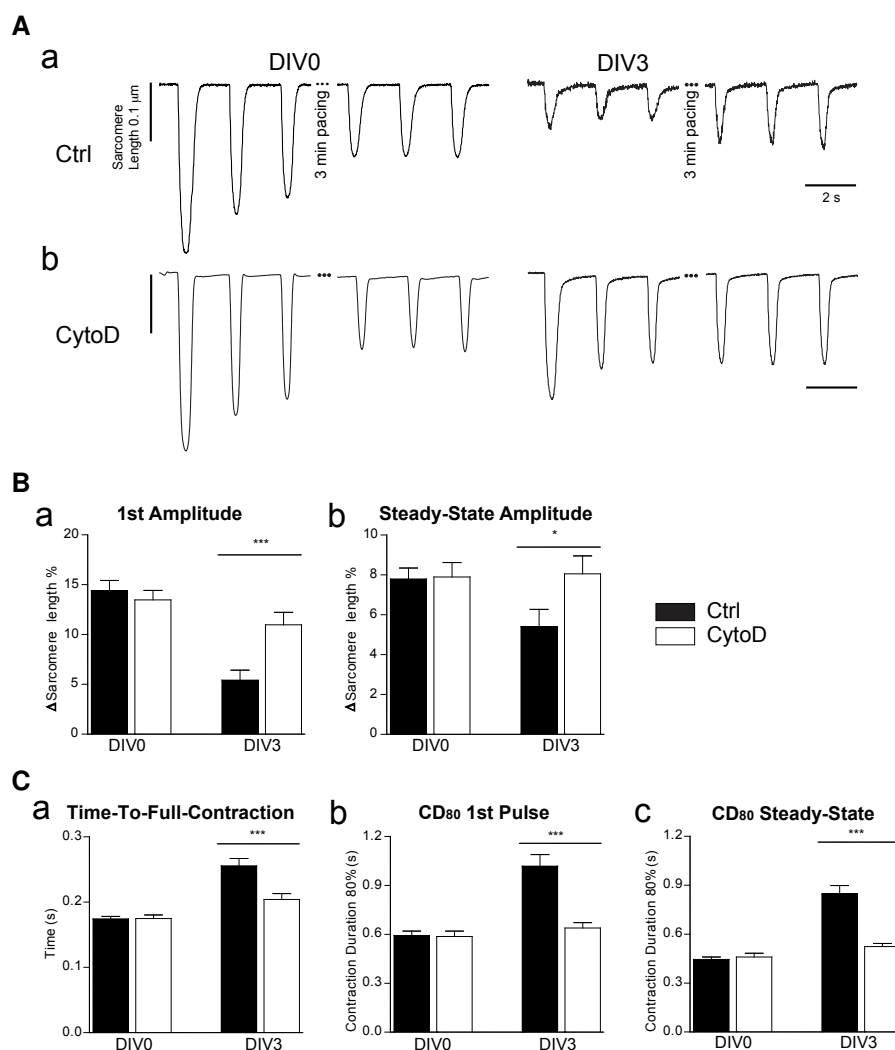


Figure 3.19: Effects of the optimal CytoD on the contraction of cardiomyocytes. **A**, typical contraction traces of rat adult cardiomyocytes from DIV0 and DIV3 in the absence (a) or presence (b) of 0.5 μ M CytoD. **B**, statistics of contraction amplitudes from the myocytes at post-rest (a) and steady states (b). **C** shows the kinetics of cell contraction, including the time to full contraction at steady states (a), duration at 80% full contraction (CD_{80}) at post-rest (b) and steady states (c).

steady state (the slow decay during caffeine application); iv) SERCA activity deconvolved from the decay phase of Ca^{2+} transients with the NCX τ as an input; and v) the fractional Ca^{2+} release ($f_{Ca^{2+}}$). The fractional Ca^{2+} release was calculated like:

$$f_{Ca^{2+}} = \frac{Amp_{steady\ state}}{Amp_{caf}} \quad (3.3)$$

where the Amp represented the amplitudes either from the electrically evoked transients (steady state) or from caffeine-induced transients.

For all Ca^{2+} transient measurements presented above the Ca^{2+} indicator Fura-2 was used, but since the Ca^{2+} bound and Ca^{2+} free form of Fura-2 are quenched differently by caffeine¹⁴⁴,

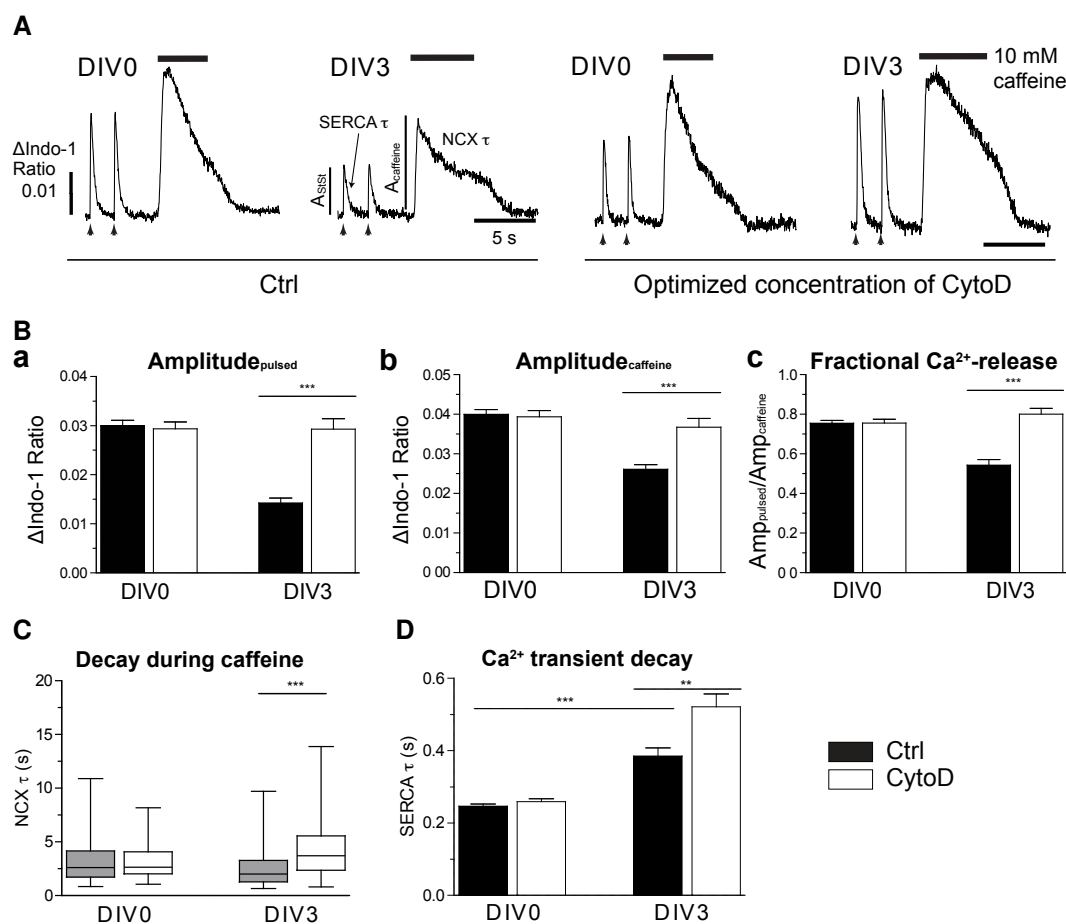


Figure 3.20: Effects of the optimal CytoD on the components of Ca²⁺ cycling. **A**, typical traces of caffeine-induced Ca²⁺ transients from cardiomyocytes treated with vehicle (Ctrl) and 0.5 μM CytoD at DIV0 and DIV3. Arrows indicate the electrical field stimulation. Panel **B** shows the amplitudes of Ca²⁺ transients stimulated with electrical field stimulations (a), 10 mM caffeine (b), and the resultant fractional Ca²⁺ release (c). Panel **C** shows the decay constants during the caffeine application (an indicator for NCX activity). **D**, the decay constants during the decay phase of Ca²⁺ transients (an indicator for SERCA, deconvolved with the NCX τ as an input). Note that the decay data for NCX did not follow Gaussian distribution nicely, so whisker's plot was used (marked median value with 5 ~ 95% percentile).

Fura-2 is not a suitable indicator together with caffeine applications. Here, Indo-1 is the indicator of choice. Although Indo-1 is also quenched by caffeine, this process does not affect the quantization of the the Ca²⁺ concentration (i.e. it does not change fluorescence ratios).

The experimental protocol described above allowed re-assessing the results on global electrically evoked Ca²⁺ transients already described for Fura-2. With Indo-1 I could confirm such results; while in the absence of CytoD the amplitude of steady-state Ca²⁺ transients declined significantly, CytoD was able to diminish such effects (see figure 3.20Ba). I obtained a first insight to the possible mechanisms behind that loss of amplitude in the absence of CytoD by analyzing the amplitude of caffeine evoked Ca²⁺ transients. In principle reduced electrically evoked Ca²⁺

signals could originate from two likely processes: (i) reduced Ca^{2+} influx during the AP or (ii) lower release of Ca^{2+} from SR by reduced SR Ca^{2+} content or decreased coupling efficiency between the LTCC and the RyR.

The analysis of the amplitude of caffeine induced Ca^{2+} transients revealed that in the presence of CytoD in the culture medium, the SR Ca^{2+} content was preserved and not significantly different to the DIV0 conditions (see figure 3.20Bb). Nevertheless, the decrease in the amplitude of electrically evoked Ca^{2+} transients appeared more pronounced than that of the caffeine-induced signals. I thus investigated the so-called fractional Ca^{2+} release, that indicates how much of the SR Ca^{2+} content is indeed release during electrical stimulation. Modulation of this parameter might hint to impairments of basic EC-coupling mechanisms. Figure 3.20Bc illustrates the results of such an analysis, suggesting that indeed, EC-coupling was impaired at DIV3 in the absence of CytoD, but that the supplement restored fractional Ca^{2+} release.

Caffeine-induced Ca^{2+} transients also allowed the analysis of the NCX function by investigating the decay time constant in the presence of caffeine (NCX activity). Meanwhile, the SERCA function could be deconvolved from the decay time constant of the electrically evoked Ca^{2+} transients (NCX + SERCA) with the NCX activity as a fixed input. While for NCX, CytoD could also rescue the DIV0 situation (see figure 3.20C), for SERCA the situation appeared to be more complex (figure 3.20D) since CytoD even exaggerated the culture effects seen in the absence of the supplement.

3.2.6 The optimized concentration of CytoD preserved the T-tubule membrane system in culture

The reduced fractional Ca^{2+} release described above could be due either to a decreased Ca^{2+} influx, or to an uncoupling of the LTCC/T-tubule from the RyR. To investigate that I asked myself whether the integrity of the T-tubular membrane system was lost in the absence of CytoD and whether the supplement was able to rescue that.

As previously reported¹⁵⁸, culture of adult rat ventricular myocytes was accompanied by a significant loss of T-tubular membrane. I also observed such a phenomenon (see also figure 3.16C). While very high concentration of CytoD (40 μM) resulted in an unphysiological remodeling of the T-tubules (“T-tubule crowding”, see figure 3.16C), the effects of the optimized CytoD concentration on the T-tubule are summarized in figure 3.21.

The 3D-reconstruction (figure 3.21A) as well as the quantitative analysis of the power spectra of the di-8-ANEPPS fluorescence (see figure 3.21B) indicated that indeed 0.5 μM CytoD was able to largely prevent loss of T-tubular structures (see figure 3.21C for statistics) while simultaneously

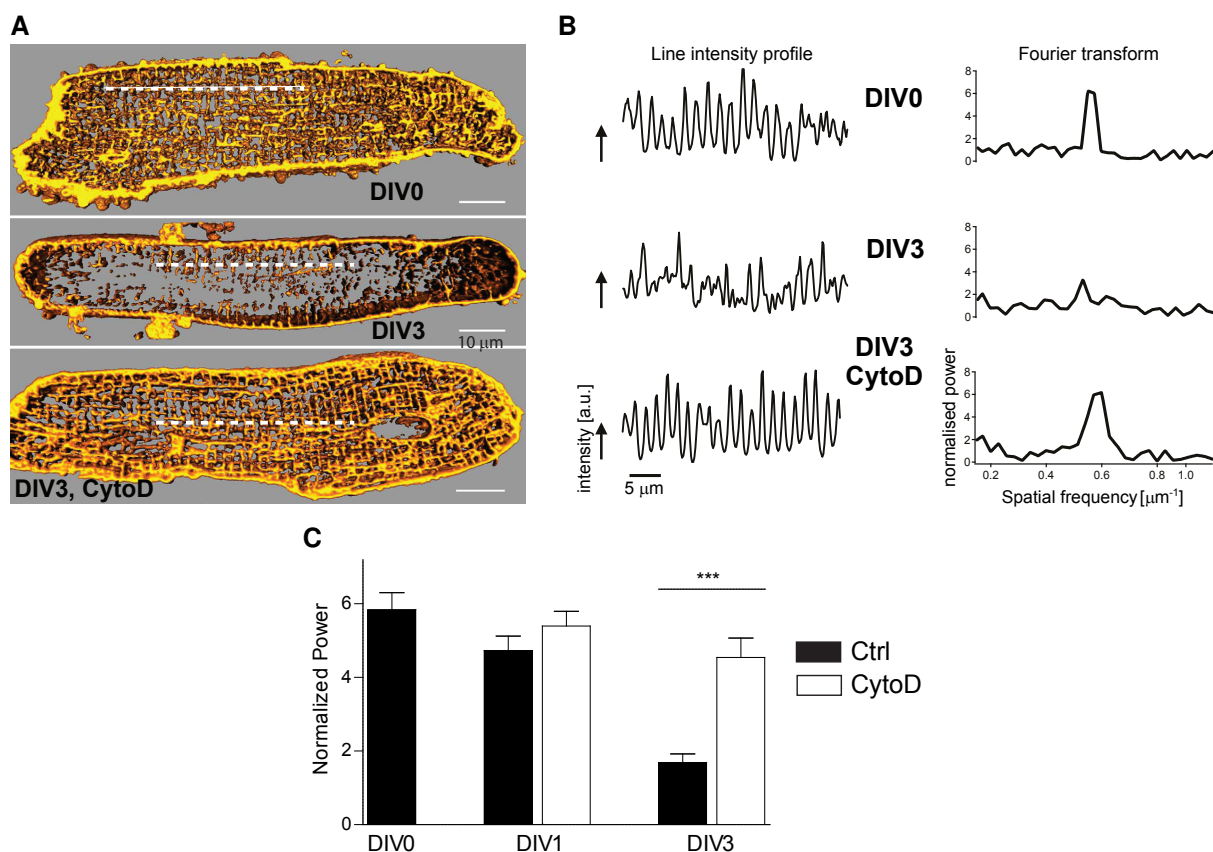


Figure 3.21: Effects of the optimized CytoD concentration on T-tubule remodeling. **A**, representative T-tubular structure in the absence/presences of 0.5 μM CytoD at DIV0 and DIV3. **B**, fluorescence profiles along the dashed lines indicated in **A** and their normalized power spectra. **C**, statistics of the maxima of the normalized power spectra (from 1.0 ~ 2.5 μm) from rat ventricular myocytes at DIV0 and DIV3, with or without 0.5 μM CytoD.

maintaining the T-tubular arrangement (see figure 3.21A). It should be noted that at this optimized concentration, CytoD did not induce T-tubular crowding.

3.2.7 CytoD prevented actin filaments reorganization during culture

As discussed above, reports about the application of CytoD illustrated contradicting results on the actin cytoskeleton, ranging from actin disruption³⁵ to actin stabilization¹¹⁹. Leach et al. reported that CytoD might have an actin stabilizing effect, but they have used very high concentration that in my hand resulted in T-tubular crowding (see figure 3.16C). After finding that 0.5 μM CytoD displayed a preserving effect on the T-tubules during short term culture (figure 3.21), I attempted to characterize the actin cytoskeleton during culture in the absence and presence of CytoD (see figure 3.22).

For this adult rat ventricular myocytes were cultured for the indicated time under the given conditions, chemically fixed and the actin cytoskeleton was stained with phalloidin (shown in red,

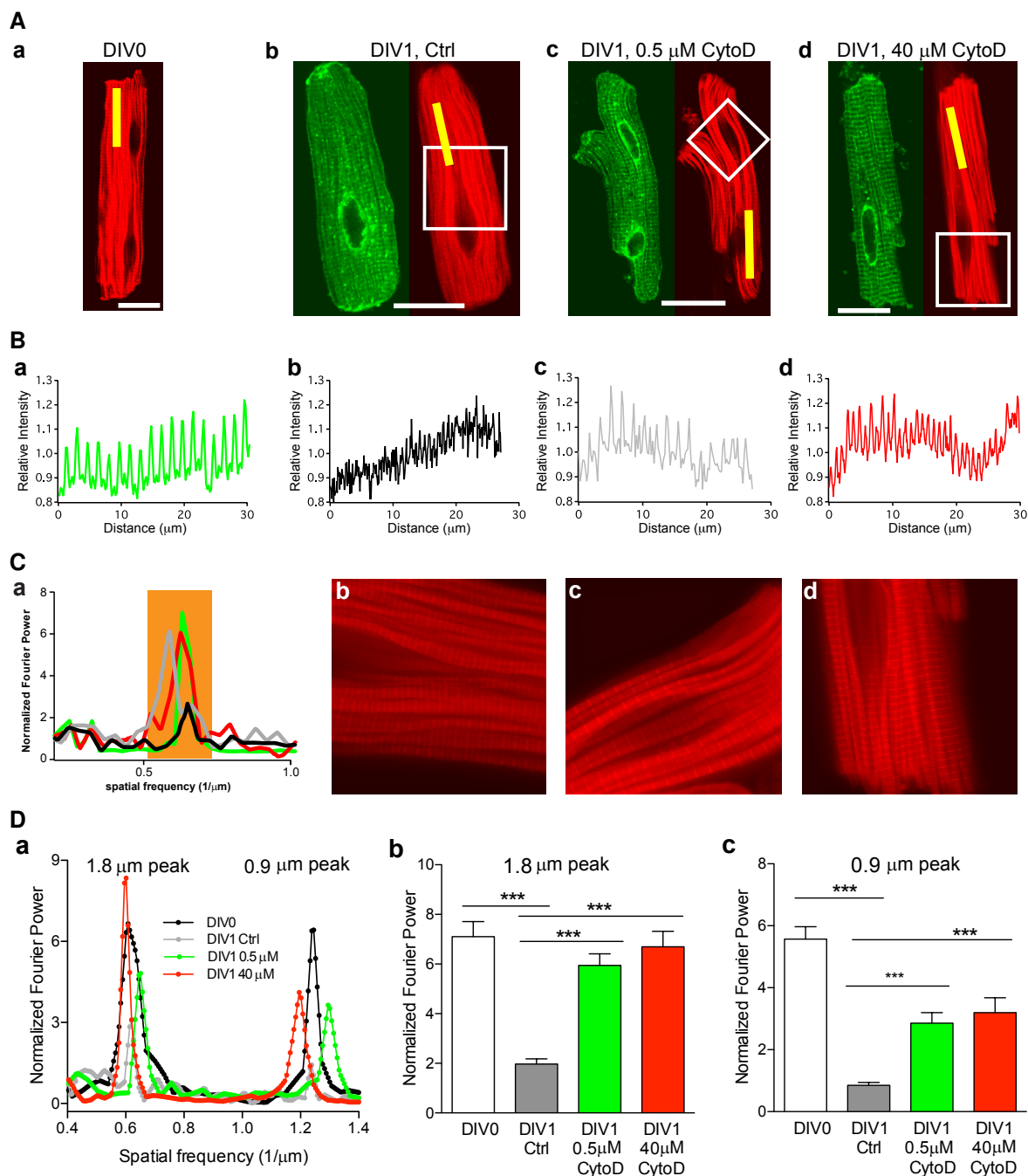


Figure 3.22: The effects of CytoD on cardiac cytoskeleton. **A**, representative rat cardiomyocytes expressing GPI-YFP (membrane) and stained with phalloidin-ATTO-647N (binds F-actin) fixed at DIV0 (Aa) or DIV1. Scale bar, 20 μm . The yellow bars indicate 2 μm wide stripes whose intensity profiles are plotted below the corresponding images in **B**, and the corresponding frequency domains of fast Fourier transform are plotted in **C**a in the same colors. The subsections indicated by the white rectangles in **A** were rescanned in STED imaging mode and displayed in **C**b, **C**c and **C**d, respectively. **D**, Fourier power analysis of Z-line and M-line staining. Panel a shows representative power spectra of F-actin from cells with different CytoD treatments at DIV0 and DIV1; statistics of power peaks at 1.8 μm and 0.9 μm are plotted in **b** and **c**, respectively. Experiments were performed by Dr. Sandra Ruppenthal, and the microscopic scanning by Dr. Christian Schumann and Dr. Lars Kaestner.

figure 3.22) †. To simultaneously confirm integrity of the cell and visualize the T-tubular membrane system, the cells were transduced with an adenovirus coding for a YFP targeted to the plasma membrane (GPI-YFP)⁷⁷.

Figure 3.22Aa and 3.22Ba depict actin arrangement and fluorescence distribution in a DIV0 cell, respectively. Its power spectrum (displayed in figure 3.22Ca, green trace) depicted the expected power peak at around the sarcomeric frequency. In the absence of CytoD the cytoskeleton had undergone remodeling as early as DIV1 (see figure 3.22Ab, 3.22Bb, 3.22Cb and black trace in 3.22Ba). Interestingly, this remodeling was prevented by both, our optimized CytoD concentration (see figure 3.22Ac, 3.22Bc, 3.22Cc and grey trace in 3.22Ba) and the concentration used by Leach et al. (see figure 3.22Ad, 3.22Bd, 3.22Cd and red trace in 3.22Ba).

When I analyzed the power spectra of the phalloidin staining over a wider range of spatial frequencies as depicted in figure 3.22D, I found a second complex of peaks at 0.9 μm that roughly doubles the sarcomeric frequency (right peaks at figure 3.22Da). I attributed this distance (around 0.9 μm) to the distance between the Z-line and the M-line which is in the middle of the A band of a sarcomere and represents interconnections between the thick filaments (myosin) and the extrasarcomeric actin cytoskeleton. Interestingly, the power of this frequency range also showed a massive drop as early as DIV1 in the absence of CytoD and underwent only a partial recovery to around 50% with both CytoD concentrations (0.5 and 40 μM) as a medium supplement (see figure 3.22Dc).

3.2.8 Effects of CytoD on subcellular properties of Ca^{2+} release

So far all data, the structural data (T-tubule and actin staining) and functional data (Ca^{2+} handling and cell contraction), were suggesting that the optimized concentration of CytoD preserved cardiomyocytes during in vitro culture up to 3 days. Since cardiac EC-coupling relies on a simultaneous release of Ca^{2+} throughout the cell and CytoD did preserve the subcellular structure of the cells, I wondered whether the optimized concentration of CytoD was able to maintain a synchronous Ca^{2+} release. For this, I employed fast (1 kHz) line scanning while simultaneously electrically stimulating Fluo-4/AM loaded ventricular myocytes. To quantify and characterize the subcellular properties of the disrupted Ca^{2+} synchrony, I used the so-called “dyssynchrony index” as described elsewhere¹²³.

The Ca^{2+} release dyssynchrony index was defined as the standard deviation of the time needed for each measured subcellular volume (pixel) to reach half-maximum amplitude (figure

†Experiments were performed by Dr. Sandra Ruppenthal, and the microscopic scanning by Dr. Christian Schumann and Dr. Lars Kaestner.

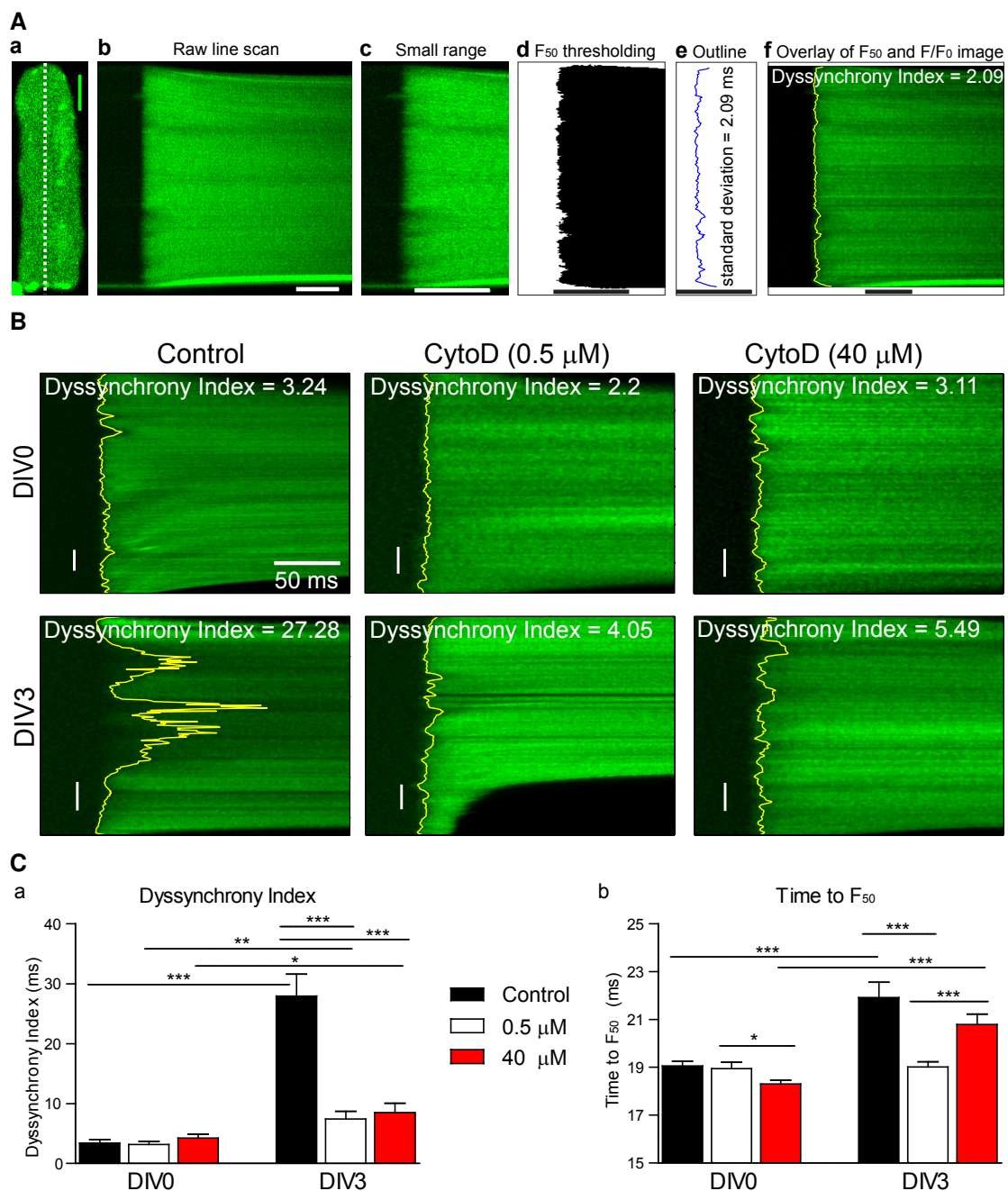


Figure 3.23: CytoD effects on subcellular Ca^{2+} release. Rat ventricular myocytes loaded with Fluo-4 were scanned in line-scan mode on a confocal microscope. **A**, illustration of sample line scan and its analysis. Panel a depicts a fresh rat ventricular myocyte with a dashed line indicating the position of the scanning line. Scale bar, 15 μm . b, confocal line scan data from the cell shown in a. c, enlarged line-scan image. d, thresholding with half-maximal fluorescence (F_{50}). e, outline of detected F_{50} profile and the final calculated dyssynchrony index. f, overlay of the F profile with F/F_0 image. Scale bar in b, c, d, e and f: 50 ms. **B**, line-scan samples from cells treated with the indicated concentrations of CytoD from DIV0 and DIV3. The yellow lines indicate the outline of F_{50} profiles. Scale bar, 15 μm . **C**, statistics of the dyssynchrony index of the Ca^{2+} release (panel a) and the time to F_{50} of the Ca^{2+} transient (panel b) for the ventricular myocytes with different treatments of CytoD from DIV0 and DIV3.

3.23A). While figure 3.23A describes the principle steps to obtain the dyssynchrony index, figure 3.23B summarizes typical line-scan data recorded at the given DIV under the indicated conditions. In the absence of CytoD in the culture medium (left most column of figure 3.23B) the substantial increase in asynchronous Ca^{2+} release was apparent, a finding that is quantified by the increase in the dyssynchrony index (here from 3.24 to 27.28 ms). The statistics from a larger population of cells (figure 3.23Ca, black bars) supported this notion. Interestingly, both CytoD concentrations (0.5 and 40 μM) appeared to suppress this massive increase in the dyssynchrony index (see figure 3.23B, middle and right columns and figure 3.23Ca, white and red bars). Nevertheless, it has to be noted here, that neither of the CytoD concentrations could diminish this increase completely, a small, but significant increase in the dyssynchrony index was left (figure 3.23Ca, white and red bars). While the dyssynchrony index characterizes the spatial homogeneity of Ca^{2+} release, I also analyzed the resulting line-scan transients with respect to their mean steepness of Ca^{2+} increase (figure 3.23Cb). For this I calculated the mean time to 50% of the amplitude for each subcellular volume (pixel) of the line-scan image. Interestingly, here I found an immediate effect of the 40 μM CytoD already at DIV0, it slightly but significantly shortened that time, however at DIV3, both control and 40 μM CytoD conditions displayed a significant increase in the time to 50% value while only the optimized CytoD concentration (0.5 μM) depicted a conservation of this value.

3.2.9 Final remarks for this section

These data again indicated and supported our notion that 0.5 μM CytoD as a culture supplement was indeed an optimized concentration to diminish culture dependent remodeling processes both on the morphological and on the functional level.

3.3 Computer-aided CICR analysis

3.3.1 Theoretical analysis of CICR signal

3.3.1.1 Components of measured signal

As illustrated in section 3.2.8, line-scan images could characterize the dyssynchrony of Ca^{2+} release. However, a single line along the longitudinal axis could not be regarded as representative. I thus used fast (≥ 100 Hz) 2D scanning of the entire cell to get a more representative recording of CICR. However, the huge amount of noise that accompanied the real “signal” prevented us from further analysis of subcellular Ca^{2+} signaling. In principle the measured fluorescence signal

was a convolution of the real Ca^{2+} signal and random noise generated by the confocal set-up. Processes that contributed to this noise level were: laser, i.e. excitation noise, photon statistical noise and detection noise (like PMT).

There were several approaches to overcome this situation. The easiest method was to smooth the raw signals in the temporal or spatial dimensions. This could significantly alter the properties of the underlying Ca^{2+} signal. A better approach would be to apply specialized filter systems, e.g. those that rely on evaluating the properties of the noise in the frequency domain (by Fourier transform) and then attempting to eliminate the noise. I tested those filters and found that they either resulted in signals with diminished noise levels but altered Ca^{2+} signals or in fluorescence data with largely preserved Ca^{2+} signals but still compromised by high levels of noise. I thus thought about another approach by assuming that measured fluorescence was composed of the true, noise-free signal and the recording noise. This situation is illustrated in figure 3.24.

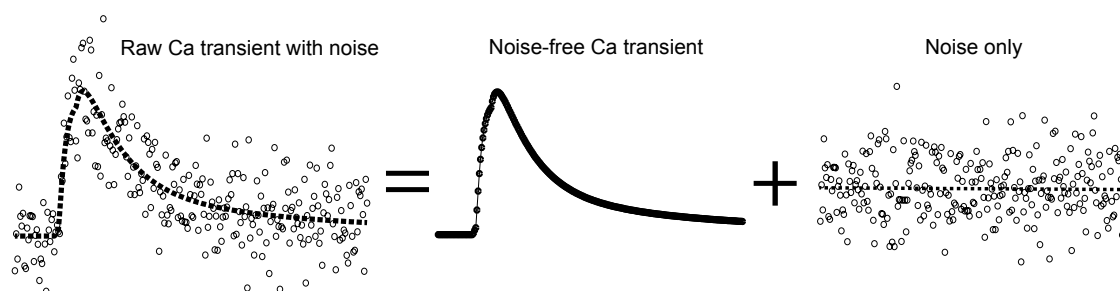


Figure 3.24: Illustration of the principal strategy of model-based fitting.

If I could construct a method to separate or deconvolve these signals, it would be possible to remove noise and analyze subcellular Ca^{2+} signaling simultaneously. I tried to come up with an easy and basic mathematical description of the Ca^{2+} signals in order to use the measured data and fit such a simple model to the data. The result would be an analytical description of the data that would be inherently noise free. I envisaged that such an approach should be applied to each individual volume element of our recording (the pixels of the image over time), and thus would allow an analytical 2D-description of the Ca^{2+} transient obtained by fitting the recorded data to the descriptive equation. I called our approach “pixel-wise fitting” that is described in the following.

3.3.1.2 Global Ca^{2+} transient

The common way to calculate an apparent uncalibrated global Ca^{2+} transient from measured image-based data is,

$$[Ca]_{app}(t) = \sum_0^{x_{dim}} \sum_0^{y_{dim}} I_{pixel}(x, y, t) \quad (3.4)$$

where I_{pixel} is the intensity of specific single pixel.

3.3.1.3 Description of local Ca^{2+} transients

I initially have to stress the point that in the following I did not attempt to compile a comprehensive mechanistic model of subcellular Ca^{2+} signals. In contrast, I tried to describe local Ca^{2+} signals in a very simplistic way. The discussion section will discuss limitations of such an approach. For my simplified view of the Ca^{2+} signal I assumed the cytosol to be a pool, that is filled via a process (here a combination of Ca^{2+} influx and Ca^{2+} release, see figure 3.25) and emptied by a removal process (here either a single or a combination of two processes). In adult rat cardiomyocytes, Ca^{2+} influx only contributes 7% to the Ca^{2+} signals, while the the majority of the transient is generated by Ca^{2+} release from SR¹⁴. It appeared thus feasible to assume a single release process either described by a mono exponential increase (left assumption for Ca^{2+} release in figure 3.25) or by a pulsatile Ca^{2+} release process that could be described by a Gaussian function (right assumption for Ca^{2+} release in figure 3.25). In rat ventricular myocytes more than 95% of the removal of Ca^{2+} from the cytosol is performed by the SERCA pump and the NCX activity. The Ca^{2+} removal process could thus be described by a mono- or bi-exponential decay.

After those initial thoughts, three model descriptions appeared worthwhile implementing into programs and testing on “real data”. Fitting of real data to an equation is generally more robust if the least parameters have to be fitted, especially when considering that I faced a limited amount of data points for fitting. Thus, the first assumption to be implemented was a convolution of Gaussian function for release and mono exponential removal, that I called GauConvExp. I compared this

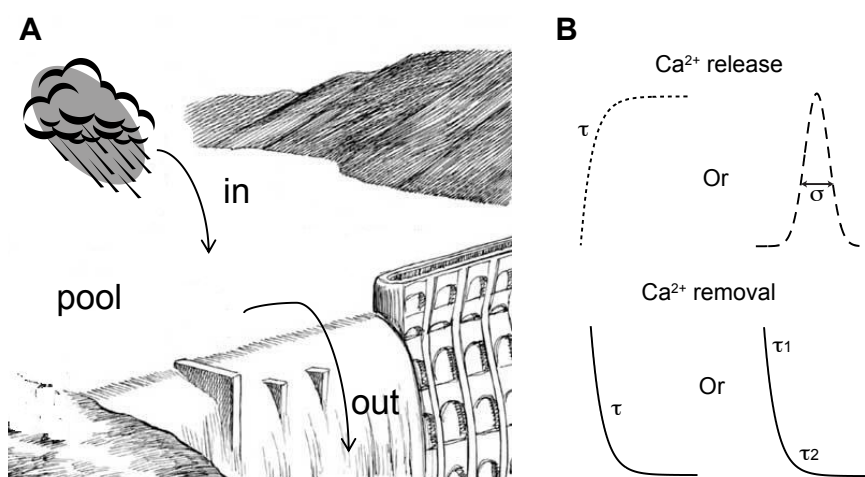


Figure 3.25: Local Ca^{2+} transient events. **A** shows the water level of the pool determined by a water flowing-in process from the raining and a water flowing-out process, water overflowing over the dam. **B** shows the two example functions that were used: Gaussian function or exponential growth function to describe the Ca^{2+} release process (top panel), and single or double exponential decay function to describe the Ca^{2+} removal process (bottom panel). The original cartoon was from Lake Hodges Scientific Research Center.

one with a mono exponential release phase convolved with a mono exponential removal phase, referred to as ExpConvExp. Finally I implemented a double exponential removal period, called ExpConvdbExp. Each of these approaches is briefly described in the following.

3.3.1.3.1 Fitting with GauConvExp For the local Ca^{2+} influx and efflux, I assumed

$$V_{ca_{in}} = Gau(t) = \frac{1}{\sqrt{2\pi}\sigma} e^{-\frac{(t-\mu)^2}{2\sigma^2}} \quad (3.5)$$

$$V_{ca_{out}} = Exp(t) = e^{-\frac{t}{\tau}} \quad (3.6)$$

where σ reflects the duration of Ca^{2+} influx, and μ the time point of the maximum speed of Ca^{2+} increase.

The local Ca^{2+} efflux process depended on the Ca^{2+} level and the velocity of Ca^{2+} removal, so the entire local Ca^{2+} transient could be described by the convolution of a Gaussian function with an exponential decay function,

$$\begin{aligned} F(t) &= Gau \otimes Exp \\ &= \frac{1}{\sqrt{2\pi}\sigma} \int_{-\infty}^t e^{-\frac{(t-t')^2}{2\sigma^2}} e^{-\frac{t-t'}{\tau}} dt' \\ &= \frac{1}{\sqrt{2\pi}\sigma} \int_{-\infty}^0 e^{-\frac{(t_0-t-t')^2}{2\sigma^2}} e^{-\frac{t'}{\tau}} dt' \end{aligned} \quad (3.7)$$

Since there is no mathematical solution for equation 3.7, an equation transformation was performed,

$$F(t) = \frac{1}{2} e^{\frac{\sigma^2 + 2\tau(t_0-t)}{2\tau^2}} \left(1 - \frac{\sigma^2 + \tau(t_0-t)}{|\sigma^2 + \tau(t_0-t)|} * \text{erf}\left(\frac{|\sigma^2 + \tau(t_0-t)|}{\sqrt{2}\sigma\tau}\right) \right) \quad (3.8)$$

such that equation 3.7 could be numerically solved with an error function,

$$\text{erf}(x) = \frac{2}{\sqrt{\pi}} \int_0^x e^{-t^2} dt \quad (3.9)$$

With the convoluted function (equation 3.8) to describe the Ca^{2+} transient, the final fluorescence intensity of a single pixel could be fitted like,

$$I(t) = \frac{Amp}{2} e^{\frac{\sigma^2 + 2\tau(t_0-t)}{2\tau^2}} \left(1 - \frac{\sigma^2 + \tau(t_0-t)}{|\sigma^2 + \tau(t_0-t)|} * \text{erf}\left(\frac{|\sigma^2 + \tau(t_0-t)|}{\sqrt{2}\sigma\tau}\right) \right) + Bgr \quad (3.10)$$

Here, $I(t)$ represents the fluorescence intensity from single pixel (or Ca^{2+} concentration) over time, the Amp is the amplitude of the local Ca^{2+} transient, and Bgr is the baseline signal.

3.3.1.3.2 Fitting with ExpConvExp Compared with the GauConvExp function, in the ExpConvExp function, the Gaussian function (equation 3.5) was replaced with an exponential function,

$$V_{ca_{in}} = \begin{cases} 1 - e^{-\frac{(t-\mu)}{\tau_{in}}}, & \text{if } t \geq \mu \\ 0, & \text{if } t < \mu \end{cases} \quad (3.11)$$

$$V_{ca_{out}} = \begin{cases} e^{-\frac{(t-\mu)}{\tau_{out}}}, & \text{if } t \geq \mu \\ 0, & \text{if } t < \mu \end{cases} \quad (3.12)$$

where μ is the onset time point for Ca^{2+} increase.

So the final Ca^{2+} transient simulation function (ExpConvExp) read as,

$$I(t) = \begin{cases} A * (1 - e^{-\frac{(t-\mu)}{\tau_{in}}}) * e^{-\frac{(t-\mu)}{\tau_{out}}} + Bgr, & \text{if } t \geq \mu \\ Bgr, & \text{if } t < \mu \end{cases} \quad (3.13)$$

where τ_{in} reflects the time constant of Ca^{2+} increase, τ_{out} the Ca^{2+} removal, μ the time point of initial Ca^{2+} release, A the virtual amplitude of the transient, and Bgr the baseline signal.

3.3.1.3.3 Fitting with ExpConvdbExp Compared with the ExpConvExp function, in the ExpConvdbExp function the single Ca^{2+} removal process was replaced by a double exponential function,

$$V_{ca_{out}} = \begin{cases} A_1 * e^{-\frac{(t-\mu)}{\tau_{out1}}} + A_2 * e^{-\frac{(t-\mu)}{\tau_{out2}}}, & \text{if } t \geq \mu \\ 0, & \text{if } t < \mu \end{cases} \quad (3.14)$$

where A_1 and A_2 are the amplitudes for the two exponential processes.

And the final ExpConvdbExp fitting function was,

$$I(t) = \begin{cases} (1 - e^{-\frac{(t-\mu)}{\tau_{in}}}) * (A_1 * e^{-\frac{(t-\mu)}{\tau_{out1}}} + A_2 * e^{-\frac{(t-\mu)}{\tau_{out2}}}) + Bgr, & \text{if } t \geq \mu \\ Bgr, & \text{if } t < \mu \end{cases} \quad (3.15)$$

where τ_{in} is the time constant of Ca^{2+} increase, τ_{out1} and τ_{out2} the two Ca^{2+} removal processes, μ the onset time point of the Ca^{2+} transient, A_1 and A_2 the virtual amplitudes of the two extrusion processes, and Bgr the baseline signal.

3.3.2 Fitting Strategies

The entire fitting procedure was performed based on the Nelder-Mead Simplex Optimization algorithm¹¹⁶. Since for any fitting procedure the starting values can be of prime importance for a sensible outcome, I decided to perform the fitting in two steps. Step one involved a global fitting (pre-processing phase in figure 3.26), that is, I averaged the fluorescence data of the entire cell, treating it as a single pixel and fitting the equation to the rather noise-free global data. In a second step, I used the resulting parameters as starting values for the pixel-wise fitting that followed (pixel-wise fitting phase in figure 3.26)¹³³. Here the fluorescence over time data for every single pixel in the image were used for the local fitting process, such that an optimized global fitting was expected based on the greedy algorithm⁴⁷.

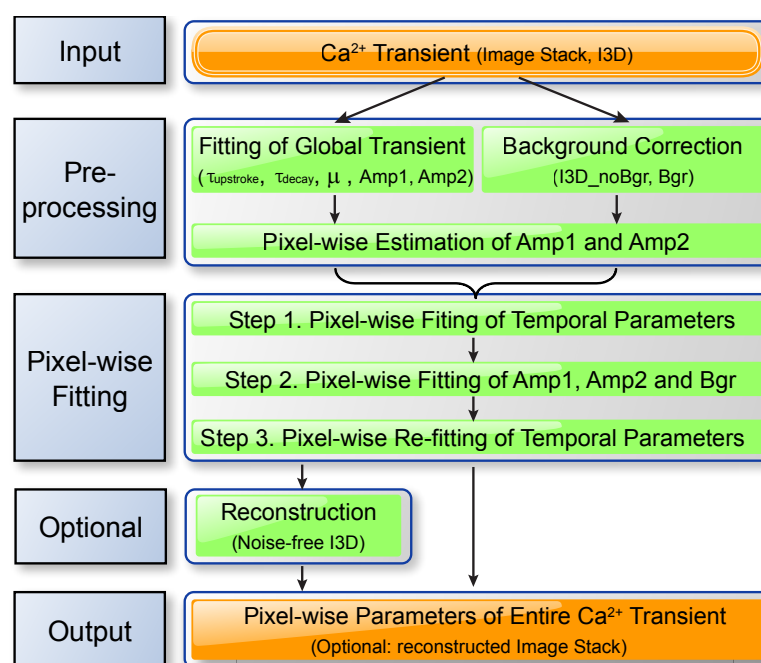


Figure 3.26: Algorithm work-flow chart for ExpConvdbExp function. I3D, 3-dimensional image stack; τ_{decay} for τ_{decay_1} and τ_{decay_2} ; $\tau_{upstroke}$, τ for the Ca^{2+} release; μ , the onset time point of Ca^{2+} release; I3D_noBgr, I3D without background; Bgr, background.

The final equations (equation 3.10, 3.13 and 3.15) indicate that at least five parameters needed to be fitted. In the ExpConvdbExp function I even have to add two more for the second decay component. While global fitting worked fine for all equations listed, pixel-wise fitting resulted in problematic data since a number of pixels gave “unreasonable” fitting results, that were obviously off-scale. The principle reason for this might be found in the fact that fitting with such a high number of independent variables (seven in the worse scenario) might give optimal fits from the mathematical point of view but may involve using parameter values that simply is of “no physiological sense”. In the images such “problem pixels” were visible as either black or white dots

with unreasonable high or low fluorescence values. Although additional spatial smoothing could reduce such pixels I thought of an alternative approach: a step-by-step fitting routine.

For this I grouped all fitting parameters into two groups: time-related and intensity-related parameters. Before the pixel-wise fitting, I estimated the amplitude by finding out the maximum and the minimum value of every single measured pixel Ca^{2+} transient. In ExpConvdbExp, the amplitude was divided into two parts according to the two global amplitudes. The pixel baselines were calculated from the time period just before the Ca^{2+} release. During the first step of fitting, the temporal parameters τ_{in} , τ_{out} and μ , (as well as the second τ_{out} in ExpConvdbExp) were fitted with the estimated amplitudes and baselines for each pixel Ca^{2+} transient. In step 2, the amplitude and baseline values were fitted based on the optimized temporal parameters from step 1. Finally, all the parameters were fitted again for every single pixel Ca^{2+} transient with the fitted temporal parameters from step 1 and intensity-related parameters from step 2 as the starting values.

3.3.3 High speed 2D imaging of cardiac Ca^{2+} imaging

For data acquisition, I used a PMT-based Leica TCS SP5 high-speed confocal microscope. This was a point-scanner with a resonating galvo mirror capable of 8000 lines/s. Since the image size, or precisely the number of lines, was the major determinant of image acquisition speed, I picked an image size of 512×80 pixels with a pixel size of $0.283 \times 0.283 \mu\text{m}$, which was at the theoretically optical resolution limit of the microscope. This image size perfectly matched the brick-like shape of rat ventricular myocytes. Using those dimensions image recording rate was 146 frames/s that was sufficient to temporally and spatially resolve cardiac EC-coupling (see figure 3.27).

With this high speed/high resolution scanning mode, the calculated dwell time for every pixel was $0.166 \mu\text{s}$. By considering the efficiency of PMT detectors¹⁶⁸ (which is usually below 30%),

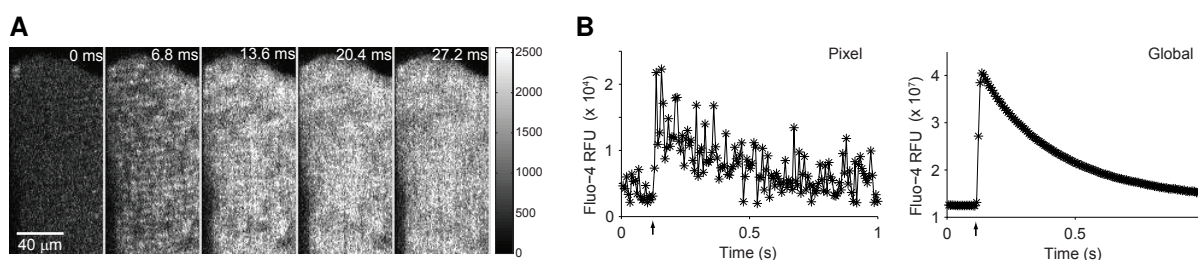


Figure 3.27: Raw data example from high resolution imaging on confocal microscope. **A**, 2D confocal microscopic scanning of Ca^{2+} transient at upstroke phase (146 Hz). **B**, single pixel and global Ca^{2+} transients. Arrows indicate the time point of electrical field stimulation. The ventricular myocyte was from a Wistar rat, measured in the presence of 1.8 mM extracellular Ca^{2+} .

the really effective integration time for every pixel can be calculated like,

$$\begin{aligned}
 t_{\text{dwell}} &= \frac{1}{x \times y \times \text{speed}} \times E \\
 &= \frac{1}{512 \times 80 \times 146} \times 30\% \\
 &= 5.02 \times 10^{-8} \text{ (s/pixel)}
 \end{aligned}
 \tag{3.16}$$

With this limited integration time, the pixel signal was severely corrupted by Gaussian noise and Poissonian noise¹²⁵ (see also figure 3.27B), even when the highest intensity of the laser that the cell could tolerate was used. The signal coefficient of variation (CV) at the basal Ca²⁺ concentration was 39.45% ~ 43.28% at the Ca²⁺ baseline, and the typical signal-to-noise ratio was 2.36.

3.3.4 Pixel-wise fitting

3.3.4.1 Comparison of different mathematical functions

As described above, I envisaged three different approaches to describe global and local Ca²⁺ signaling. Here I compared all three side-by-side in order to identify the optimal approach. For this, local Ca²⁺ transients were fitted with all three functions (figure 3.28A), then the global Ca²⁺ transients were reconstructed (figure 3.28B) with locally fitted parameters.

All functions belong to the “family” of parallel models, implying that Ca²⁺ removal process occurs throughout the entire transient starting from the beginning of the Ca²⁺ release, while for other models, referred to as sequential models^{115,245}, Ca²⁺ removal processes only kick-in at the peak of the transient. From the results in figure 3.28, it can be concluded that despite an indistinguishably different residual noise levels for all three approaches on the local level, they display characteristic differences on the global level. Both functions, ExpConvExp and GauConvExp show imperfect fitting at the onset and during later recovery periods of the Ca²⁺ transients (indicated by arrows) while the ExpConvdbExp, using a mono exponential description for the onset and a double exponential description of the recovery of the Ca²⁺ transient, did not depict significant deviations between the measured and the fitted time course (leftmost panel in figure 3.28B).

From the comparison of the three different fitting approaches it was apparent that the ExpConvdbExp was best able to describe the time course of Ca²⁺ transients. Thus for the following I decided to employ the ExpConvdbExp function.

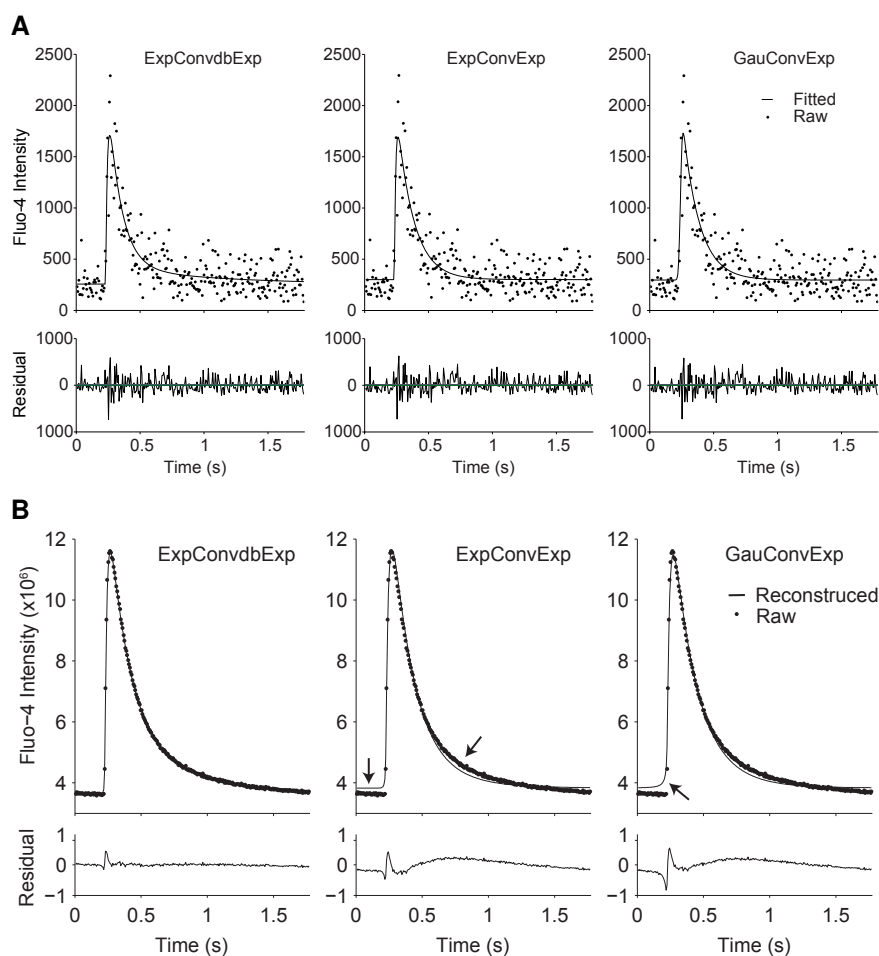


Figure 3.28: Pixel-wise fitting with different mathematical functions. Same raw data of cardiac Ca^{2+} transient from confocal microscope were pixel-wisely fitted and reconstructed, and representative pixel and global fitting are shown in **A** and **B** respectively. The data was from the same cell as shown in figure 3.33. Arrows indicate the regions with large fitting residuals.

3.3.4.2 Fitting results with ExpConvdbExp function

From the equations used for the ExpConvdbExp fitting several interesting and important physiological parameters could be extracted. They are summarized in figure 3.29. Here, I illustrate the distribution of the Ca^{2+} transient amplitude (figure 3.29A), Ca^{2+} release duration (figure 3.29B) and the averaged decay τ (figure 3.29C). Interestingly, when analyzing the spatial frequency domain of the Ca^{2+} release process (black box in figure 3.29B) a power peak at the sarcomeric frequency of $0.56/\mu\text{m}$ ($1.8 \mu\text{m}$) could be detected (figure 3.29E) indicating the expected regularity of the Ca^{2+} release process.

In model-based fitting, the value R^2 quantifies the goodness of fit. It is a fraction between 0.0 and 1.0 without units. Higher values indicate that the model fits the data better. R^2 is computed from the sum of the squares of the distances of the points from the best-fit curve determined by nonlinear regression. This sum-of-squares value is called SS_{reg} , which is in the units of the Y-axis

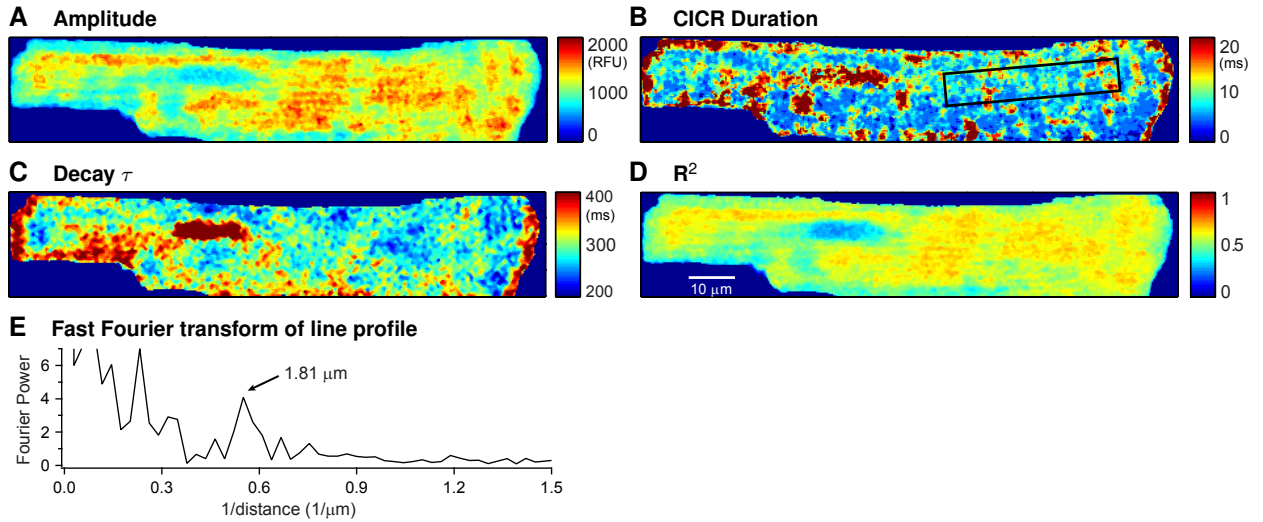


Figure 3.29: Pixel-wise fitting of Ca^{2+} transients. Ca^{2+} transients from all pixels constituting the ventricular myocyte were fitted with function ExpConvdbExp (Equation 3.15). The resultant parameters, including amplitude, CICR duration, decay τ , and the fitting coverage parameter R^2 are shown in panel **A**, **B**, **C** and **D**, respectively. The black box in **B** indicates the ROI whose line profile was transformed with Fast Fourier Transform (FFT) and the trace of frequency domain is shown in panel **E**. The data was from the same cell in figure 3.27. Decay τ is calculated according to formula:

$$\tau = \frac{Amp_1 * \tau_1 + Amp_2 * \tau_2}{Amp_1 + Amp_2}.$$

squared. To turn R^2 into a fraction, the results are normalized to the sum of the square of the distances of the points from a horizontal line through the mean of all Y values. This value is called SS_{tot} . If the curve fits the data well, SS_{reg} will be much smaller than SS_{tot} . Here I called the R^2 as “fitting coverage parameter”, and was calculated as,

$$R^2 = 1.0 - \frac{SS_{reg}}{SS_{tot}} \quad (3.17)$$

When R^2 equals 1.0, all points lie exactly on the curve with no scatter. Otherwise, the fitting can not cover the all the data points, which will results in larger residual. Here the ExpConvdbExp fitting resulted in a median R^2 of $0.60 \sim 0.70$ (see figure 3.29D). Considering that the noise CV was up to 40% (mentioned above), I concluded that the pixel-wise fitting had extracted out almost all the useful information out of the noisy raw Ca^{2+} signals.

3.3.4.3 Pixel-wise reconstruction

With these fitted parameters for all pixel transients, a Ca^{2+} transient for the whole cell was finally reconstructed (see figure 3.28B and 3.30). The reconstructed Ca^{2+} transient (figure 3.30B) reproduced the noisy raw data (figure 3.30A) with highly diminished spatial noise (figure 3.30C, noise from range of for example the noise was reduced from $[-300, 500]$ to $[-100, 150]$ for the first frame

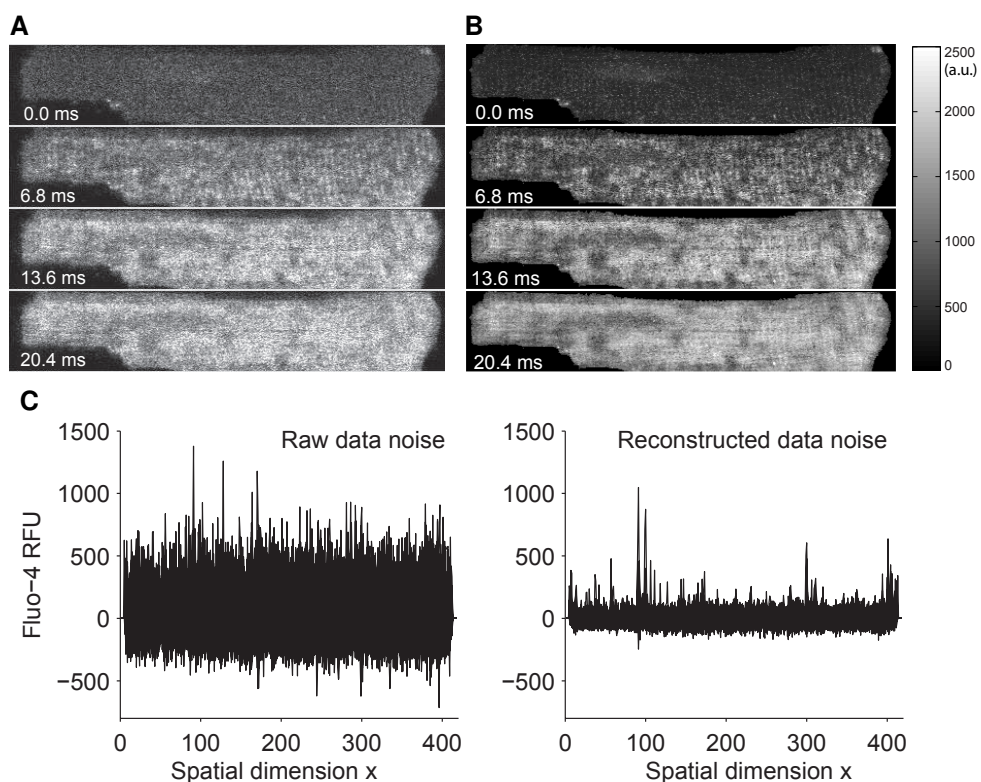


Figure 3.30: Comparison of raw and reconstruction of Ca^{2+} transients. **A**, individual confocal images at the given time points. Rat ventricular myocytes loaded with Fluo-4/AM and subjected to electrical stimulation. **B**, after fitting the data with the ExpConvdbExp function, the Ca^{2+} transient was reconstructed for identical time points as in **A**. **C** shows the noise levels from the raw confocal image (the first frame in panel **A**) and reconstructed image (the first frame in panel **B**). The noise was calculated with the equation: $\text{Noise} = \text{image} - \text{medfilt2}(\text{image})$, where medfilt2 represented a 2-dimensional 3×3 median filter.

shown in figure 3.30A and 3.30B).

Mathematically, the ExpConvdbExp function is continuous. Since all the pixel-wise parameters for the function have been fitted, the Ca^{2+} transient itself is now also temporally continuous. Thus a new Ca^{2+} transient can be reconstructed at any temporal resolution. Such a reconstruction with 3 times higher sampling frequency is shown in figure 3.31. The “interpolated” frames during the Ca^{2+} release phase (from 8.74 ms to 20.4 ms in figure 3.31C) clearly resembled the cell-crossing pattern that was seen in the raw or reconstructed frames.

3.3.4.4 Contraction perturbation

Whereas fitting and reconstruction worked reliably on most cells, with those myocytes that showed severe contraction, the fitting failed for a small portion of pixels (see figure 3.32). The main reason for that was that the volume of observation changed during the Ca^{2+} transient. This could not be compensated easily. One possible way out would have been chemical suppression of contraction

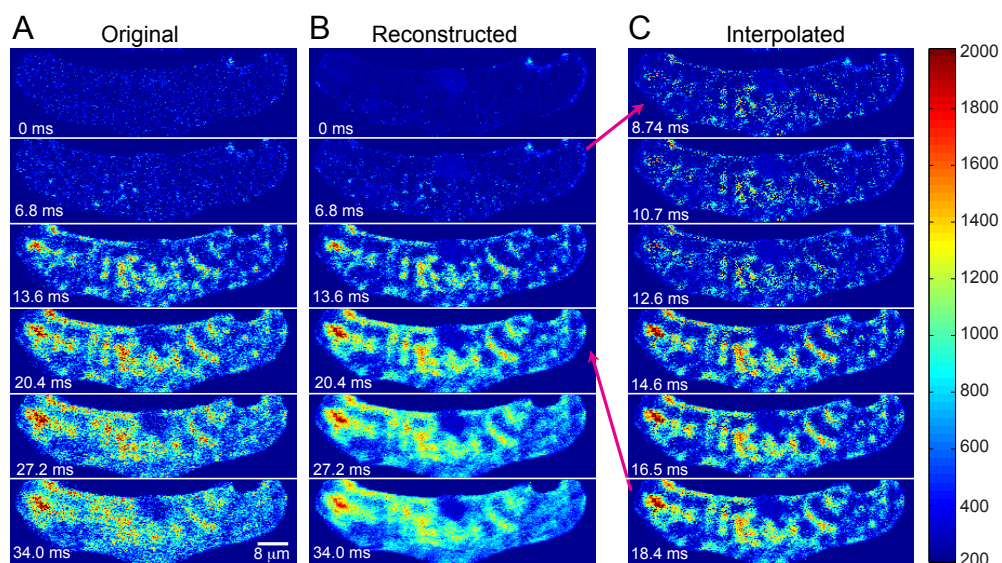


Figure 3.31: Temporally unlimited interpolation of Ca^{2+} transients. **A**, raw Ca^{2+} transient signals during the upstroke phase. **B**, reconstructed Ca^{2+} transient signals corresponding to **A**. **C**, an example of signal interpolation with 3 times higher sampling frequency during the upstroke phase. Arrows show the start and end frames of the interpolation. The cell was isolated from the left atrium of a healthy FVB/N mouse.

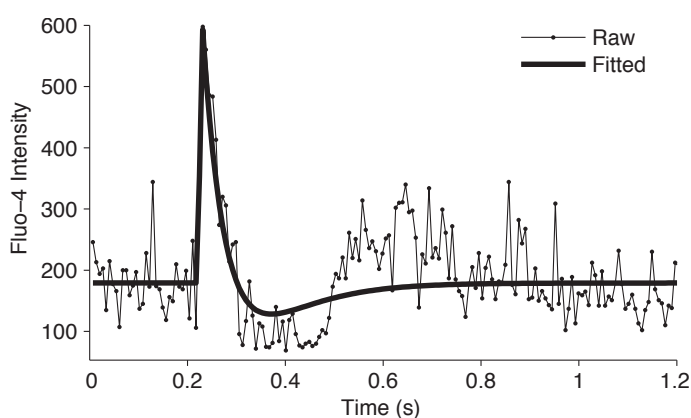


Figure 3.32: Contraction effects on ExpConvdbExp fitting. Shown is a pixel Ca^{2+} transient that was affected with contraction and its fitted signal with ExpConvdbExp function.

by the application of pharmacological agents, such as BDM or blebbistatin²⁰⁵. Since all those agents also altered Ca^{2+} signaling they were not considered further. Therefore cells shown in the following are all cells where contraction artifacts were at their minimum.

3.3.4.5 Reproducibility of pixel-wise fitting

To test the reproducibility of my fitting approach I thought of an experimental approach yielding cellular Ca^{2+} transients with a very high probability of reproducibility: steady state conditions during electrical pacing. Under those conditions, Ca^{2+} transients following consecutive electrical stimulations should yield signals that are superimposable. Figure 3.33 and table 3.2 summarize

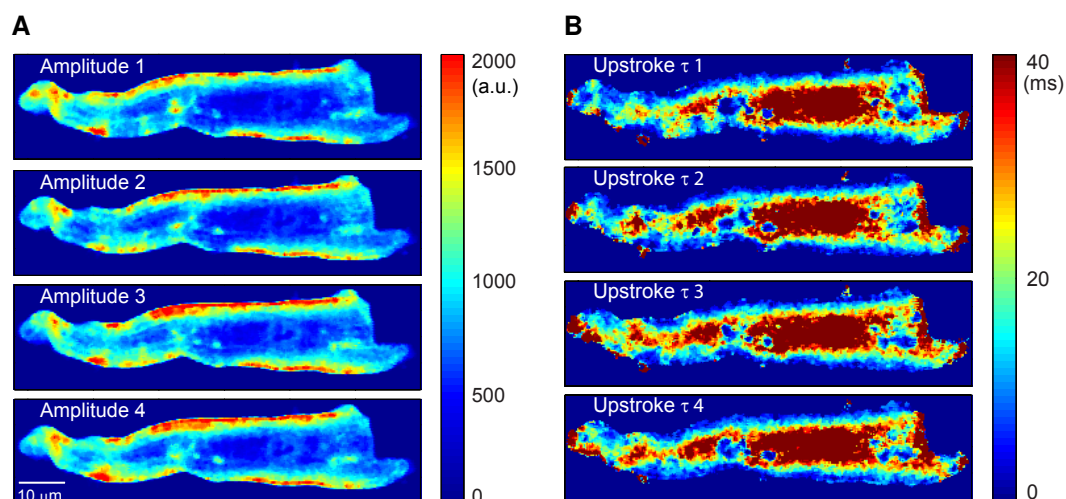


Figure 3.33: Reproducibility of pixel-wise fitting. Four consecutive Ca^{2+} transients of a myocyte from left atrium of RacET mouse were recorded and fitted, and the pixel amplitudes and the time constants of Ca^{2+} release (τ) are shown in **A** and **B** respectively. Extracellular Ca^{2+} : 1.2 mM. Note that all the images were filtered with median filter (3×3) to remove salt and pepper noise generated from fitting errors.

Table 3.2: Reproducibility of pixel-wise fitting

-	$Amplitude_1$	$Amplitude_2$	$Amplitude_3$	$Amplitude_4$
Upstroke τ_1	-	0.9341	0.936	0.9274
Upstroke τ_2	0.8124	-	0.9395	0.9393
Upstroke τ_3	0.8148	0.8164	-	0.942
Upstroke τ_4	0.8213	0.8157	0.8251	-

Note: The cell was the same cell as shown in figure 3.33.

data from a typical cardiac myocyte. In order to provoke subcellular regions with CICR failures I chose atrial myocytes with a rudimentary T-tubular system and a reduced extracellular Ca^{2+} concentration (1.2 mM)^{2,127}. After pacing such a cell for three minutes the resulting Ca^{2+} transients had reached steady state. Under these conditions I performed fitting of four consecutive Ca^{2+} transients as shown in figure 3.33. While panel A depicts the derived amplitude distribution, panel B illustrates the color coded upstroke time constant. Even without any further correlation analysis, it became apparent that the distribution of these two parameters was very comparable amongst these four Ca^{2+} transients.

To quantify the reproducibility in between Ca^{2+} transients I calculated the correlation coefficient²⁰⁸ for the amplitudes and the upstroke time constants and found that both parameters correlated between 81% and 94% (see table 3.2), indicating a very good reproducibility of the fitting algorithm. Such a reliable approach was necessary in order to study changes or failures of CICR in normal and/or diseased cardiac myocytes.

3.3.5 Application of “pixel-wise” fitting in the study of subcellular cardiac Ca^{2+} signaling

Now that I have a method in hand that describes subcellular Ca^{2+} transients well and also allow the deduction of important EC-coupling characteristics such as those describing the release process itself, I thought of testing that approach on two different experimental systems: i) healthy and diseased atrial myocytes from a mouse model of atrial fibrillation (AF) and, ii) a system displaying cellular Ca^{2+} alternans, an important substrate for ventricular arrhythmia¹¹⁸.

3.3.5.1 Atrial myocyte EC-coupling

As depicted in chapter 1 and reported elsewhere^{21,23,92}, atrial myocytes of various species display a rather complex subcellular EC-coupling. While human and cat atrial myocytes only possess a rudimentary (if any) T-tubular system, our group has shown recently that mouse atrial myocytes from left atria have a rather well developed system of membrane invaginations. In a mouse model of atrial fibrillation (the RacET mouse that expresses a constitutively active mutant of Rac1²⁰⁶), we could recently describe a loss of T-tubules during the development of AF.

I thought of studying the relationship between cellular membrane topology and subcellular Ca^{2+} signaling in greater detail by means of “pixel-wise” fitting. For this I performed fast confocal recording of subcellular Ca^{2+} signals as well as high-resolution reconstruction of the plasma membrane in the very same cells and applied my fitting approach. Such an entire analysis flow is illustrated in figure 3.34.

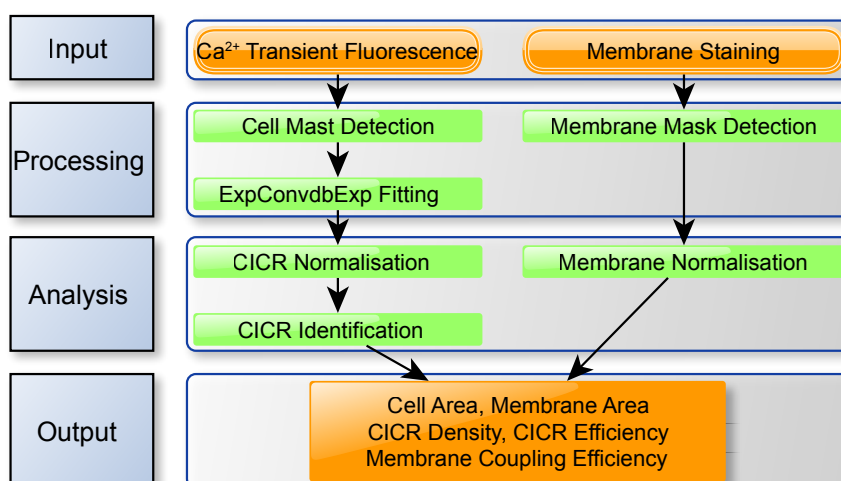


Figure 3.34: Flow chart of membrane-CICR coupling analysis.

3.3.5.2 Reconstruction of the plasma membrane

The raw readout of the membrane recording varied from experiment to experiment, and even from cell to cell in the same experiment. In order to quantify the fraction of membrane that contributed to the Ca^{2+} release, the membrane staining was normalized before calculating the EC-coupling efficiency. For this, all the pixels that constituted the cell membrane were analyzed by their cumulative histogram, the intensity values at 5% and 80% were set as the “low” and “high” threshold in the normalization. Such a membrane normalization is shown in figure 3.35. With this normalization, the variations from inhomogeneous dye loading could be amended and the real membrane distribution could be restored.

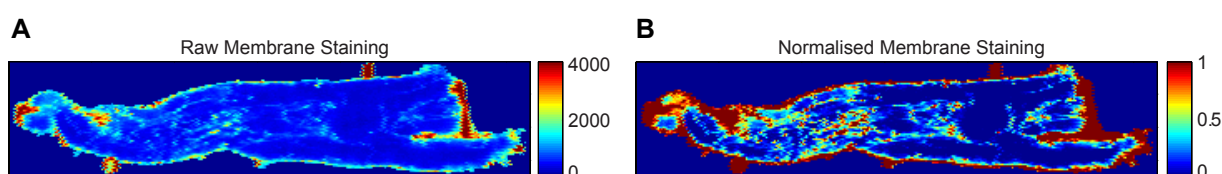


Figure 3.35: Normalization of membrane staining. **A**, raw membrane staining. **B**, normalized membrane staining.

3.3.5.3 Identification of EC-coupling sites

EC-coupling is manifested by the $1/\tau$ value of the upstroke that is in the real temporal unit (1/ms), which makes it elusive to compare one cell with another and difficult to calculate the fractional membrane that contributes to the Ca^{2+} release. To identify the EC-coupling sites, I used an algorithm “H-maxima transformation”²⁰⁹ to identify the EC-coupling sites, in which regional maxima are calculated with a constant intensity value (H-value), and their external boundary pixels all have a lower value¹⁹⁹. For both of these reasons, a normalized $1/\tau$ is needed.

To calculate the normalized $1/\tau$, all the pixels that constituted the cell were analyzed by their histogram. The fastest pixels was set to 100% and the maximal pixel counting was set to 50% in the assumption that this histogram would follow a Gaussian distribution if it is a healthy cell. Such a normalization is shown in figure 3.36A. With the normalized $1/\tau$, a H-value of 15% turned out

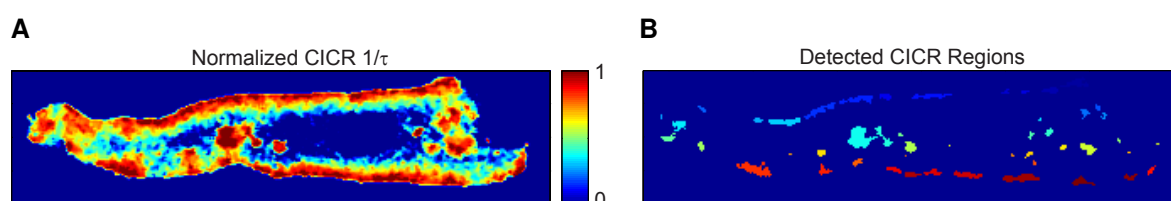


Figure 3.36: Identification of CICR sites. **A**, normalized CICR $1/\tau$ image for the top panel in figure 3.33B. **B**, the identified CICR regions encoded in different colors.

to be an optimal number to identify the EC-coupling sites. Figure 3.36B demonstrates such an example of identified EC-coupling sites.

3.3.5.4 Analysis of membrane-CICR properties

Thus so far I could deduct CICR sites, sizes and membrane properties and thus calculate useful parameters that characterized EC-coupling in these cells. Here the efficiency of CICR throughout the entire cell and the coupled membrane were calculated as,

$$\text{Efficacy of Ca}^{2+} \text{ release} = \frac{\text{Detected CICR Regions}}{\text{Cell Area}} \quad (3.18)$$

$$\text{Coupled Membrane} = \frac{\text{Membrane} * \text{Detected CICR Regions}}{\text{Membrane Area}} \quad (3.19)$$

All the available parameters are summarized in table 3.3.

3.3.6 RacET atrial myocyte displayed CICR failure

We have recently found that in transgenic mice expressing a constitutively active Rac1 (RacET mice) left atrial myocytes displayed a significant loss of T-tubular membrane when compared to the FVB/N mice (wild type, WT). However, the functional consequence of this remodeling on subcellular Ca²⁺ signaling remained elusive. Therefore I compared subcellular Ca²⁺ signaling in these cells by using the “pixel-wise fitting” approach explained above. While in the typical left atrial WT myocyte the peak amplitude was distributed rather homogeneously, the RacET cell displayed maximal amplitudes restricted to its circumvent (compare left and right panel of figure 3.37Aa). This difference is even more pronounced when analyzing the Ca²⁺ release period (1/τ, see figure 3.37Ac and 3.37Ad). Here Ca²⁺ release appeared in stripes throughout the cell in the WT myocyte but almost absent in the RacET cell (compare left and right panel of figure 3.37Ac, respectively).

The same cells were labelled with di-8-ANEPPS to reconstruct the plasma membrane (figure 3.37Ba). When overlaying membrane staining and speed Ca²⁺ release (figure 3.37Bb from figure 3.37Ac and 3.37Ba) it becomes apparent that (i) Ca²⁺ release hot spots colocalize with the plasma membrane and (ii) RacET myocyte display less Ca²⁺ release sites than WT myocyte. Moreover, when calculating the density of Ca²⁺ release sites for both situations, the RacET myocyte depicted an non-proportionally low density of Ca²⁺ release sites.

The “pixel-wise fitting” approach yielded quantitative information about EC-coupling thus allowing to quantitatively analyze CICR in these cells. Table 3.3 summarizes such analysis results.

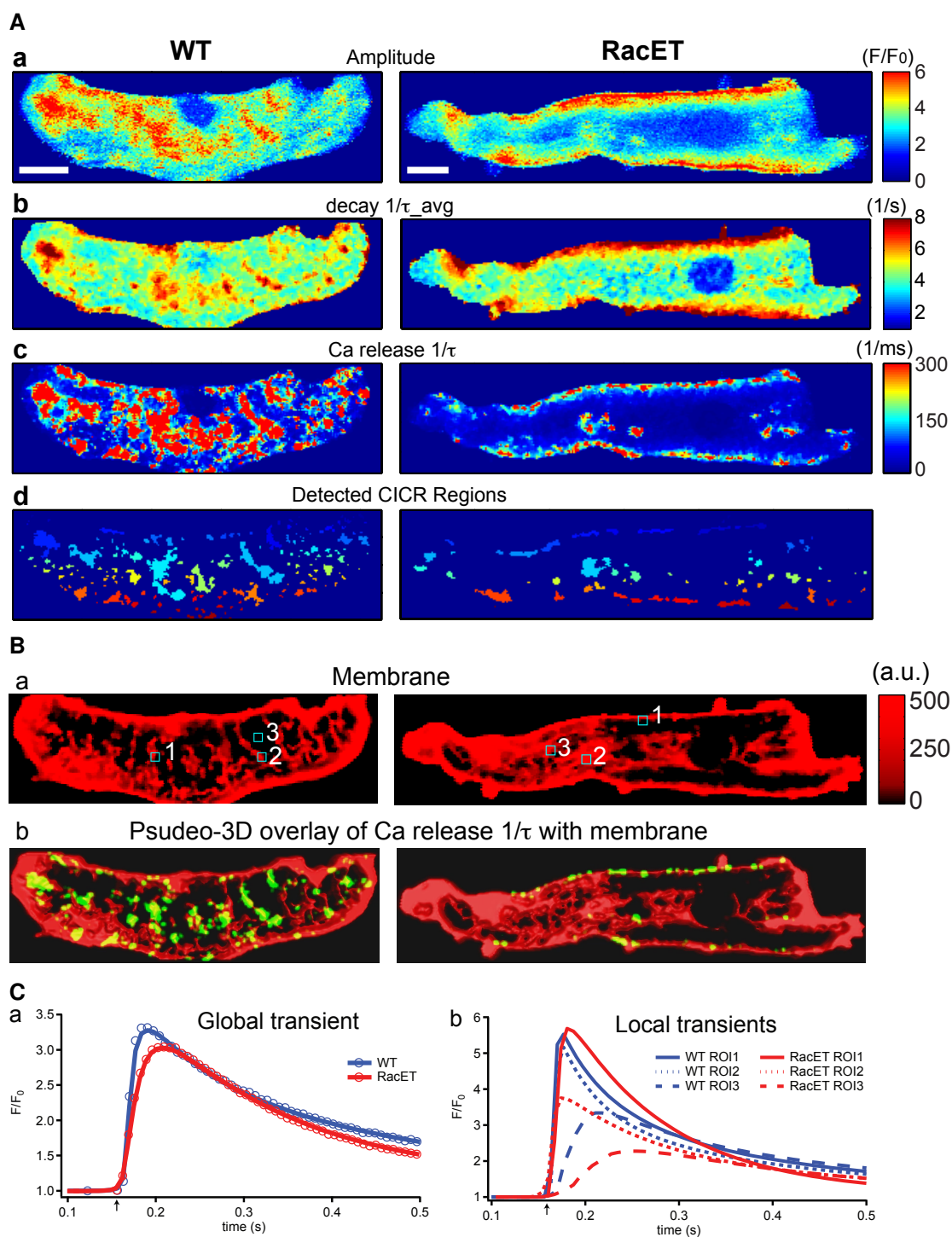


Figure 3.37: RacET atrial myocyte displayed CICR failure. **A**, the resultant images from pixel-wise fitting, including amplitude images (a), decay images (b), CICR $1/\tau$ images (c) and detected CICR regions (d, with different colors for different regions) are shown respectively for the cells from both the wide type (WT) and the RacET mouse. Scale bar: 10 μm . **B**, membrane staining images from both cells (a) and their psudeo-3D overlay with CICR $1/\tau$ images (b). **C**, Ca^{2+} transients from the entire cell (a) or from local ROIs (b) indicated with white boxes on membrane staining in B. Decay τ_{avg} was calculated according to formula: $\tau_{avg} = \frac{Amp_1 * \tau_1 + Amp_2 * \tau_2}{Amp_1 + Amp_2}$. Arrows in C show the electrical field stimulations. Note that the extracellular Ca^{2+} was 1.2 mM.

Table 3.3: Coupling analysis of CICR-membrane for RacET myocytes

Parameter	WT Mouse	RacET Mouse
Cell area (μm^2)	1105	1013
Number of Ca^{2+} release sites	158	63
Density of Ca^{2+} release sites ($/\mu\text{m}^2$)	0.143	0.062
Efficacy of Ca^{2+} release	0.21	0.14
Membrane area (μm^2)	342.3	341.2
Coupled Membrane	18.9%	15.5%

Note: The data shown here was calculated from the cells shown in figure 3.37.

From these data it became obvious that EC-coupling was severely impaired in RacET left atrial myocytes, not only because of plasma membrane remodeling (loss of T-tubular membrane) but apparently also because the “remaining” plasma membrane only displayed a rather low density of coupling sites. Both processes will contribute to the impaired contractility of the whole atria reported elsewhere¹²¹.

3.3.7 The role of subcellular Ca^{2+} handling for cardiac alternates

A rather broad range of phenomena can cause cardiac arrhythmias. On the tissue and single cell level, inhomogeneities in the excitability of myocytes are believed to be an important substrate for arrhythmic behavior^{191,223}. An important mechanism leading to such heterogeneities is the occurrence of cardiac alternans. This can be observed on the whole organ (even in in-vivo ECGs) “down” to the single cell level^{59,176,189}. The concomitant occurrence of mechanical, electrical and Ca^{2+} alternates has been reported earlier²³⁵ but the contribution of subcellular alternans in Ca^{2+} release has remained elusive and often been neglected. By using the pixel-wise fitting approach to quantitatively analyze EC-coupling also on a subcellular level I thought of investigating this further. On the tissue and single cell level, rapid changes (increases) in the pacing frequency are likely method of inducing the phenomenon of alternans^{3,161}.

3.3.7.1 Rat ventricular CICR stability and algorithm reliability

Before characterize the subcellular Ca^{2+} alternans, I evaluated the reliability of the fitting strategy on myocytes without Ca^{2+} alternans. For this I used Fluo-4-loaded rat ventricular myocytes (DIV0) and recorded 5 consecutive Ca^{2+} transients after the cell reached a steady state with a pacing frequency of 2 Hz and subjected them to the pixel-wise fitting analysis. The detailed results of this analysis are summarized in figure 3.38. The amplitudes as well as the Ca^{2+} release function were distributed homogeneously (figure 3.38A) and the algorithm allowed reconstruction of the

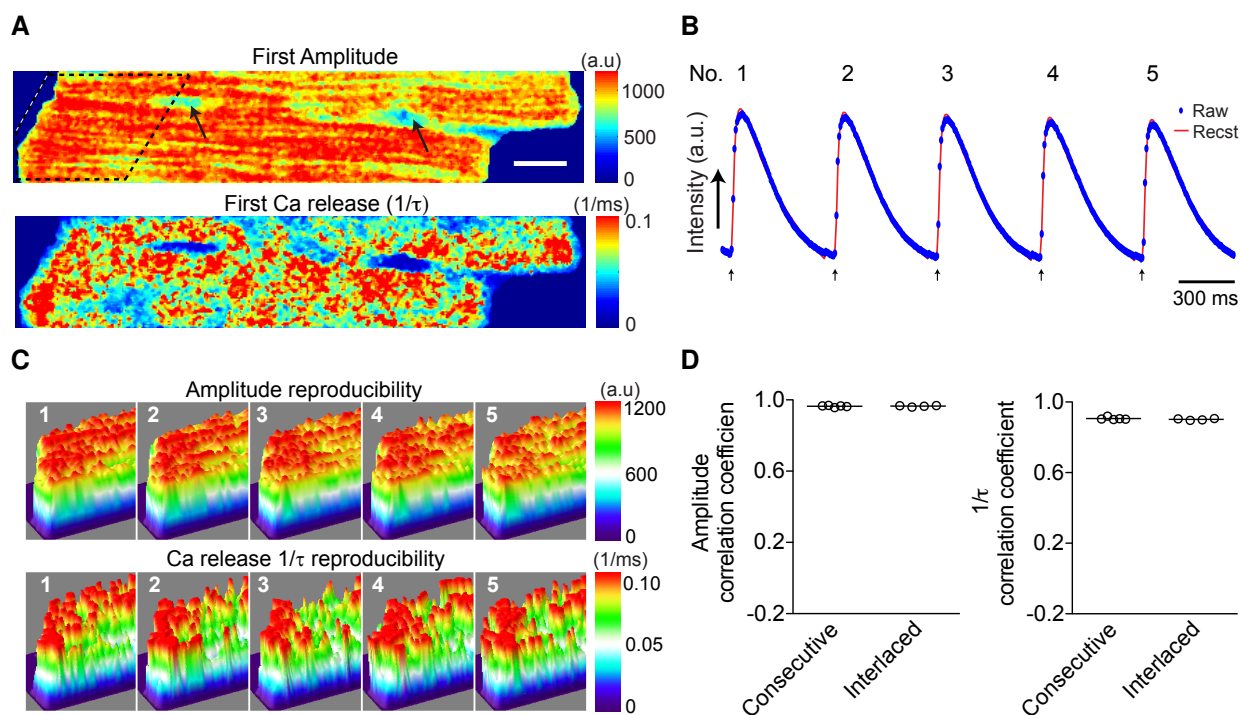


Figure 3.38: Rat ventricular CICR stability. **A**, one fitted sample amplitude and Ca²⁺ release τ images of rat ventricular Ca²⁺ transients. Scale bar, 10 μm . Arrows indicate nuclei. Panel **B** shows 5 consecutive Ca²⁺ transients of the same cell. Dots in blue, raw data points; red lines, reconstructed data points (Recst); arrows indicate the electrical field stimulation. **C**, 3D-surface plotting of the amplitudes and Ca²⁺ release τ values of the ROI indicated in A with dashed line. **D**, the correlation coefficients of fitted amplitudes and $1/\tau$ Ca²⁺ release values between two consecutive or interlaced transients. The cell was from a Wistar rat, and recorded with 1.8 mM extracellular Ca²⁺. Note that the $1/\tau$ images used to calculate the correlation coefficients in panel D were filtered with a median filter (size = $4.2 \times 4.2 \mu\text{m}$).

global Ca²⁺ transients (figure 3.38B). Since these transients did not display any properties of Ca²⁺ alternans, the analysis of subcellular Ca²⁺ handling should reveal reliable EC-coupling in between the individual Ca²⁺ transients. As illustrated in figure 3.38C the distribution of amplitudes as well as Ca²⁺ release displayed a high degree of reproducibility from transient to transient. Further analysis of the correlation between consecutive transients and interlaced transients demonstrated coefficients above 0.9 in both amplitudes and $1/\tau$ images, which also implied high reproducibility from transient to transient (figure 3.38D).

3.3.7.2 CICR dynamics after acceleration of the stimulation

To study the frequency dependent changes in EC-coupling I employed a protocol that involved a step-wise increase of the pacing frequency from 0.5 Hz to 4.0 Hz (at room temperature). The results of a typical experiments are summarized in figure 3.39. Figure 3.39A exemplifies representative global and local Ca²⁺ transients in steady state at the given frequencies, while figure 3.39B

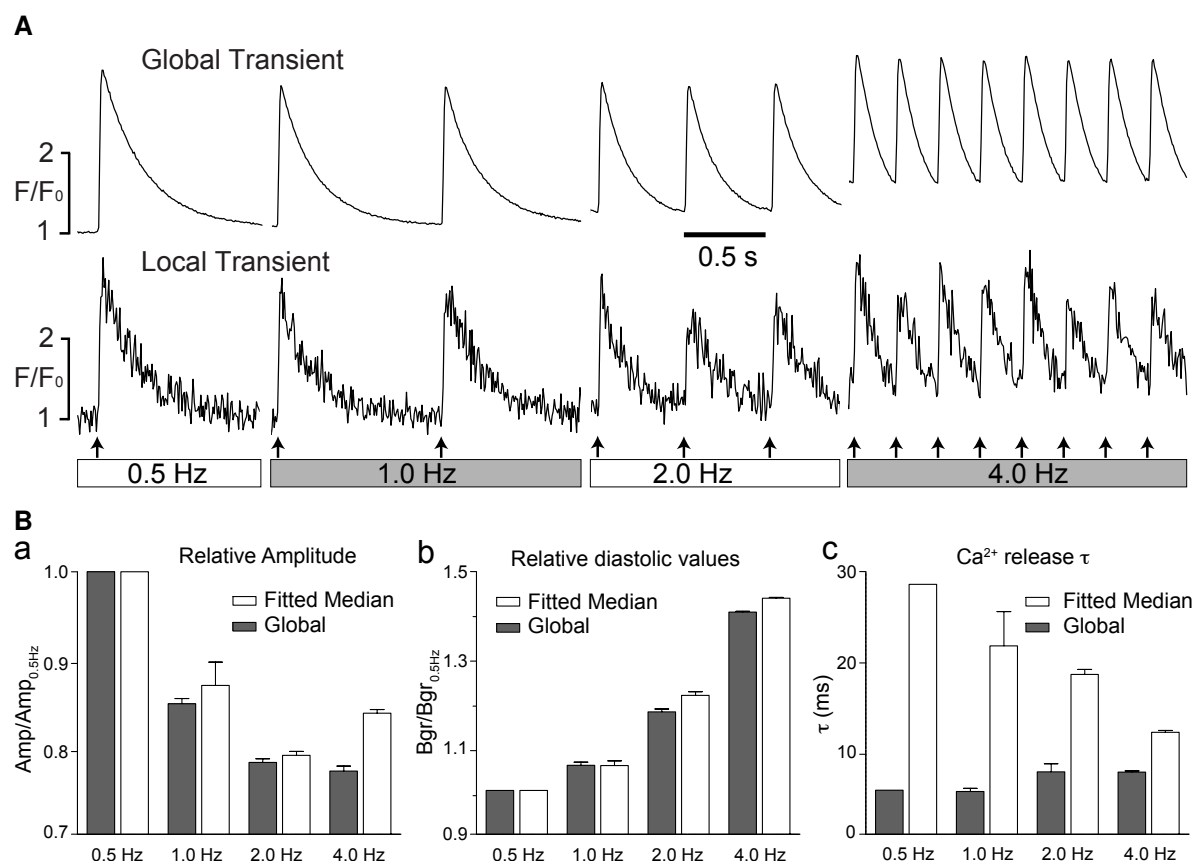


Figure 3.39: CICR dynamics upon pulse acceleration. **A**, global vs. local (raw data, $1.7 \times 1.7 \mu m$) Ca^{2+} transients. Arrows indicate the electrical field stimulations. **B**, changes of global vs. pixel Ca^{2+} handling parameter upon pulse acceleration, including amplitude, basal Ca^{2+} level and Ca^{2+} release τ values. Note that “fitted median” represented the median value of all the pixels that constitute the complete cell. Except the Ca^{2+} release τ values, all the data were normalized to the corresponding values obtained at 0.5 Hz. The myocyte was from Wistar Rat ventricle, and recorded with 1.8 mM extracellular Ca^{2+} .

illustrates the analysis of the amplitude, the diastolic fluorescence and the characteristic Ca^{2+} release value (from left to right). While the amplitude and the diastolic fluorescence displayed the anticipated frequency dependence (negative and positive, respectively), the results with respect to the Ca^{2+} release speed were unexpected, While the globally fitted (fitting the global averaged fluorescence) showed a positive frequency dependence (black filled bars in figure 3.39Bc), the medians from the “pixel-wise fitting” approach decreased with increasing frequency (white bars in figure 3.39Bc).

3.3.7.3 Subcellular Ca^{2+} handling in Ca^{2+} alternans

A close look at the Ca^{2+} transient at 4 Hz (figure 3.39A) revealed that, despite a stable global Ca^{2+} transient, the local Ca^{2+} signals displayed a noticeable variability, local heterogeneity. I wondered

whether these local instabilities might be precursor states to Ca^{2+} alternans. To study this in more details I designed an adapted experimental design in which cells were initially paced at 0.5 Hz and then the pacing frequency was abruptly increased to 4 Hz.

Figure 3.40 summarizes such experiments. While the recordings in the left column were obtained 1 min after the abrupt increase of the pacing frequency, the right column displayed results after 15 minutes of continuous pacing with the high frequency. Panel A of figure 3.40 exemplifies amplitude (top) and Ca^{2+} release speed (bottom) distribution of the first transient during recording periods with global alternans absent (left) and present (right). While subcellular alternans was visible in both amplitude distributions, local Ca^{2+} release only displayed appropriate inhomogeneities for situation of global alternans. Unexpectedly, local increase in the Ca^{2+} transient was slowed down in those regions that showed higher amplitudes (compare right upper and right lower panel in figure 3.40A). These observations are supported by the time course the local fluorescence as illustrated in figure 3.40B for three regions of interest (ROIs).

For the left part of the cell (boxed in figure 3.40A), the distributions of amplitude and speed of Ca^{2+} increase were re-plotted as 3D surface representations in figure 3.40C for every Ca^{2+} transient. The basic observations from panel A were substantiated. While the amplitude plots (upper two rows in figure 3.40C) display local beat-to-beat variability in an alternating manner (see arrows in this panel), the speed of Ca^{2+} increase (left lower part of figure 3.40C) lacked systematic variations. This picture dramatically changed when I analyzed Ca^{2+} transients recorded during global alternans. The right column of figure 3.40C illustrates the non-concordant changes of the amplitude (upper two rows) and the spread of Ca^{2+} increase (lower two rows). Surprisingly, the Ca^{2+} release showed an alternating pattern as the amplitudes, but in an opposite phase.

Further correlation analysis of the amplitude and Ca^{2+} release images confirmed the observations shown in figure 3.40C. Figure 3.40D summarizes the results. In the absence of global alternans with only microscopic alternans, the correlation coefficients of the amplitude images from two consecutive transients was already significantly lower than the coefficients between one and every second transient (interlaced coefficients), as shown in most left panel in figure 3.40D. This difference was not visible in the Ca^{2+} release panel (the second panel in figure 3.40D). When the global alternans developed, the consecutive correlation decreased significantly from 0.72 to almost zero with the interlaced coefficients unchanged (third panel in figure 3.40D). This change resulted in significantly increased difference between the consecutive and interlaced amplitude correlation, which was compatible with the alternating pattern of Ca^{2+} transients. The correlation of the Ca^{2+} release between consecutive transients was also decreased slightly, while the interlaced coefficients was increased significantly (the last panel in figure 3.40D), which highly implied

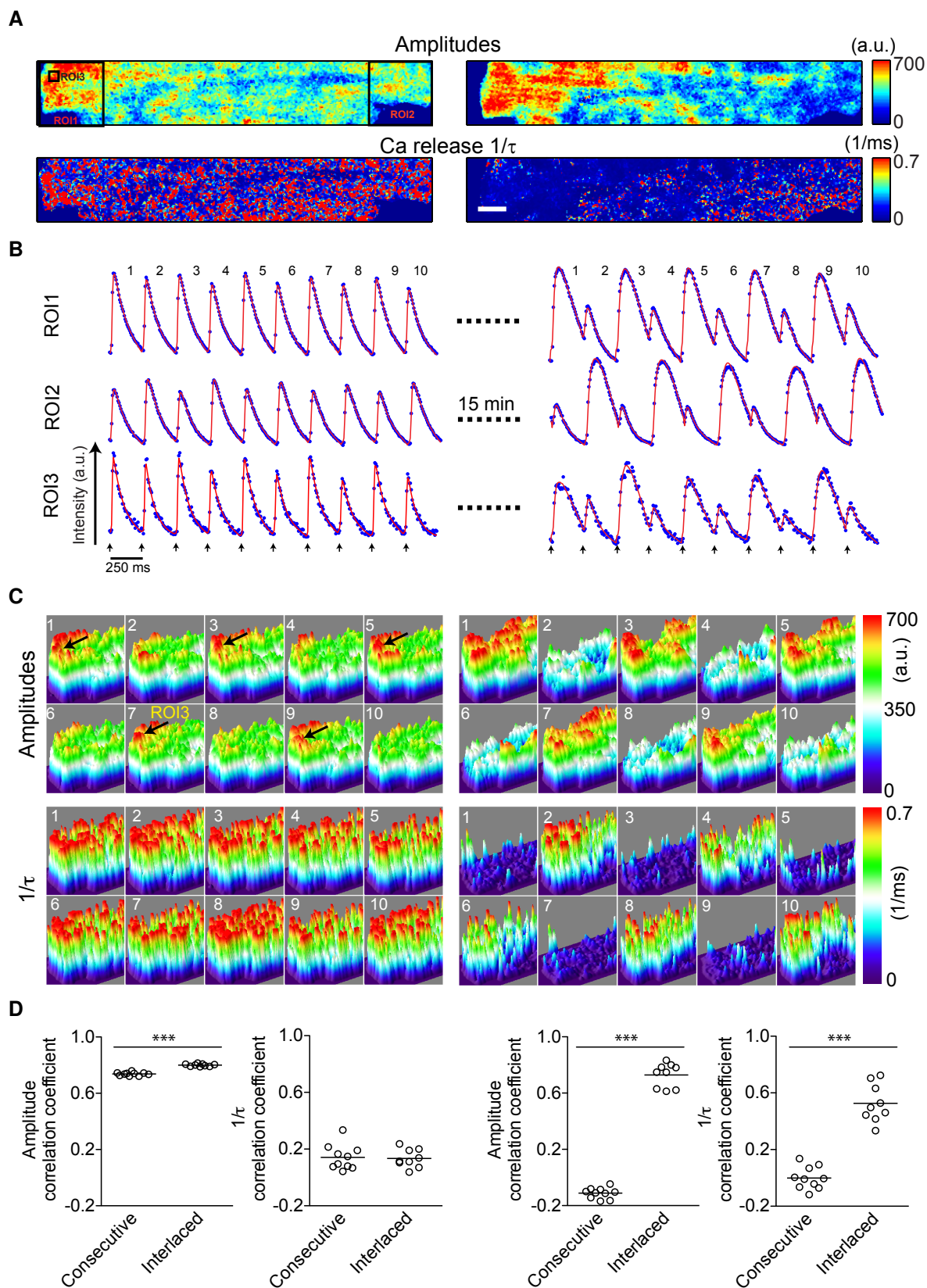


Figure 3.40: Analysis of Ca^{2+} alternans with pixel-wise fitting. **A**, a sample of fitted amplitude and Ca^{2+} release τ from a ventricular myocyte with slightly (left panel) and severely alternating (right panel) Ca^{2+} alternans. Scale bar, 10 μm . *To be continued on next page.*

a global Ca^{2+} alternans.

From these data I concluded that microscopic Ca^{2+} alternans as displayed in the left columns of figure 3.40 may be an early precursor of global Ca^{2+} alternans. The latter is known to be an important substrate for cardiac arrhythmia.

3.3.8 Final remarks for this section

The two examples (atrial myocyte remodeling and Ca^{2+} alternans) depicted in this section have illustrated that by using the pixel-wise fitting approach relevant and novel information can be extracted from high speed confocal Ca^{2+} recordings that are otherwise buried in the high noise levels associated with the necessary short pixel dwell time. This fitting approach was and is not designed to describe individual cellular and subcellular processes, it merely serves the function to offer a phenomenological description of the time course of a Ca^{2+} transient and thus helps to uncover the “real” Ca^{2+} signal in the noisy data.

Continued figure 3.40. B, local Ca^{2+} transients of ROIs indicated in A (black boxes in amplitudes panel) from slightly (left panel) and severely alternating (right panel) phases. Dots in blue, raw data points; red lines, reconstructed data points; arrows indicate the electrical field stimulation. *C*, the amplitudes and Ca^{2+} release τ images of ROI1 (indicated in panel A) were represented in 3D-surface plotting. Left panel, the cell in slightly alternating phase. Arrows indicate the ROI3 at different transients. Right panel, the cell in severely alternating phase. Panel *D* shows the correlation coefficients of fitted amplitudes and $1/\tau$ Ca^{2+} release values between two consecutive or interlaced transients with global alternans absent (left column) or present (right column). Note that the $1/\tau$ images were filtered with a median filter (size = $4.2 \times 4.2 \mu\text{m}$). The cell was from a Wistar rat, and recorded with 1.2 mM extracellular Ca^{2+} .

Chapter 4

Discussion

4.1 Optical recordings of action potential

The gold standard for recordings of action potentials in cardiac myocytes is the patch clamp technique. Despite various modes of this approach that also overcome inherent shortcomings of this technology such as perforated patch avoiding intercellular dialysis, all those approaches suffer from a rather low throughput. In this, optical technologies can overcome such limitations and offer medium to large throughput. The principles of this optical action potential recordings are well known for quite some time¹⁸² and have also been adapted for the cardiac myocyte^{78,79}. However, in most studies rather high indicator concentrations (up to 100 μM) and/or multiple signal averaging (up to 10 \sim 20 individual APs) were necessary to obtain optical AP equivalents with sufficient signal to noise ratio. Unfortunately such approaches did not allow the analysis of individual APs as might be necessary e.g. during cardiac alternans. In addition such high sensor concentration unavoidably resulted in alterations of the time course for the action potential, such as AP prolongation⁷⁸.

4.1.1 Validated improvements

The improvement was obtained by using spectrally extended filters (figure 3.1C) and by incorporating detectors with greatly enhanced quantum efficiency (figure 2.3B). When di-8-ANEPPS is excited at 460 nm, additional molecular constituents, mainly inside the mitochondria, are also excited and result in a significant fluorescence output, which is called "autofluorescence". The emission peak is spectrally located around 510 nm and can be bleached very quickly (data not shown). So the signal of the "green" channel (490 nm \sim 580 nm) will be perturbed to a larger degree than that of the red signal. This kind of asymmetric influence may introduce a ratio base-

line shift during illumination. To avoid introducing such additional signal component to the final fluorescence ratio, the emission below 532 nm was omitted (figure 3.1C). The increased detection efficiency allowed for a shortened staining time and a reduced concentration for dye loading (here 7 min vs. literature 20 min, and 5 μ M vs. any other higher concentrations, typically 100 μ M). It also enabled us to record single AP with sufficient signal to noise ratio while avoiding AP prolongation.

Single optical AP recordings provide new opportunities for application such as: (i) membrane potential changes like premature action potentials, EADs and DADs¹²⁸ can now be recorded, and (ii) minute alterations in the action potential can be resolved allowing a precise evaluation of cardiac safety according to FDA and EMEA requirements⁵. To further support this concept, optical recording has been adapted into a high throughput screening (HTS)-compatible workflow for primary isolated adult cardiac myocytes. The necessity to use immersion objectives (for high numerical aperture objective lenses and consequently a high photon collection efficiency) is compatible with screening concepts as recently shown¹⁴¹.

In comparison of optical and electrophysiological recordings of action potentials both approaches have their advantages and shortcomings. While the patch-clamp technique provides a plethora of variants to analyze individual membrane current components or even single ion channels, albeit with a ultra low throughput, optical AP measurements offer the unique possibility to generate AP data with a rather high throughput. For example, the data shown in figure 3.8B and 3.6B contained APs from at least 650 adult cells and 1000 neonatal cells. When used for the evaluation of compounds from a HTS campaign ("hit" or "lead" compounds), the optical approach can generate hundreds of thousands of action potential data in a reasonable short time scale.

4.1.2 Comparison of adult with neonatal ventricular myocytes in QT-screen

Optical high-throughput measurements of action potentials are a likely candidate approach for QT-screens of pharmacological substances as is requested by both, the FDA and EMA⁵. Beside reliable recordings modes, easy and reproducible handling of living cells is of prime interest. In this it is highly desirable to use cardiac myocytes rather than e.g. hERG-expressing HEK cells, since the former cell type resembles the entire complexity of cardiac action potentials. Neonatal cardiac myocytes are a rather popular cell model since isolation and culturing of these cells appears rather easy. In my attempt to validate optical AP screening I thus used both, neonatal and adult rat ventricular myocytes and challenged both cell types with various compounds with a well-established molecular effect.

The measured IC₅₀ values of quinidine both on adult and neonatal cells were around 10 μ M (figure 3.6B and 3.8B), which was in good agreement with electrophysiological data⁸⁵. As for the

4-AP, only marginal effects have been reported for neonatal cells¹⁰⁵. However, our data indicated similar response for both cell types (figure 3.6B and 3.8B). This might be due to the long time (usually 5 days after isolation for the formation of synchronized cell clusters) of in vitro culture which probably allowed the cell differentiation and the expression of I_{to} ⁷⁶. As expected, E-4031 showed no effect when used with adult cells, but a clear concentration-dependent AP prolongation for neonatal cells. Its IC_{50} (11.4 nM) was in good agreement with literature data (10 nM)^{234,247}. Although data shown here were only from neonatal and ventricular adult cardiomyocytes, the entire method could be applied to atrial myocytes and stem cell-derived myocytes without further adaptations. Taken together, our work-flow of optical AP measurements worked and generated reliable data, regardless of the cell types used in the experiments.

4.1.3 Benefits of genetically encoded membrane potential sensors

If cellular APs need to be followed over a longer period of time, e.g. for chronic treatments by hormones, possible shortcomings of di-8-ANEPPS as for probably all other small molecule dyes as well as patch-clamp based measurements will arise. An alternative approach is to utilize genetically encoded membrane voltage sensors, such as FlaSH^{74,193}, SPARC⁶, Ci-VSP¹⁴³, or Mermaid²¹⁴. These sensors can be targeted to specific cell types or even specific organelles within the cell. Among them, Mermaid is the best sensor for AP measurements, which provides a high intensity ratio change and fast kinetics, and has been verified in neonatal cardiac myocytes²¹⁴ and zebrafish myocytes²¹². Our data showed that most Mermaid proteins localized in the plasma membrane (figure 3.10), with a small portion in the perinuclear region most likely representing rough ER and/or Golgi localization (figure 3.12C). Functional data (figure 3.14A) indicated that the ratio changes during an AP are around 25% higher with Mermaid in comparison to di-8-ANEPPS. Nevertheless, the responses of Mermaid at room temperature were still not fast enough to follow an adult rodent AP, especially during the upstroke phase of an AP. In a conclusion, Mermaid is a promising candidate for monitoring adult cardiac APs under chronic conditions, but still needs further structural optimization for improving kinetic responses.

4.1.4 Further perspectives about optical AP recordings

Although the recording process for each cell could be finished within 10 seconds, the recordings of 30 random cells still occupied 20 minutes with our setup, since all the steps including selecting cells, focusing, illuminating cells, recording signals and saving data were performed manually. In principle, all of these steps can be automated by a motorized stage in an integrated system,

which will make it possible to finish a single compound treatment in less than 5 minutes (6 seconds for each cell, and 40 cells per treatment). Five minutes per data point are not short enough to fulfill the drug discovery requirements and to take full advantages of the properties of this optical approach. A perspective solution would be a high-speed CMOS camera as already announced by camera manufacturers⁴⁴. With such a sensitive camera offering acquisition speeds of up to 1000 frames/second, it would be possible to record 20 ~ 30 cells simultaneously, and for each concentration only one to two recordings would be sufficient to provide an accurate APD. With this, a real medium-throughput screening or even HTS would be available.

4.2 The effects of CytoD in the culture of cardiomyocytes

As mentioned above, apart from technical prerequisites, automatic screening and testing of hormones and/or drugs often requires stimulation protocols lasting from hours to days. When studying cardiac myocytes over such an extended time period, the process of remodeling of the cells in culture becomes very important. The fact that adult cardiac myocytes de-differentiate in culture is well known for a long time¹³⁷ and my group has already taken measures to minimize such processes^{77,219}. In this thesis I have taken such efforts a major step forward by investigating whether and how the culture supplement CytoD might exert beneficial effects on this de-differentiation process. During this study I found that CytoD affected remodeling significantly and largely prevented T-tubule loss. Interestingly, remodeling of the T-tubular system is a concomitant process to many cardiac diseases such as e.g. the transition from compensatory hypertrophy to heart failure and thus the interaction of CytoD and T-tubular remodeling might shed new light on the role of the cytoskeleton in such remodeling processes in general.

4.2.1 Rat ventricular myocytes undergo remodeling after isolation

Isolation of adult cardiomyocytes is usually performed with special enzyme cocktails containing collagenases and proteases¹⁰⁰. During the isolation process, the extracellular matrix proteins in the space between the cells, are digested and destroyed, such that cardiomyocytes can be isolated/released from the tissue. Meanwhile, the mechanical force that is supported by the ECM inside the heart tissue is also relieved, and accordingly, the Z-disk/Z-line structure is loosened. Then the cell starts remodeling, probably first with respect to its structure and also with respect to its function. This notion was supported by our cytoskeleton staining data. In our investigation, isolated adult rat ventricular myocytes lost their Z-line and M-line first at DIV1 (figure 3.22D), whereas T-tubule structure (figure 3.21C and 3.22A) remained intact. Following the loss of Z-disk

and the disappearance of Z-line/M-line, some cytoskeleton proteins, especially F-actin, probably detaches from the Z-disk, which could accelerate its dynamic polymerization/depolymerization processes, since it has more freedom at its two ends.

The cardiac T-tubule network is extremely dynamic¹³⁹, and a hypothesis on the regulation of the T-tubule in three levels has been proposed recently⁹³. First of all, some specific proteins (e.g. BIN1⁸⁶) result in the formation of tubular invaginations of the cell membrane and recruitment of the appropriate ion channels. Subsequently, a second class of regulatory molecules sensitive to biomechanical factors (e.g. JP-1/2^{110,216}) triggers appropriate T-tubule/SR interaction. A third level of biomechanically sensitive regulatory molecules (e.g. Tcap¹⁰⁸) are responsible for the dynamic regulation of the T-tubule system when conditions are changed physiologically. Changes to the biomechanical conditions of the heart may trigger inappropriate reductions or alterations in the regulatory components at any level, and therefore they may all be important during the *in vitro* culture of the myocytes, as supported by the observation of T-tubules at DIV3 in figure 3.21. A direct outcome of T-tubule loss was the increased EC-coupling failures, as evidenced by a decrease of fractional Ca^{2+} release (figure 3.20Bc) and an increase in the dyssynchrony index of Ca^{2+} release (figure 3.23). Following loss of F-actin and EC-coupling failure, it was not surprising that the contraction decreased by more than 60% (figure 3.19).

The molecular complex responsible for the interaction between SR and myofibrils remain unknown. However, ankyrin1 and obscurin have been involved in this interaction^{8,177}. Ankyrin1 is a 155 amino acid small protein, containing a transmembrane domain responsible for its anchorage to the SR followed by a short cytosolic tail⁸⁸. Obscurin is a giant sarcomeric protein of 800 kD that binds to titin and has been proposed to mediate interactions between myofibrils and other cellular structures¹¹¹. The cytosolic region of ankyrin 1 has been found to interact with the C-terminal region of obscurin, thus contributing to the format a molecular link between the SR and the Z-disk/M-line⁸. Disruption of Z-disk/M-line during the *in vitro* culture will ultimately affect SR organelles. After 3 days culture, the myocytes' SR Ca^{2+} content was decreased by 35% (figure 3.20Bb).

Taken together, my data suggests a three-step remodeling process during *in vitro* cultivation of adult rat ventricular myocytes: i) loss of Z-disk/M-line; ii) F-actin detaching and iii) T-tubule loss. Following these structural changes the Ca^{2+} handling organelle and contractility will decrease accordingly.

4.2.2 Improved culture of adult cardiomyocytes with CytoD

CytoD is a fungal metabolite that suppresses cytokinesis by blocking the formation of contractile microfilament structures, which results in multinucleated cell formation, reversible inhibition of cell movement, and cellular extrusion³⁷. Our starting points were that high concentration of CytoD (40 μM) did not disrupt EC-coupling, but was beneficial for long term culture of cardiomyocytes^{40,119}. In our study 40 μM CytoD also diminished the loss of Ca^{2+} cycling but left us with initial doubts that the T-tubular arrangement was significantly altered (figure 3.16C).

In a systematic approach I set out to explore the potential of CytoD as a culture supplement by evaluating Ca^{2+} transients as an assay readout for concentration response relationships. Initial experiments demonstrated a good concentration-dependent preservation of Ca^{2+} cycling with an EC_{50} of 0.3 μM (figure 3.17B). A concentration 0.5 μM preserved DIV0 conditions for up to 3 days extremely well. This initial notion was substantiated in additional studies investigating a plethora of physiological parameters such as the post-rest behavior of Ca^{2+} transients (figure 3.18), the fractional Ca^{2+} release and removal (figure 3.20), the Ca^{2+} release synchrony (figure 3.23), and the contractility (figure 3.19). The principle result of all of those experimental series was that CytoD at a concentration of 0.5 μM preserved the structural and functional properties of the cardiomyocytes up to 3 days during in vitro culture.

Reports on Ca^{2+} measurements in the presence of CytoD are rather sparse. In a 2-photon imaging approach with 50 μM CytoD, recording of intracellular Ca^{2+} transients in Langendorff mouse hearts had been successful¹⁷⁹, but the transients could not be compared to control conditions, because the mechanical uncoupling was a necessary requirement for these technically demanding experiments. Leach et al. recorded line-scans in the presence and absence of 40 μM CytoD during a culture period of 4 days and described severe alterations of Ca^{2+} handling, but did not include a statistical/quantitative analysis¹¹⁹. In contrast to our current study, acute effects of CytoD (40 μM) have been investigated⁹⁰.

Under physiological Na^+ concentrations, heterologously expressed NCX displayed a 40% reduced activity in the presence of 1 μM CytoD¹⁷⁰. In ventricular myocytes I did not find changes in NCX activity after CytoD (0.5 μM) treatment at DIV0, but a slight increase of the time constant τ during the caffeine application at DIV3 (figure 3.20Ca). The obvious differences in the functional parameters of the cardiac myocytes under CytoD treatment between our study and other reports can most likely be explained by different concentrations of CytoD. While previous reports mostly used between 10 and 80 μM CytoD^{20,119,134,179,215}, our experiments were performed with only 0.5 μM CytoD in the culture medium (figure 3.18 ~ 3.21).

I was particularly surprised by our finding that the optimized CytoD concentration of 0.5 μM

conserved the contractility of myocytes, since CytoD was traditionally used as a mechanical uncoupler^{9,20,35,237}. However, similar to the above, I believe that this is a concentration dependent behavior because CytoD at a concentration of 4 μM had no effect on the contraction in cat cardiomyocytes²¹³. In addition in Langendorff-perfused hearts 5 μM CytoD was determined to be the minimum concentration that reliably reduced the developed pressure by more than 90%⁹. Although those results were not in good agreement with each other, the minimum concentration for mechanical uncoupling should be above 5 μM , according to the pharmacological concentration-effect relationship¹⁶⁹.

Based on these points, I conclude that 0.5 μM CytoD is the optimal concentration to conserve cellular function over a culture period of up to 3 days. This is a sufficient time to enable the expression of exogenous proteins and genetically encoded biosensors^{77,219} in cardiomyocytes, and therefore can serve as an improved cellular model for genetic as well as for pharmacological manipulations in vitro.

4.2.3 Possible mechanisms underlying CytoD effects

CytoD primarily acts on actin^{26,37} and leads to mechanical uncoupling with a concentration above 5 μM , but does not show mechanical uncoupling at concentrations of 0.5 μM ^{9,213} (figure 3.19). Investigations of molecular mechanism of CytoD revealed that CytoD binds to actin to prevent further polymerization/filament elongation in a concentration range of 0.1 ~ 1 μM ^{30,61}.

Our data as well as previous reports suggested that the effects of CytoD on cardiomyocytes are concentration dependent. At low concentrations, e.g. 100 ~ 500 nM, CytoD exerts its action of inhibiting actin depolymerization by binding to its barbed end^{26,37}. Higher concentrations (e.g. above 5 μM) can decrease the Ca^{2+} sensitivity of myofilaments^{34,35} and are thus usually used as a mechanical uncoupler. However, it is still not clear whether the inhibition of polymerization, either at the optimal or high concentrations, dominates in adult ventricular myocytes, where the F-actin is more stable³⁴ due to capping proteins at both ends^{72,241}. The present work supports the notion that CytoD stabilizes, rather than disrupts, F-actin filaments in cultured myocytes. This effect is consistent with the observation that CytoD reduced changes in cell shape in culture (data not shown) that might result from changes in actin cytoskeleton, and that CytoD helped to maintain the morphology and function of cardiomyocytes.

However, it seems that CytoD might do something more than stabilizing F-actin. FFT power analysis demonstrated that either 0.5 or 40 μM CytoD completely prevented Z-line from disappearing, while only had moderate effects on the M-lines. The mechanism underlying Z-line/M-line preservation by CytoD are less clear. Since F-actin is anchored to Z-disk by a major component

of the Z-line, α -actinin⁶⁴ (figure 1.5), a direct speculation is that CytoD might also act on other proteins located inside the Z-disk or stabilize protein-protein interactions inside the Z-disk, such that the Z-disks were also stabilized during the in vitro culture. The stabilization of Z-disk may also contribute to the stabilization of the M-line, since Z-disk and M-line are connected by some giant muscle proteins, like titin⁶⁸. However, this kind of indirect stabilization of M-line might be weaker than that of Z-disk, such that only moderate M-line preservation was observed (figure 3.22Dc) even with traditionally high concentration of CytoD (40 μ M). A direct outcome of such a stabilization would be a delayed reduction of EC-coupling and delayed induction of Ca^{2+} release dyssynchrony during culture. Besides the stabilization of Z-line/M-line, higher concentrations of CytoD could still induce additional effects, such as inducing denser or “crowded” T-tubule (figure 3.16C) and accordingly higher amplitudes of Ca^{2+} transients (figure 3.16B).

4.2.4 CytoD as a pharmacological tool to study cardiomyocyte remodeling

As depicted in figures 3.17 ~ 3.21 the presence of 0.5 μ M CytoD conserved the functional properties of ventricular myocytes in culture. Although it was reported before that T-tubular remodeling could be prevented by high CytoD concentrations, our results strongly discourages the application of such high concentrations, since 40 μ M CytoD clearly induced highly artificial T-tubules “crowding” (figure 3.16C). From this I conclude that the application of 40 μ M CytoD substituted one kind of remodeling, i.e. loss of T-tubular structures, by another one, i.e. T-tubular “crowding”. Here, I present evidence that after titration of the CytoD, one can find an optimal balance that resulted in a conservation of the regular cross-striational arrangement of T-tubules (figure 3.21A).

The addition of an optimal concentration of CytoD (0.5 μ M) as a culture supplement, prevented culture-dependent remodeling in both morphological and functional aspects. Culture-dependent alterations of functional properties can be mainly related to the loss of T-tubules and the resulting loss of LTCC-RyR interactions. Reduction in T-tubules most likely also caused a reduction in dyadic coupling and generation of orphaned RyR that both contribute to the reduced fractional Ca^{2+} release observed in this study (figure 3.20Bc). These findings suggest a possible link between remodeling in cytoskeletal components on one hand and the observed T-tubular remodeling and appearance of orphaned RyR in many cardiac diseases^{83,233}. It will thus be interesting to extend the findings and concepts described in the current report for cultured cardiac cells onto mechanisms of plasma membrane remodeling observed e.g. following myocardial infarction¹²³, in diabetic cardiomyopathy^{136,204}, during heart failure in general^{136,126,200} or especially during the transition from hypertrophy to heart failure²³³. We speculate whether short term culture (3 days to additionally allow virus mediated genetic manipulation) might be an appropriate model system

to obtain initial insights into cellular structural remodeling during cardiac diseases.

4.2.5 Summary and perspectives

The remodeling processes after adult cardiomyocyte isolation were explored, and the potential mechanisms that CytoD preserved cultured cardiomyocytes are proposed. Our data also provide some evidence for an interplay between actin remodeling and loss of T-tubules. The preservation of the T-tubules for at least 3 days in culture without impairing functional parameters adds a novel quality to the single cell based investigations that rely on culture, e.g. for viral gene manipulation in vitro.

4.3 Computer-aided cardiac CICR analysis

4.3.1 High-speed/resolution confocal Ca^{2+} imaging and inherent problems

As discussed in section 4.2, culture-induced dyssynchrony of Ca^{2+} release can be characterized with confocal microscopy in the line-scan mode (figure 3.23). However, the information that can be obtained from line-scan is limited, just one spatial dimension over time. Nowadays, 2D laser beam scanner enables fast confocal microscopes with a 2D scanning speed up to 150 Hz (figure 3.27)¹⁸⁸. With the fast imaging of the CICR processes, Ca^{2+} release dyssynchronies can be clearly visualized (figure 3.37 and 3.40). Whithin such data, however, the pixel signal is so noisy that detailed analysis and interpretation of spatiotemporal aspects of Ca^{2+} signaling are rather difficult.

Such pixel signals are composed of three major components, the “true” Ca^{2+} signal, photon statistical noise and the noise contributed by the laser and the detectors with electronics. Both photon statistical noise and the electronic noise can be minimized, but only in a small range. High concentration of Ca^{2+} sensor molecules might help to improve the signal to noise ratio, but it will also comprise the kinetics of the Ca^{2+} transient signal and increase the Ca^{2+} buffering in the cytosol. I wondered whether there was a “reliable” strategy that can decompose the measured pixel signals into the “true” Ca^{2+} signal and the noise, such that I can simply focus on the the “true” Ca^{2+} signal.

4.3.2 Algorithm design of “pixel-wise fitting”

Traditional image denoising, such as averaging in the temporal or spatial dimension, convolution with blurring²⁴⁰, fast Fourier Transform (FFT)-based filtering¹¹⁴, etc., are the first choices to be

tested to approximate the “true” Ca^{2+} signals. All these methods already have mature algorithm designs and are robust for preprocessing of raw data, however, these methods either alter the fast upstroke phase of the real Ca^{2+} transients or can not remove noise completely. Furthermore, after image denoising, additional analysis is still necessary to extract CICR information from these “denoised” data. I wondered whether there might be a method that could overcome the noise disturbance and extract these CICR information directly without altering the properties of real pixel Ca^{2+} transient signals.

According to the greedy algorithm⁴⁷, a global optimum is expected if the problem is solved by making the locally optimal choice at each stage. In the 2D Ca^{2+} transient case, if all the local Ca^{2+} transients are analyzed optimally, a global Ca^{2+} transient might be solved. Thus I tried to find out the “true” Ca^{2+} signals for all pixels. With the prerequisite that all the noise over time follows a Gaussian distribution, a model-based fitting seemed to be a good option^{69,73}. This strategy intends to find out suitable parameters for a given mathematical model, such that the final difference between the measured signal and the hypothetical signal from the model is the minimum. If the noise follows Gaussian distribution, it will not shift the hypothetical signal in any specific direction, such that the “hypothetical” signal is the “true” Ca^{2+} signal. Then all the “hypothetical” pixel signals would be a global optimum of the entire 2D Ca^{2+} transient signals (figure 3.24).

4.3.2.1 Design of mathematical function for rodent cardiac Ca^{2+} transient

Physiologically, the Ca^{2+} transient is determined by lots of components, such as Ca^{2+} influx, Ca^{2+} release, intracellular Ca^{2+} buffering, Ca^{2+} removal, etc. All these components have been simulated successfully in the modeling field¹¹², however, those mathematical functions are apparently too complicated to be fitted to pixel-wise Ca^{2+} transients. In principle, these components can be simplified into two: i) Ca^{2+} increase contributed by Ca^{2+} influx via LTCC and Ca^{2+} release via RyR from SR; ii) Ca^{2+} removal contributed by Ca^{2+} pumping via SERCA and Ca^{2+} efflux via NCX, as discussed below.

(i) Ca^{2+} increase process RyR is the major channel that accounts for the Ca^{2+} release from SR, which contributes about 92% Ca^{2+} to the Ca^{2+} increase in rodent cardiomyocytes¹⁴. Fast Ca^{2+} imaging data has shown that RyR opens within 0.5 ms upon Ca^{2+} binding²⁴⁴. Compared to the common time that a typical upstroke of Ca^{2+} release lasts, it is reasonable to assume that RyR channels operated in a way of “on” or “off” mode, not in a gradual mode, such that the maximum speed of Ca^{2+} release occurs at the beginning, but not in the middle or late phase of this process. An exponential function seems to fit well to this process. Additionally, rodent AP-

induced Ca^{2+} influx via LTCC roughly follows a Gaussian distribution²⁴³, which might contribute to the maximum speed at the beginning of the upstroke phase, although only in a very small number (7% to the global Ca^{2+} increase¹⁴). These information might explain the reason that the ExpConvExp function fitted better to the measured Ca^{2+} transient signals than the GauConvExp function (figure 3.28B).

(ii) Ca^{2+} removal process Two major proteins are responsible for Ca^{2+} removal: NCX and SERCA. NCX is a passive Ca^{2+} transporter that follows the Nernst equation. During the Ca^{2+} removal process, NCX contributes to Ca^{2+} efflux in the beginning phase that roughly follows an exponential decay²¹⁸. SERCA is an active Ca^{2+} pump, its activity depends on the intracellular Ca^{2+} concentration¹⁶ with a Michaelis Constant (Km) of 300 nM. During a typical decay phase of a Ca^{2+} transient, the free Ca^{2+} usually goes from 700 nM to 100 nM¹⁴. In this dynamic range, the Ca^{2+} sensitivity of SERCA, and accordingly, the Ca^{2+} extrusion speed, will decrease in an exponential decay-like pattern. In addition, the intracellular passive Ca^{2+} buffering by Troponin C is quite significant and affects the $[\text{Ca}^{2+}]_i$ ¹⁷, which contributes more Ca^{2+} at lower $[\text{Ca}^{2+}]_i$. A single exponential decay function, the ExpConvExp function, probably can not fully approximate all these components during the Ca^{2+} removal process, while a double exponential decay function, the ExpConvdbExp function, can better describe the Ca^{2+} extrusion process for pixel-wise simulation (figure 3.28B).

Our fitting results demonstrated that the ExpConvdbExp function, an exponential function for the Ca^{2+} upstroke phase convolved with a double-exponential decay function for the Ca^{2+} removal process, was the best mathematical function to describe a Ca^{2+} transient. It could extract almost all the information out of the noisy pixel Ca^{2+} transients (figure 3.28), with the final resultant residual well below 5% of the measured signal.

4.3.2.2 Reliability, reproducibility, extendability, efficiency and limitations of the fitting strategy

Our fitting strategy exhibited high reliability, even the “cross-striation” pattern of Ca^{2+} release can be reproduced from the rat ventricular myocytes (figure 3.30 and 3.31). The pixel-wise fitting strategy also demonstrated high reproducibility. In an example myocyte from left atrium of RacET mouse (figure 3.33), both the pixel amplitude and Ca^{2+} release τ images during the electrically stimulated steady state demonstrated high correlation of above 0.8 (summarized in table 3.2). Similar reproducibility was also seen in rat ventricular myocytes (figure 3.38).

Our ExpConvdbExp function still remains simple for further modifications, such as incorporating a new function to consider larger Ca^{2+} influx than that in rodent cardiomyocytes²⁴³. Another

extendibility is to combine this pixel-wise fitting strategy with the “peeling” algorithm⁷³, in which overlaid Ca^{2+} transients can be fitted and “peeled” off one by one, such that EADs or DADs can be separated from Ca^{2+} transients. However, it is beyond of this thesis and will not be discussed here. Our fitting strategy did not require any pre-processing before the entire fitting, even when the SN ratio was below 2.0. Its high tolerance to noise makes it very flexible.

Our fitting strategy was possible to be used for everyday calculation. For a common Ca^{2+} transient with a dimension of $512 \times 80 \times 150$ points, it usually takes 25 ~ 40 minutes on a common laptop CPU (Intel Core duo 2 T5500, 2 CPU cores at 1.6 GHz, with Matlab 2009a).

There is an issue in the pixel-wise fitting. Contraction could shift the pixel Ca^{2+} content outside of the pixel focus, which introduces a fast Ca^{2+} decay, and probably also a restoration of Ca^{2+} (figure 3.32). Our mathematical function was not designed to cover this issue. Two means have been introduced in the corresponding result section.

4.3.3 Biological relevance

Pixel-wise fitting with the ExpConvdbExp function generates 7 parameters, most of which can be used with independent meanings (figure 3.29). The first one is the amplitude, the most substantial parameter to evaluate spatiotemporal variations, such as Ca^{2+} alternans (figure 3.40). The Ca^{2+} increase τ is also readily available, which reflects the Ca^{2+} increase velocity. If the Ca^{2+} normally increases, it implies that the coupling between the LTCC and RyR is successful, CICR initiating sites (visualized as “sparking” sites in figure 3.36B) will form; otherwise coupling failures will be visible (dark regions in figure 3.36B). Taking the membrane staining into account (figure 3.37Ba), the CICR initiating sites of a cardiomyocyte from left atrium of RacET mouse were visualized clearly (figure 3.37Bb), which will be discussed in next section.

Two decay τ values are also available. Since I am not interested in this pattern, no further data or discussion are presented except very common τ_{avg} images were used to show the fitting qualities.

The entire fitting can be monitored with the standard fitting parameter R^2 . Depending on the data quality, R^2 was in the range of 0.5 ~ 0.7, leaving out 30% ~ 50% noise, which was compatible with our noise estimation ($CV_{noise} \approx 40\%$).

At the end of the fitting process it was possible to reconstruct the Ca^{2+} transient on a pixel level with any given temporal resolutions (figure 3.31), since now the Ca^{2+} transient is described by an equation. Such reconstructed Ca^{2+} transients only contain spatial noise and are basically noise free (See supplementary movie: reconstructed RacET).

4.3.4 Case study: role of Rac1 in left atrial EC-coupling

The Rho family of small guanosine triphosphatases (GTPases) are a subgroup of the Ras superfamily of GTPases. Among this family, Rac1 is one of the most extensively studied members. It has been shown to be expressed ubiquitously, and to play a fundamental role in a wide variety of cellular processes, including actin cytoskeletal reorganization, cell transformation, the induction of DNA synthesis, superoxide production, axonal guidance, and cell migration²⁴. Just like Rho⁹⁶, Rac1 exists in two conformational states: GTP-binding form and GDP-binding form. Stimuli-activated receptor kinases, G proteins, or adhesion molecules can act as guanine nucleotide exchange factors (GEFs) to accelerate the dissociation of GDP from Rac1 and binding of GTP to Rac1, resulting in further signaling, while GTPase-activating proteins (GAPs) inactivate Rac1 by promoting the GTPase activity of Rac1 and hydrolysis of GTP. A third regulator of Rac is guanine nucleotide dissociation inhibitors (GDIs). Its effectors include, IQGAPs²⁸, p21-activating kinases (PAK)⁵⁸, IRSp53/WAVE¹³⁸, etc.

In cardiomyocytes, Rac1 activation leads to several major downstream responses, such as induction of ROS⁷¹ and cytoskeletal remodeling²⁹, both of which lead to hypertrophic responses. Adenoviral-mediated expression of constitutively activated Rac1 (V12rac1) led to significant reorganization of the actin cytoskeleton into sarcomeric structures in neonatal cardiomyocytes, while dominant-negative Rac1 (N17rac1) attenuated these responses¹⁶⁵. Specific knockout of cardiac Rac1 decreased myocardial hypertrophy by decreasing the NADPH oxidase activity, superoxide anion production, signal-regulating kinase 1 (ASK1) and NF- κ B activity upon the inducement by Angiotensin II¹⁸⁷. In vivo overexpression of constitutively active Rac1 (RacET) revealed two different phenotypes: both atrial and ventricular dilation, and hypertrophy in juvenile mice²⁰⁶. Myofibrillar structure was not altered, while the contractility was increased by 46%. Meanwhile Rac1 induced significant PAK activation and redistribution in striated pattern with bands between Z-discs. Besides altered focal adhesion changes, Rac1 also increased the atrial natriuretic factor (ANF) and β -myosin heavy chain (β -MHC) gene expression, decreased the expression of α -myosin heavy chain (α -MHC) and SERCA²⁰⁶. Taken together, Rac1 activates PAK and its following effects on cytoskeleton remodeling, and Rac1 regulated NADPH oxidase activity is critical oxidative stress and producing hypertrophy.

Atrial structural remodeling was also observed recently¹⁷¹. Along those structural remodeling, functional alterations concerning left atrial EC-coupling on cellular level were also observed, including T-tubule loss/reorganizations, decreased Ca²⁺ transient amplitude and decreased SERCA activity, while the SR Ca²⁺ content and RyR distribution remained normal¹²¹. These data indicate that the EC-coupling is defective in RacET left myocytes. However, no functional analysis

methodology regarding spatiotemporal EC-coupling is available. Here our pixel-wise fitting CICR analysis and subsequent membrane-CICR coupling analysis have characterized those alterations (figure 3.37).

Our reconstructed Ca^{2+} transient precisely resembled the “true” Ca^{2+} signal that laid behind noise. Especially during the time period of Ca^{2+} release, the atrial myocytes from FVB/N mice showed a clear Ca^{2+} release pattern across the cell, while the RacET cell exhibited only few fast Ca^{2+} increase sites in the interior regions (figure 3.37Ad). Pseudo-3D overlay of the Ca^{2+} release $1/\tau$ with membrane staining confirmed the notion that CICR-membrane coupling in RacET left atrial myocytes was greatly corrupted (figure 3.37B). Subsequent CICR-membrane coupling analysis resulted in a much lower coupling coefficient from the RacET mice than that of the WT mice (0.14 vs. 0.21, see table 3.3), which supported the conclusion that constitutively active Rac1 proteins impaired the cardiac EC-coupling.

Since the LTCC current density and the SR Ca^{2+} load were not changed¹²¹ for RacET left atrial cells, while the global Ca^{2+} transient amplitude was decreased by 30%, there must be a coupling failure between LTCC and RyR. The results from functional membrane-CICR coupling analysis supported our deduction. I conclude that the mechanism maintaining T-tubule structure, either its scaffolding backbone or its biogenesis, has been altered by the constitutively active Rac1. Further effort could focus on the T-tubule related proteins, such as ankyrin⁴⁸, spectrin¹⁰³ or BIN1⁸⁶, and their relationship to Rac1.

4.3.5 Case study: dynamics of ventricular Ca^{2+} handling

In a healthy cardiomyocyte, under normal circumstances and electrical simulation, the contraction and the underlying systolic Ca^{2+} transient are consistent from beat to beat. In contrast, in arrhythmias and ventricular fibrillation, this balance is broken^{223,235}. Among Ca^{2+} release dysfunctions, Ca^{2+} alternans, a beat-to-beat alternation in intracellular Ca^{2+} transients, is a key factor promoting T-wave alternans and pulsus alternans in the genesis of electromechanical alternans¹³.

Several mechanisms have been implicated in these Ca^{2+} cycling disturbances and considered to contribute to the Ca^{2+} alternans, such as low Ca^{2+} influx via LTCC¹²⁰, slowed SR Ca^{2+} pump⁴⁹, slow RyR restitution¹⁶¹. Evidence about the role of RyR in the Ca^{2+} alternans is still controversial, Diza et al. reported that the SR Ca^{2+} content fluctuation was the key to Ca^{2+} alternans⁵², while Picht et al. gave an opposite evidence and concluded that Ca^{2+} alternans does not rely on SR Ca^{2+} content¹⁶¹. All those evidences draw the focus of Ca^{2+} alternans to the role of RyR in the CICR process. However, so far there is no direct evidence regarding the behavior of RyR in such abnormal circumstance. Here I recorded Ca^{2+} dynamics with high spatiotemporal resolution

and analyzed the data with the pixel-wise fitting approach to evaluate the RyR behavior under these circumstances: i) Ca^{2+} release under normal conditions; ii) Ca^{2+} release upon stimulation acceleration; and iii) Ca^{2+} release during Ca^{2+} alternans development.

When cardiomyocytes were electrically stimulated and reached a steady state, the Ca^{2+} release sites (see $1/\tau$ images in figure 3.38A and 3.38C) were evenly distributed, such that the pixel-wise amplitudes of Ca^{2+} transients were homogeneous throughout the entire myocyte except the nuclei (see amplitude images in figure 3.38A and 3.38C). This pattern was also very stable with high correlation (2D correlation coefficient is above 0.8) between successive transients (figure 3.38D). No local or microscopic alternating pixels was apparent.

Upon increasing the stimulation frequency, the diastolic Ca^{2+} concentration increased with stimulation frequency, while the systolic Ca^{2+} concentration just increased slightly. The resultant amplitude of Ca^{2+} transients decreased (figure 3.39A, top panel). These results are compatible with previous report⁵⁵. Local Ca^{2+} transients almost resembled the global transients, with microscopic Ca^{2+} alternans clearly visible at high frequency (low panel in figure 3.39A), which was not observed at low stimulation frequency (1 Hz) and in global transients from all the tested frequencies.

Subsequent pixel-wise fitting confirmed the increase of the diastolic Ca^{2+} and decreased amplitudes, while the global signal was in good agreement with the local signal (figure 3.39B). However, the fitted Ca^{2+} increase velocity (τ values) from global and pixel transients showed opposite trends. The local Ca^{2+} increase τ value was decreased, that is, the local Ca^{2+} increase velocity was increased ($1/\tau$ decreasing); however, this kind of locally acceleration did not boost, but decrease the global Ca^{2+} increase velocity. These data implied that the activity of the individual RyR clusters (all the RyR in the same pixel) might be increased to comply with the higher beating frequency, however, the concordance of all these RyR clusters (pixels) was decreased, such that the global Ca^{2+} increase velocity was not increased, but decreased. One possible reason for this phenomena is that the coupling between the junctional SR and the longitudinal SR¹⁷⁷ might be altered at high pacing rates, such that the synchrony between RyRs is reduced, and the global Ca^{2+} increase velocity was eventually decreased. Additionally, RyRs are physically and functionally coupled with each other^{132,149}. Increased diastolic Ca^{2+} concentration might also contribute to the instability of the coupling between RyRs.

With the speculation mentioned above, it is interesting to know what will happen if those microscopic Ca^{2+} alternans advance one step further. In the beginning of alternans development, microscopic Ca^{2+} alternans was observed (ROI3 in figure 3.40B), but less significant in the Ca^{2+} transients from large area (ROI1 and ROI2 in figure 3.40B), and even not in global transients. The

amplitude of the microscopic alternans was very small, and the fitted $1/\tau$ values were still homogeneous (figure 3.40A, left panel), when compared with a cell without any microscopic alternans (figure 3.38A). After a long time (15 min) of pacing at the high frequency (4 Hz at room temperature), macroscopic Ca^{2+} alternans developed (figure 3.40, right panel). The amplitude image and Ca^{2+} release τ image demonstrated clear alternating patterns, but surprisingly in a opposite direction. Furthermore, the Ca^{2+} release τ value changed from below 10 ms to 100 ms. The reduced Ca^{2+} increase implies a decreased RyR activity and a longer Ca^{2+} increase time. This will eventually prolong the Ca^{2+} transient duration, thus there will be no enough time for the RyRs to recover. When the next pulse comes, the Ca^{2+} release via RyRs will be reduced or aborted, and the Ca^{2+} amplitude will be small. Without the Ca^{2+} release from SR, the Ca^{2+} increase will be very fast, since the Ca^{2+} influx via LTCC is very fast. Ultimately the amplitude and the Ca^{2+} increase alternated in an opposite pattern. In the microscopic alternans, the coupling of the RyRs on the junctional SR and those on the longitudinal SR might be just altered slightly and locally. As the alternans developed, the coupling was probably further disrupted, such that all these sites of small microscopic alternans are connected and synchronized, which ultimately results in a global Ca^{2+} alternans.

4.3.6 Summary and perspectives

The pixel-wise fitting approach introduced here for the first time allied comprehensive analysis of subcellular EC-coupling in fast 2D confocal data without compromising spatial and/or temporal resolution. Our novel approach describes the entire time course of microscopic Ca^{2+} transients on a pixel-by-pixel basis and allows reconstruction of the Ca^{2+} signals at any given temporal resolution. The two examples given and discussed revealed novel aspects of cardiac EC-coupling in both a transgenic model and an arrhythmic model. In the transgenic animal case, the localization of Ca^{2+} release sites was important and in an experimental conditions fostered cardiac alternans. In the later case, the approach revealed microscopic alternans preceding macroscopic alternans.

Based on this approach additional parameters can be extracted that have not been considered here, such as Ca^{2+} removal processes.

For the future I believe that the application of this approach will foster the analysis of fast 2D confocal data and will aid the researcher to increase the understanding of spatial aspects of cardiac Ca^{2+} handling and EC-coupling in physiological but especially in disease situations.

References

1. Abbott GW, Sesti F, Splawski I, Buck ME, Lehmann MH, Timothy KW, Keating MT, Goldstein SA (1999) MiRP1 forms I_{Kr} potassium channels with hERG and is associated with cardiac arrhythmia. *Cell* 97(2):175–187
2. Adam O, Frost G, Custodis F, Sussman MA, Schäfers HJ, Böhm M, Laufs U (2007) Role of Rac1 GTPase activation in atrial fibrillation. *J Am Coll Cardiol* 50(4):359–367
3. Aistrup GL, Kelly JE, Kapur S, Kowalczyk M, Sysman-Wolpin I, Kadish AH, Wasserstrom JA (2006) Pacing-induced heterogeneities in intracellular Ca^{2+} signaling, cardiac alternans, and ventricular arrhythmias in intact rat heart. *Circ Res* 99(7):e65–e73
4. Anderson M (2004) Calmodulin Kinase and L-Type Calcium Channels: A Recipe for Arrhythmias? *Trends in Cardiovascular Medicine* 14(4):152–161
5. Arrigoni C, Crivori P (2007) Assessment of QT liabilities in drug development. *Cell Biol Toxicol* 23(1):1–13
6. Ataka K, Pieribone VA (2002) A genetically targetable fluorescent probe of channel gating with rapid kinetics. *Biophys J* 82(1 Pt 1):509–516
7. Babu GJ, Bhupathy P, Petrashevskaya NN, Wang H, Raman S, Wheeler D, Jagatheesan G, Wieczorek D, Schwartz A, Janssen PML, Ziolo MT, Periasamy M (2006) Targeted overexpression of sarcolipin in the mouse heart decreases sarcoplasmic reticulum calcium transport and cardiac contractility. *J Biol Chem* 281(7):3972–3979
8. Bagnato P, Barone V, Giacomello E, Rossi D, Sorrentino V (2003) Binding of an ankyrin-1 isoform to obscurin suggests a molecular link between the sarcoplasmic reticulum and myofibrils in striated muscles. *J Cell Biol* 160(2):245–253
9. Baker LC, Wolk R, Choi BR, Watkins S, Plan P, Shah A, Salama G (2004) Effects of mechanical uncouplers, diacetyl monoxime, and cytochalasin-D on the electrophysiology of perfused mouse hearts. *Am J Physiol Heart Circ Physiol* 287(4):H1771–H1779

10. Balijepalli RC, Lokuta AJ, Maertz NA, Buck JM, Haworth RA, Valdivia HH, Kamp TJ (2003) Depletion of T-tubules and specific subcellular changes in sarcolemmal proteins in tachycardia-induced heart failure. *Cardiovasc Res* 59(1):67–77
11. Balshaw DM, Xu L, Yamaguchi N, Pasek DA, Meissner G (2001) Calmodulin binding and inhibition of cardiac muscle calcium release channel (ryanodine receptor). *J Biol Chem* 276(23):20144–20153
12. Banyasz T, Lozinskiy I, Payne CE, Edelmann S, Norton B, Chen B, Chen-Izu Y, Izu LT, Balke CW (2008) Transformation of adult rat cardiac myocytes in primary culture. *Exp Physiol* 93(3):370–382
13. Bao M, Zhang J, Huang C, Jiang H, Liu J, Zhao D (2007) Abnormal intracellular calcium handling underlying T-wave alternans and its hysteresis. *Cardiology* 108(3):147–156
14. Bers DM (2002) Cardiac excitation-contraction coupling. *Nature* 415(6868):198–205
15. Bers DM (2002) Excitation-Contraction Coupling and Cardiac Contractile Force. 63-64, Kluwer Academic Publishers
16. Bers DM (2002) Excitation-Contraction Coupling and Cardiac Contractile Force. 165-166, Kluwer Academic Publishers
17. Bers DM (2002) Excitation-Contraction Coupling and Cardiac Contractile Force. 41-46, Kluwer Academic Publishers
18. Bers DM (2008) Calcium cycling and signaling in cardiac myocytes. *Annu Rev Physiol* 70:23–49
19. Betzenhauser MJ, Marks AR (2010) Ryanodine receptor channelopathies. *Pflugers Arch* 460(2):467–480
20. Biermann M, Rubart M, Moreno A, Wu J, Josiah-Durant A, Zipes DP (1998) Differential effects of Cytochalasin D and 2,3-butanedione monoxime on isometric twitch force and transmembrane action potential in isolated ventricular muscle: implications for optical measurements of cardiac repolarization. *J Cardiovasc Electrophysiol* 9(12):1348–1357
21. Blatter LA, Kockskämper J, Sheehan KA, Zima AV, Hüser J, Lipsius SL (2003) Local calcium gradients during excitation-contraction coupling and alternans in atrial myocytes. *J Physiol* 546(Pt 1):19–31

22. Bodi I, Mikala G, Koch SE, Akhter SA, Schwartz A (2005) The L-type calcium channel in the heart: the beat goes on. *J Clin Invest* 115(12):3306–3317
23. Bootman MD, Higazi DR, Coombes S, Roderick HL (2006) Calcium signalling during excitation-contraction coupling in mammalian atrial myocytes. *J Cell Sci* 119(Pt 19):3915–3925
24. Bosco EE, Mulloy JC, Zheng Y (2009) Rac1 GTPase: a "Rac" of all trades. *Cell Mol Life Sci* 66(3):370–374
25. Bowers SLK, Banerjee I, Baudino TA (2010) The extracellular matrix: at the center of it all. *J Mol Cell Cardiol* 48(3):474–482
26. Brenner SL, Korn ED (1979) Substoichiometric concentrations of Cytochalasin D inhibit actin polymerization. Additional evidence for an F-actin treadmill. *J Biol Chem* 254(20):9982–9985
27. Brette F, Orchard C (2003) T-tubule function in mammalian cardiac myocytes. *Circ Res* 92(11):1182–1192
28. Briggs MW, Sacks DB (2003) IQGAP proteins are integral components of cytoskeletal regulation. *EMBO Rep* 4(6):571–574
29. Brown JH, Re DPD, Sussman MA (2006) The Rac and Rho hall of fame: a decade of hypertrophic signaling hits. *Circ Res* 98(6):730–742
30. Brown SS, Spudich JA (1981) Mechanism of action of cytochalasin: evidence that it binds to actin filament ends. *J Cell Biol* 88(3):487–491
31. Brugada R, Brugada P, Brugada J (2006) Electrocardiogram interpretation and class I blocker challenge in Brugada syndrome. *J Electrocardiol* 39(4 Suppl):S115–S118
32. Bu G, Adams H, Berbari EJ, Rubart M (2009) Uniform action potential repolarization within the sarcolemma of in situ ventricular cardiomyocytes. *Biophys J* 96(6):2532–2546
33. Bullen A, Saggau P (1999) High-speed, random-access fluorescence microscopy: II. Fast quantitative measurements with voltage-sensitive dyes. *Biophys J* 76(4):2272–2287
34. Calaghan SC, Guennec JYL, White E (2004) Cytoskeletal modulation of electrical and mechanical activity in cardiac myocytes. *Prog Biophys Mol Biol* 84(1):29–59

35. Calaghan SC, White E, Bedut S, Guennec JYL (2000) Cytochalasin D reduces Ca^{2+} sensitivity and maximum tension via interactions with myofilaments in skinned rat cardiac myocytes. *J Physiol* 529 Pt 2:405–411
36. Cannell MB, Crossman DJ, Soeller C (2006) Effect of changes in action potential spike configuration, junctional sarcoplasmic reticulum micro-architecture and altered t-tubule structure in human heart failure. *J Muscle Res Cell Motil* 27(5-7):297–306
37. Casella JF, Flanagan MD, Lin S (1981) Cytochalasin D inhibits actin polymerization and induces depolymerization of actin filaments formed during platelet shape change. *Nature* 293(5830):302–305
38. Chen Q, Kirsch GE, Zhang D, Brugada R, Brugada J, Brugada P, Potenza D, Moya A, Borggrefe M, Breithardt G, Ortiz-Lopez R, Wang Z, Antzelevitch C, O'Brien RE, Schulze-Bahr E, Keating MT, Towbin JA, Wang Q (1998) Genetic basis and molecular mechanism for idiopathic ventricular fibrillation. *Nature* 392(6673):293–296
39. Chlopčíková S, Psotová J, Miketová P (2001) Neonatal rat cardiomyocytes - a model for the study of morphological, biochemical and electrophysiological characteristics of the heart. *Biomed Pap Med Fac Univ Palacky Olomouc Czech Repub* 145(2):49–55
40. Chung KY, Kang M, Walker JW (2008) Contractile regulation by overexpressed ETA requires intact T tubules in adult rat ventricular myocytes. *Am J Physiol Heart Circ Physiol* 294(5):H2391–H2399
41. Clapham DE (2007) Calcium signaling. *Cell* 131(6):1047–1058
42. Clark KA, McElhinny AS, Beckerle MC, Gregorio CC (2002) Striated muscle cytoarchitecture: an intricate web of form and function. *Annu Rev Cell Dev Biol* 18:637–706
43. Cleutjens JPM, Creemers EEJM (2002) Integration of concepts: cardiac extracellular matrix remodeling after myocardial infarction. *J Card Fail* 8(6 Suppl):S344–S348
44. Coates C, Fowler B, Holst G (2009), Scientific CMOS technology - A high-performance imaging breakthrough. F. I. P. A. Andor Technology PLC, Ed. pp. 1-14 (www.scmos.com).
45. Committee for proprietary medicinal products (1997) Points to consider: the assessment for the potential for QT prolongation by noncardiovascular medicinal products. *European Agency for the Evaluation of Medicinal Products* 986:96

46. Cordeiro JM, Malone JE, Diego JMD, Scornik FS, Aistrup GL, Antzelevitch C, Wasserstrom JA (2007) Cellular and subcellular alternans in the canine left ventricle. *Am J Physiol Heart Circ Physiol* 293(6):H3506–H3516
47. Cormen TH, Leiserson CE, Rivest RL, Stein C (2009) Introduction to algorithms. 3rd edition, The MIT Press, Cambridge, Massachusetts, London, England
48. Cunha SR, Mohler PJ (2006) Cardiac ankyrins: Essential components for development and maintenance of excitable membrane domains in heart. *Cardiovasc Res* 71(1):22–29
49. Cutler MJ, Wan X, Laurita KR, Hajjar RJ, Rosenbaum DS (2009) Targeted SERCA2a gene expression identifies molecular mechanism and therapeutic target for arrhythmogenic cardiac alternans. *Circ Arrhythm Electrophysiol* 2(6):686–694
50. Díaz ME, Eisner DA, O'Neill SC (2002) Depressed ryanodine receptor activity increases variability and duration of the systolic Ca^{2+} transient in rat ventricular myocytes. *Circ Res* 91(7):585–593
51. Díaz ME, Graham HK, Trafford AW (2004) Enhanced sarcolemmal Ca^{2+} efflux reduces sarcoplasmic reticulum Ca^{2+} content and systolic Ca^{2+} in cardiac hypertrophy. *Cardiovasc Res* 62(3):538–547
52. Díaz ME, O'Neill SC, Eisner DA (2004) Sarcoplasmic reticulum calcium content fluctuation is the key to cardiac alternans. *Circ Res* 94(5):650–656
53. del Monte F, Harding SE, Schmidt U, Matsui T, Kang ZB, Dec GW, Gwathmey JK, Rosenzweig A, Hajjar RJ (1999) Restoration of contractile function in isolated cardiomyocytes from failing human hearts by gene transfer of SERCA2a. *Circulation* 100(23):2308–2311
54. Delpón E, Cordeiro JM, Núñez L, Thomsen PEB, Guerchicoff A, Pollevick GD, Wu Y, Kanters JK, Larsen CT, Hofman-Bang J, Burashnikov E, Christiansen M, Antzelevitch C (2008) Functional effects of KCNE3 mutation and its role in the development of Brugada syndrome. *Circ Arrhythm Electrophysiol* 1(3):209–218
55. Dibb KM, Eisner DA, Trafford AW (2007) Regulation of systolic $[\text{Ca}^{2+}]_i$ and cellular Ca^{2+} flux balance in rat ventricular myocytes by SR Ca^{2+} , L-type Ca^{2+} current and diastolic $[\text{Ca}^{2+}]_i$. *J Physiol* 585(Pt 2):579–592
56. Dumaine R, Wang Q, Keating MT, Hartmann HA, Schwartz PJ, Brown AM, Kirsch GE (1996) Multiple mechanisms of Na^+ channel-linked long-QT syndrome. *Circ Res* 78(5):916–924

57. Dumitrescu C, Narayan P, Efimov IR, Cheng Y, Radin MJ, McCune SA, Altschuld RA (2002) Mechanical alternans and restitution in failing SHHF rat left ventricles. *Am J Physiol Heart Circ Physiol* 282(4):H1320–H1326
58. Eblen ST, Slack JK, Weber MJ, Catling AD (2002) Rac-PAK signaling stimulates extracellular signal-regulated kinase (ERK) activation by regulating formation of MEK1-ERK complexes. *Mol Cell Biol* 22(17):6023–6033
59. Estes N 3rd, Michaud G, Zipes DP, El-Sherif N, Venditti FJ, Rosenbaum DS, Albrecht P, Wang PJ, Cohen RJ (1997) Electrical alternans during rest and exercise as predictors of vulnerability to ventricular arrhythmias. *Am J Cardiol* 80(10):1314–1318
60. Fecik RA, Frank KE, Gentry EJ, Menon SR, Mitscher LA, Telikepalli H (1998) The search for orally active medications through combinatorial chemistry. *Med Res Rev* 18(3):149–185
61. Flanagan MD, Lin S (1980) Cytochalasins block actin filament elongation by binding to high affinity sites associated with F-actin. *J Biol Chem* 255(3):835–838
62. Fromherz P, Hübener G, Kuhn B, Hinner MJ (2008) ANNINE-6plus, a voltage-sensitive dye with good solubility, strong membrane binding and high sensitivity. *Eur Biophys J* 37(4):509–514
63. Garbino A, van Oort RJ, Dixit SS, Landstrom AP, Ackerman MJ, Wehrens XHT (2009) Molecular evolution of the junctophilin gene family. *Physiol Genomics* 37(3):175–186
64. Gautel M (2011) The sarcomeric cytoskeleton: who picks up the strain? *Curr Opin Cell Biol* 23(1):39–46
65. Goldhaber JI, Xie LH, Duong T, Motter C, Khuu K, Weiss JN (2005) Action potential duration restitution and alternans in rabbit ventricular myocytes: the key role of intracellular calcium cycling. *Circ Res* 96(4):459–466
66. Grandy SA, Trépanier-Boulay V, Fiset C (2007) Postnatal development has a marked effect on ventricular repolarization in mice. *Am J Physiol Heart Circ Physiol* 293(4):H2168–H2177
67. Grant AO (2009) Cardiac ion channels. *Circ Arrhythm Electrophysiol* 2(2):185–194
68. Granzier HL, Labeit S (2004) The giant protein titin: a major player in myocardial mechanics, signaling, and disease. *Circ Res* 94(3):284–295
69. Greenberg DS, Houweling AR, Kerr JND (2008) Population imaging of ongoing neuronal activity in the visual cortex of awake rats. *Nat Neurosci* 11(7):749–751

70. Greenstein JL, Wu R, Po S, Tomaselli GF, Winslow RL (2000) Role of the calcium-independent transient outward current $I_{(to1)}$ in shaping action potential morphology and duration. *Circ Res* 87(11):1026–1033
71. Gregg D, Rauscher FM, Goldschmidt-Clermont PJ (2003) Rac regulates cardiovascular superoxide through diverse molecular interactions: more than a binary GTP switch. *Am J Physiol Cell Physiol* 285(4):C723–C734
72. Gregorio CC, Weber A, Bondad M, Pennise CR, Fowler VM (1995) Requirement of pointed-end capping by tropomodulin to maintain actin filament length in embryonic chick cardiac myocytes. *Nature* 377(6544):83–86
73. Grewe BF, Langer D, Kasper H, Kampa BM, Helmchen F (2010) High-speed in vivo calcium imaging reveals neuronal network activity with near-millisecond precision. *Nat Methods* 7(5):399–405
74. Guerrero G, Siegel MS, Roska B, Loots E, Isacoff EY (2002) Tuning FlaSh: redesign of the dynamics, voltage range, and color of the genetically encoded optical sensor of membrane potential. *Biophys J* 83(6):3607–3618
75. Guo W, Kamiya K, Liu W, Toyama J (1997) Developmental changes of the ultrarapid delayed rectifier K^+ current in rat ventricular myocytes. *Pflugers Arch* 433(4):442–445
76. Guo W, Kamiya K, Toyama J (1996) Modulated expression of transient outward current in cultured neonatal rat ventricular myocytes: comparison with development in situ. *Cardiovasc Res* 32(3):524–533
77. Hammer K, Ruppenthal S, Viero C, Scholz A, Edelmann L, Kaestner L, Lipp P (2010) Remodelling of Ca^{2+} handling organelles in adult rat ventricular myocytes during long term culture. *J Mol Cell Cardiol* 49(3):427–437
78. Hardy M, Lawrence C, Standen N, Rodrigo G (2006) Can optical recordings of membrane potential be used to screen for drug-induced action potential prolongation in single cardiac myocytes? *Journal of Pharmacological and Toxicological Methods* 54(2):173–182
79. Hardy M, Pollard C, Small B, Bridgland-Taylor M, Woods A, Valentin JP, Abi-Gerges N (2009) Validation of a voltage-sensitive dye (di-4-ANEPPS)-based method for assessing drug-induced delayed repolarisation in beagle dog left ventricular midmyocardial myocytes. *J Pharmacol Toxicol Methods* 60(1):94–106

80. Hashemi SM, Hund TJ, Mohler PJ (2009) Cardiac ankyrins in health and disease. *J Mol Cell Cardiol* 47(2):203–209
81. Haverkamp W, Breithardt G, Camm AJ, Janse MJ, Rosen MR, Antzelevitch C, Escande D, Franz M, Malik M, Moss A, Shah R (2000) The potential for QT prolongation and pro-arrhythmia by non-anti-arrhythmic drugs: clinical and regulatory implications. Report on a Policy Conference of the European Society of Cardiology. *Cardiovasc Res* 47(2):219–233
82. He J, Conklin MW, Foell JD, Wolff MR, Haworth RA, Coronado R, Kamp TJ (2001) Reduction in density of transverse tubules and L-type Ca^{2+} channels in canine tachycardia-induced heart failure. *Cardiovasc Res* 49(2):298–307
83. Heinzel FR, Bito V, Biesmans L, Wu M, Detre E, von Wegner F, Claus P, Dymarkowski S, Maes F, Bogaert J, Rademakers F, D'hooge J, Sipido K (2008) Remodeling of T-tubules and reduced synchrony of Ca^{2+} release in myocytes from chronically ischemic myocardium. *Circ Res* 102(3):338–346
84. Heinzel FR, Macquaide N, Biesmans L, Sipido K (2011) Dyssynchrony of Ca^{2+} release from the sarcoplasmic reticulum as subcellular mechanism of cardiac contractile dysfunction. *J Mol Cell Cardiol* 50(3):390–400
85. Hirota M, Ohtani H, Hanada E, Sato H, Kotaki H, Uemura H, Nakaya H, Iga T (2000) Influence of extracellular K^{+} concentrations on quinidine-induced K^{+} current inhibition in rat ventricular myocytes. *J Pharm Pharmacol* 52(1):99–105
86. Hong TT, Smyth JW, Gao D, Chu KY, Vogan JM, Fong TS, Jensen BC, Colecraft HM, Shaw RM (2010) BIN1 localizes the L-type calcium channel to cardiac T-tubules. *PLoS Biol* 8(2):e1000312
87. Honig MG, Hume RI (1989) Dil and diO: versatile fluorescent dyes for neuronal labelling and pathway tracing. *Trends Neurosci* 12(9):333–5, 340–1
88. Hopitzan AA, Baines AJ, Kordeli E (2006) Molecular evolution of ankyrin: gain of function in vertebrates by acquisition of an obscurin/titin-binding-related domain. *Mol Biol Evol* 23(1):46–55
89. Hoshijima M (2006) Mechanical stress-strain sensors embedded in cardiac cytoskeleton: Z disk, titin, and associated structures. *Am J Physiol Heart Circ Physiol* 290(4):H1313–H1325

90. Howarth FC, Boyett MR, White E (1998) Rapid effects of cytochalasin-D on contraction and intracellular calcium in single rat ventricular myocytes. *Pflugers Arch* 436(5):804–806
91. Hüser J, Lipp P, Niggli E (1996) Confocal microscopic detection of potential-sensitive dyes used to reveal loss of voltage control during patch-clamp experiments. *Pflugers Arch* 433(1-2):194–199
92. Hüser J, Lipsius SL, Blatter LA (1996) Calcium gradients during excitation-contraction coupling in cat atrial myocytes. *J Physiol* 494 (Pt 3):641–651
93. Ibrahim M, Gorelik J, Yacoub MH, Terracciano CM (2011) The structure and function of cardiac t-tubules in health and disease. *Proc Biol Sci* 278(1719):2714–2723
94. Imahashi K, Pott C, Goldhaber JI, Steenbergen C, Philipson KD, Murphy E (2005) Cardiac-specific ablation of the Na^{2+} - Ca^{2+} exchanger confers protection against ischemia/reperfusion injury. *Circ Res* 97(9):916–921
95. Investigators CAST (1989) Preliminary report: effect of encainide and flecainide on mortality in a randomized trial of arrhythmia suppression after myocardial infarction. The Cardiac Arrhythmia Suppression Trial (CAST) Investigators. *N Engl J Med* 321(6):406–412
96. Jaffe AB, Hall A (2005) Rho GTPases: biochemistry and biology. *Annu Rev Cell Dev Biol* 21:247–269
97. James R Broach JT (1996) High-throughput screening for drug discovery. *Nature* 384 (Supplementray):14–16
98. Jorgensen PL, Hakansson KO, Karlsh SJD (2003) Structure and mechanism of Na,K-ATPase: functional sites and their interactions. *Annu Rev Physiol* 65:817–849
99. Jost N, Papp JG, Varró A (2007) Slow delayed rectifier potassium current (I_{Ks}) and the repolarization reserve. *Ann Noninvasive Electrocardiol* 12(1):64–78
100. Kaestner L, Scholz A, Hammer K, Vecerdea A, Ruppenthal S, Lipp P (2009) Isolation and genetic manipulation of adult cardiac myocytes for confocal imaging. *J Vis Exp* 31(31):31
101. Kamogawa Y, Biro S, Maeda M, Setoguchi M, Hirakawa T, Yoshida H, Tei C (2001) Dystrophin-deficient myocardium is vulnerable to pressure overload in vivo. *Cardiovasc Res* 50(3):509–515

102. Kääh S, Dixon J, Duc J, Ashen D, Näbauer M, Beuckelmann DJ, Steinbeck G, McKinnon D, Tomaselli GF (1998) Molecular basis of transient outward potassium current downregulation in human heart failure: a decrease in Kv4.3 mRNA correlates with a reduction in current density. *Circulation* 98(14):1383–1393
103. Kee AJ, Gunning PW, Hardeman EC (2009) Diverse roles of the actin cytoskeleton in striated muscle. *J Muscle Res Cell Motil* 30(5-6):187–197
104. Kenyon JL, Gibbons WR (1979) 4-Aminopyridine and the early outward current of sheep cardiac Purkinje fibers. *J Gen Physiol* 73(2):139–157
105. Kilborn MJ, Fedida D (1990) A study of the developmental changes in outward currents of rat ventricular myocytes. *J Physiol* 430:37–60
106. Klymchenko AS, Duportail G, Mély Y, Demchenko AP (2003) Ultrasensitive two-color fluorescence probes for dipole potential in phospholipid membranes. *Proc Natl Acad Sci U S A* 100(20):11219–11224
107. Knisley SB, Justice RK, Kong W, Johnson PL (2000) Ratiometry of transmembrane voltage-sensitive fluorescent dye emission in hearts. *Am J Physiol Heart Circ Physiol* 279(3):H1421–H1433
108. Knöll R, Hoshijima M, Hoffman HM, Person V, Lorenzen-Schmidt I, Bang ML, Hayashi T, Shiga N, Yasukawa H, Schaper W, McKenna W, Yokoyama M, Schork NJ, Omens JH, McCulloch AD, Kimura A, Gregorio CC, Poller W, Schaper J, Schultheiss HP, Chien KR (2002) The cardiac mechanical stretch sensor machinery involves a Z disc complex that is defective in a subset of human dilated cardiomyopathy. *Cell* 111(7):943–955
109. Knollmann BC, Chopra N, Hlaing T, Akin B, Yang T, Etensohn K, Knollmann BEC, Horton KD, Weissman NJ, Holinstat I, Zhang W, Roden DM, Jones LR, Franzini-Armstrong C, Pfeifer K (2006) Casq2 deletion causes sarcoplasmic reticulum volume increase, premature Ca²⁺ release, and catecholaminergic polymorphic ventricular tachycardia. *J Clin Invest* 116(9):2510–2520
110. Komazaki S, Nishi M, Takeshima H (2003) Abnormal junctional membrane structures in cardiac myocytes expressing ectopic junctophilin type 1. *FEBS Lett* 542(1-3):69–73
111. Kontogianni-Konstantopoulos A, Bloch RJ (2005) Obscurin: a multitasking muscle giant. *J Muscle Res Cell Motil* 26(6-8):419–426

112. Krishna A, Sun L, Valderrábano M, Palade PT, Clark JW (2010) Modeling CICR in rat ventricular myocytes: voltage clamp studies. *Theor Biol Med Model* 7:43
113. Kuhn B, Fromherz P, Denk W (2004) High sensitivity of Stark-shift voltage-sensing dyes by one- or two-photon excitation near the red spectral edge. *Biophys J* 87(1):631–639
114. Kwan AC, Dietz SB, Zhong G, Harris-Warrick RM, Webb WW (2010) Spatiotemporal dynamics of rhythmic spinal interneurons measured with two-photon calcium imaging and coherence analysis. *J Neurophysiol* 104(6):3323–3333
115. Lacampagne A, Ward CW, Klein MG, Schneider MF (1999) Time course of individual Ca^{2+} sparks in frog skeletal muscle recorded at high time resolution. *J Gen Physiol* 113(2):187–198
116. Lagarias JC, Reeds JA, Wright MH, Wright PE (1998) Convergence Properties of the Nelder-Mead Simplex Method in Low Dimensions. *SIAM Journal of Optimization* 9:112–147
117. Lanner JT, Georgiou DK, Joshi AD, Hamilton SL (2010) Ryanodine receptors: structure, expression, molecular details, and function in calcium release. *Cold Spring Harb Perspect Biol* 2(11):a003996
118. Laurita KR, Rosenbaum DS (2008) Cellular mechanisms of arrhythmogenic cardiac alternans. *Prog Biophys Mol Biol* 97(2-3):332–347
119. Leach RN, Desai JC, Orchard CH (2005) Effect of cytoskeleton disruptors on L-type Ca channel distribution in rat ventricular myocytes. *Cell Calcium* 38(5):515–526
120. Li Y, Díaz ME, Eisner DA, O'Neill S (2009) The effects of membrane potential, SR Ca^{2+} content and RyR responsiveness on systolic Ca^{2+} alternans in rat ventricular myocytes. *J Physiol* 587(Pt 6):1283–1292
121. Lipp P, Ruppenthal S, Scholz A, Jung J, Kaestner L (2011) Visualisation of the cytoskeleton in cardiac myocytes from a model of atrial fibrillation. In: *Biophysical Society 55th Annual Meeting*
122. Louch WE, Bito V, Heinzel FR, Macianskiene R, Vanhaecke J, Flameng W, Mubagwa K, Sipido KR (2004) Reduced synchrony of Ca^{2+} release with loss of T-tubules: a comparison to Ca^{2+} release in human failing cardiomyocytes. *Cardiovascular Research* 62(1):63–73

123. Louch WE, Mørk HK, Sexton J, Strømme TA, Laake P, Sjaastad I, Sejersted OM (2006) T-tubule disorganization and reduced synchrony of Ca^{2+} release in murine cardiomyocytes following myocardial infarction. *J Physiol* 574(Pt 2):519–533
124. Lu H, Fedak PWM, Dai X, Du C, Zhou YQ, Henkelman M, Mongroo PS, Lau A, Yamabi H, Hinek A, Husain M, Hannigan G, Coles JG (2006) Integrin-linked kinase expression is elevated in human cardiac hypertrophy and induces hypertrophy in transgenic mice. *Circulation* 114(21):2271–2279
125. Luisier F, Blu T, Unser M (2011) Image denoising in mixed Poisson-Gaussian noise. *IEEE Trans Image Process* 20(3):696–708
126. Lyon AR, MacLeod KT, Zhang Y, Garcia E, Kanda GK, Lab MJ, Korchev YE, Harding SE, Gorelik J (2009) Loss of T-tubules and other changes to surface topography in ventricular myocytes from failing human and rat heart. *Proc Natl Acad Sci U S A* 106(16):6854–6859
127. Mackenzie L, Bootman MD, Berridge MJ, Lipp P (2001) Predetermined recruitment of calcium release sites underlies excitation-contraction coupling in rat atrial myocytes. *J Physiol* 530(Pt 3):417–429
128. Mackenzie L, Bootman MD, Laine M, Berridge MJ, Thuring J, Holmes A, Li WH, Lipp P (2002) The role of inositol 1,4,5-trisphosphate receptors in Ca^{2+} signalling and the generation of arrhythmias in rat atrial myocytes. *J Physiol* 541(Pt 2):395–409
129. MacLennan DH, Kranias EG (2003) Phospholamban: a crucial regulator of cardiac contractility. *Nat Rev Mol Cell Biol* 4(7):566–577
130. Mader SS (2004) *Understanding Human Anatomy & Physiology* (5th Ed.). The McGraw-Hill Companies
131. Marban E, Robinson SW, Wier WG (1986) Mechanisms of arrhythmogenic delayed and early afterdepolarizations in ferret ventricular muscle. *J Clin Invest* 78(5):1185–1192
132. Marx SO, Gaburjakova J, Gaburjakova M, Henrikson C, Ondrias K, Marks AR (2001) Coupled gating between cardiac calcium release channels (ryanodine receptors). *Circ Res* 88(11):1151–1158
133. The MathWorks, Inc. (2009) fminsearch - Find minimum of unconstrained multivariable function using derivative-free method. Matlab 2009a edition

134. Mazzanti M, Assandri R, Ferroni A, DiFrancesco D (1996) Cytoskeletal control of rectification and expression of four substates in cardiac inward rectifier K⁺ channels. *FASEB J* 10(2):357–361
135. McCall E, Li L, Satoh H, Shannon TR, Blatter LA, Bers DM (1996) Effects of FK-506 on contraction and Ca²⁺ transients in rat cardiac myocytes. *Circ Res* 79(6):1110–1121
136. McGrath KF, Yuki A, Manaka Y, Tamaki H, Saito K, Takekura H (2009) Morphological characteristics of cardiac calcium release units in animals with metabolic and circulatory disorders. *J Muscle Res Cell Motil* 30(5-6):225–231
137. Messerli JM, Eppenberger-Eberhardt ME, Rutishauser BM, Schwarb P, von Arx P, Koch-Schneidemann S, Eppenberger HM, Perriard JC (1993) Remodelling of cardiomyocyte cytoarchitecture visualized by three-dimensional (3D) confocal microscopy. *Histochemistry* 100(3):193–202
138. Miki H, Yamaguchi H, Suetsugu S, Takenawa T (2000) IRSp53 is an essential intermediate between Rac and WAVE in the regulation of membrane ruffling. *Nature* 408(6813):732–735
139. Mitcheson JS, Hancox JC, Levi AJ (1996) Action potentials, ion channel currents and transverse tubule density in adult rabbit ventricular myocytes maintained for 6 days in cell culture. *Pflugers Arch* 431(6):814–827
140. Mohler PJ, Davis JQ, Bennett V (2005) Ankyrin-B coordinates the Na/K ATPase, Na/Ca exchanger, and InsP3 receptor in a cardiac T-tubule/SR microdomain. *PLoS Biol* 3(12):e423
141. Müller O, Tian Q, Zantl R, Kahl V, Lipp P, Kaestner L (2010) A system for optical high resolution screening of electrical excitable cells. *Cell Calcium* 47(3):224–233
142. Müller W, Windisch H, Tritthart HA (1986) Fluorescent styryl dyes applied as fast optical probes of cardiac action potential. *Eur Biophys J* 14(2):103–111
143. Murata Y, Iwasaki H, Sasaki M, Inaba K, Okamura Y (2005) Phosphoinositide phosphatase activity coupled to an intrinsic voltage sensor. *Nature Cell Biology* 435(7046):1239–1243
144. Muschol M, Dasgupta BR, Salzberg BM (1999) Caffeine interaction with fluorescent calcium indicator dyes. *Biophys J* 77(1):577–586
145. Myles RC, Burton FL, Cobbe SM, Smith GL (2008) The link between repolarisation alternans and ventricular arrhythmia: does the cellular phenomenon extend to the clinical problem? *J Mol Cell Cardiol* 45(1):1–10

146. Nattel S, Carlsson L (2006) Innovative approaches to anti-arrhythmic drug therapy. *Nat Rev Drug Discov* 5(12):1034–1049
147. Niwa N, Nerbonne JM (2010) Molecular determinants of cardiac transient outward potassium current (I_{to}) expression and regulation. *J Mol Cell Cardiol* 48(1):12–25
148. NIWA N, WANG W, SHA Q, MARIONNEAU C, NERBONNE J (2008) Kv4.3 is not required for the generation of functional $I_{to,f}$ channels in adult mouse ventricles. *Journal of Molecular and Cellular Cardiology* 44(1):95–104
149. Ondrias K, Mojzisová A (2002) Coupled gating between individual cardiac ryanodine calcium release channels. *Gen Physiol Biophys* 21(1):73–84
150. Ono K, Iijima T (2010) Cardiac T-type Ca^{2+} channels in the heart. *J Mol Cell Cardiol* 48(1):65–70
151. Orchard C, Brette F (2008) T-tubules and sarcoplasmic reticulum function in cardiac ventricular myocytes. *Cardiovasc Res* 77(2):237–244
152. O'Rourke B, Kass DA, Tomaselli GF, Kääb S, Tunin R, Marbán E (1999) Mechanisms of altered excitation-contraction coupling in canine tachycardia-induced heart failure, I: experimental studies. *Circ Res* 84(5):562–570
153. Ostap EM (2002) 2,3-Butanedione monoxime (BDM) as a myosin inhibitor. *J Muscle Res Cell Motil* 23(4):305–308
154. Oudit GY, Kassiri Z, Sah R, Ramirez RJ, Zobel C, Backx PH (2001) The molecular physiology of the cardiac transient outward potassium current (I_{to}) in normal and diseased myocardium. *J Mol Cell Cardiol* 33(5):851–872
155. Papazian DM, Schwarz TL, Tempel BL, Jan YN, Jan LY (1987) Cloning of genomic and complementary DNA from Shaker, a putative potassium channel gene from *Drosophila*. *Science* 237(4816):749–753
156. Pastore JM, Girouard SD, Laurita KR, Akar FG, Rosenbaum DS (1999) Mechanism linking T-wave alternans to the genesis of cardiac fibrillation. *Circulation* 99(10):1385–1394
157. Pavlovi D, Fuller W, Shattock MJ (2007) The intracellular region of FXYD1 is sufficient to regulate cardiac Na/K ATPase. *FASEB J* 21(7):1539–1546
158. Pavlovic D, McLatchie LM, Shattock MJ (2010) The rate of loss of T-tubules in cultured adult ventricular myocytes is species dependent. *Exp Physiol* 95(4):518–527

159. Periasamy M, Kalyanasundaram A (2007) SERCA pump isoforms: their role in calcium transport and disease. *Muscle Nerve* 35(4):430–442
160. Perrin MJ, Subbiah RN, Vandenberg JI, Hill AP (2008) Human ether-a-go-go related gene (hERG) K⁺ channels: function and dysfunction. *Prog Biophys Mol Biol* 98(2-3):137–148
161. Picht E, DeSantiago J, Blatter LA, Bers DM (2006) Cardiac alternans do not rely on diastolic sarcoplasmic reticulum calcium content fluctuations. *Circ Res* 99(7):740–748
162. Picht E, Zima AV, Blatter LA, Bers DM (2007) SparkMaster: automated calcium spark analysis with ImageJ. *Am J Physiol Cell Physiol* 293(3):C1073–C1081
163. Pieske B, Maier LS, Bers DM, Hasenfuss G (1999) Ca²⁺ handling and sarcoplasmic reticulum Ca²⁺ content in isolated failing and nonfailing human myocardium. *Circ Res* 85(1):38–46
164. Postma AV, Denjoy I, Hoorntje TM, Lupoglazoff JM, Costa AD, Sebillon P, Mannens MMAM, Wilde AAM, Guicheney P (2002) Absence of calsequestrin 2 causes severe forms of catecholaminergic polymorphic ventricular tachycardia. *Circ Res* 91(8):e21–e26
165. Pracyk JB, Tanaka K, Hegland DD, Kim KS, Sethi R, Rovira II, Blazina DR, Lee L, Bruder JT, Kovcsdi I, Goldshmidt-Clermont PJ, Irani K, Finkel T (1998) A requirement for the Rac1 GTPase in the signal transduction pathway leading to cardiac myocyte hypertrophy. *J Clin Invest* 102(5):929–937
166. Pugsley MK, Authier S, Curtis MJ (2008) Principles of Safety Pharmacology. *British Journal of Pharmacology* 154:1382–1399
167. Qian YW, Sung RJ, Lin SF, Province R, Clusin WT (2003) Spatial heterogeneity of action potential alternans during global ischemia in the rabbit heart. *Am J Physiol Heart Circ Physiol* 285(6):H2722–H2733
168. R Mirzoyan MT M Laatiaouia (2006) Very high quantum efficiency PMTs with bialkali photocathode. *Nuclear Instruments and Methods in Physics Research A* 567:230–232
169. Rang HP (2006) The receptor concept: pharmacology's big idea. *Br J Pharmacol* 147 Suppl 1:S9–16
170. Reeves JP, Condrescu M, Chernaya G, Gardner JP (1994) Na⁺/Ca²⁺ antiport in the mammalian heart. *J Exp Biol* 196:375–388

171. Reil JC, Hohl M, Oberhofer M, Kazakov A, Kaestner L, Mueller P, Adam O, Maack C, Lipp P, Mewis C, Allessie M, Laufs U, Böhm M, Neuberger HR (2010) Cardiac Rac1 overexpression in mice creates a substrate for atrial arrhythmias characterized by structural remodelling. *Cardiovasc Res* 87(3):485–493
172. Remme CA, Bezzina CR (2010) Sodium channel (dys)function and cardiac arrhythmias. *Cardiovasc Ther* 28(5):287–294
173. Roden DM (2006) Long QT syndrome: reduced repolarization reserve and the genetic link. *J Intern Med* 259(1):59–69
174. Roden DM, Balsler JR, George AL, Anderson ME (2002) Cardiac ion channels. *Annu Rev Physiol* 64:431–475
175. Roden DM, Hoffman BF (1985) Action potential prolongation and induction of abnormal automaticity by low quinidine concentrations in canine Purkinje fibers. Relationship to potassium and cycle length. *Circ Res* 56(6):857–867
176. Rosenbaum DS, Jackson LE, Smith JM, Garan H, Ruskin JN, Cohen RJ (1994) Electrical alternans and vulnerability to ventricular arrhythmias. *N Engl J Med* 330(4):235–241
177. Rossi D, Barone V, Giacomello E, Cusimano V, Sorrentino V (2008) The sarcoplasmic reticulum: an organized patchwork of specialized domains. *Traffic* 9(7):1044–1049
178. Rossi D, Sorrentino V (2002) Molecular genetics of ryanodine receptors Ca^{2+} -release channels. *Cell Calcium* 32(5-6):307–319
179. Rubart M, Wang E, Dunn KW, Field LJ (2003) Two-photon molecular excitation imaging of Ca^{2+} transients in Langendorff-perfused mouse hearts. *Am J Physiol Cell Physiol* 284(6):C1654–C1668
180. Sakai R, Repunte-Canonigo V, Raj CD, Knöpfel T (2001) Design and characterization of a DNA-encoded, voltage-sensitive fluorescent protein. *Eur J Neurosci* 13(12):2314–2318
181. Sakmann B, Neher E (1984) Patch clamp techniques for studying ionic channels in excitable membranes. *Annu Rev Physiol* 46:455–472
182. Salzberg BM, Davila HV, Cohen LB (1973) Optical recording of impulses in individual neurones of an invertebrate central nervous system. *Nature* 246(5434):508–509

183. Sanguinetti MC, Curran ME, Zou A, Shen J, Spector PS, Atkinson DL, Keating MT (1996) Coassembly of K_{VLQT1} and minK (IsK) proteins to form cardiac I_{Ks} potassium channel. *Nature* 384(6604):80–83
184. Sanguinetti MC, Jiang C, Curran ME, Keating MT (1995) A mechanistic link between an inherited and an acquired cardiac arrhythmia: HERG encodes the I_{Kr} potassium channel. *Cell* 81(2):299–307
185. Sanguinetti MC, Tristani-Firouzi M (2006) hERG potassium channels and cardiac arrhythmia. *Nature* 440(7083):463–469
186. Sato TR, Gray NW, Mainen ZF, Svoboda K (2007) The functional microarchitecture of the mouse barrel cortex. *PLoS Biol* 5(7):e189
187. Satoh M, Ogita H, Takeshita K, Mukai Y, Kwiatkowski DJ, Liao JK (2006) Requirement of Rac1 in the development of cardiac hypertrophy. *Proc Natl Acad Sci U S A* 103(19):7432–7437
188. Semwogerere D, Weeks ER (2005) Confocal microscopy. *Encyclopedia of Biomaterials and Biomedical Engineering* :1–10
189. Shimizu W, Antzelevitch C (1999) Cellular and ionic basis for T-wave alternans under long-QT conditions. *Circulation* 99(11):1499–1507
190. Shou W, Aghdasi B, Armstrong DL, Guo Q, Bao S, Charrng MJ, Mathews LM, Schneider MD, Hamilton SL, Matzuk MM (1998) Cardiac defects and altered ryanodine receptor function in mice lacking FKBP12. *Nature* 391(6666):489–492
191. Shu J, Zhou J, Patel C, Yan GX (2009) Pharmacotherapy of cardiac arrhythmias—basic science for clinicians. *Pacing Clin Electrophysiol* 32(11):1454–1465
192. Shynkar VV, Klymchenko AS, Duportail G, Demchenko AP, Mély Y (2005) Two-color fluorescent probes for imaging the dipole potential of cell plasma membranes. *Biochim Biophys Acta* 1712(2):128–136
193. Siegel MS, Isacoff EY (1997) A genetically encoded optical probe of membrane voltage. *Neuron* 19(4):735–741
194. Simmerman HK, Jones LR (1998) Phospholamban: protein structure, mechanism of action, and role in cardiac function. *Physiol Rev* 78(4):921–947

195. SIPIDO KR, BITO V, ANTOONS G, VOLDERS PG, VOS MA (2007) Na/Ca Exchange and Cardiac Ventricular Arrhythmias. *Annals of the New York Academy of Sciences* 1099(1):339–348
196. Sjöblom B, Salmazo A, Djinovic-Carugo K (2008) α -actinin structure and regulation. *Cell Mol Life Sci* 65(17):2688–2701
197. Smith PL, Baukrowitz T, Yellen G (1996) The inward rectification mechanism of the HERG cardiac potassium channel. *Nature* 379(6568):833–836
198. Soeller C, Cannell MB (1999) Examination of the transverse tubular system in living cardiac rat myocytes by 2-photon microscopy and digital image-processing techniques. *Circ Res* 84(3):266–275
199. Soille P (1999) *Morphological Image Analysis: Principles and Applications*. Springer-Verlag
200. Song LS, Sobie EA, McCulle S, Lederer WJ, Balke CW, Cheng H (2006) Orphaned ryanodine receptors in the failing heart. *Proc Natl Acad Sci U S A* 103(11):4305–4310
201. Spector PS, Curran ME, Keating MT, Sanguinetti MC (1996) Class III antiarrhythmic drugs block hERG, a human cardiac delayed rectifier K⁺ channel. Open-channel block by methanesulfonanilides. *Circ Res* 78(3):499–503
202. Splawski I, Timothy KW, Sharpe LM, Decher N, Kumar P, Bloise R, Napolitano C, Schwartz PJ, Joseph RM, Condouris K, Tager-Flusberg H, Priori SG, Sanguinetti MC, Keating MT (2004) Ca_v1.2 calcium channel dysfunction causes a multisystem disorder including arrhythmia and autism. *Cell* 119(1):19–31
203. Stern MD, Pizarro G, Ríos E (1997) Local control model of excitation-contraction coupling in skeletal muscle. *J Gen Physiol* 110(4):415–440
204. Stølen TO, Høydal MA, Kemi OJ, Catalucci D, Ceci M, Aasum E, Larsen T, Rolim N, Condorelli G, Smith GL, Wisløff U (2009) Interval training normalizes cardiomyocyte function, diastolic Ca²⁺ control, and SR Ca²⁺ release synchronicity in a mouse model of diabetic cardiomyopathy. *Circ Res* 105(6):527–536
205. Straight AF, Cheung A, Limouze J, Chen I, Westwood NJ, Sellers JR, Mitchison TJ (2003) Dissecting temporal and spatial control of cytokinesis with a myosin II Inhibitor. *Science* 299(5613):1743–1747

206. Sussman MA, Welch S, Walker A, Klevitsky R, Hewett TE, Price RL, Schaefer E, Yager K (2000) Altered focal adhesion regulation correlates with cardiomyopathy in mice expressing constitutively active Rac1. *J Clin Invest* 105(7):875–886
207. Tada M, Toyofuku T (1998) Molecular regulation of phospholamban function and expression. *Trends Cardiovasc Med* 8(8):330–340
208. The MathWorks Inc (2009), corr2 - 2D correlation coefficient. MatLab R2009a Documentation, Image Processing Toolbox
209. The MathWorks Inc (2009), Imextendedmax, Extended-maxima transform. Image Processing Toolbox
210. Therien AG, Blostein R (2000) Mechanisms of sodium pump regulation. *Am J Physiol Cell Physiol* 279(3):C541–C566
211. Trudeau MC, Warmke JW, Ganetzky B, Robertson GA (1995) hERG, a human inward rectifier in the voltage-gated potassium channel family. *Science* 269(5220):92–95
212. Tsutsui H, Higashijima Si, Miyawaki A, Okamura Y (2010) Visualizing voltage dynamics in zebrafish heart. *J Physiol* 588(Pt 12):2017–2021
213. Tsutsui H, Ishihara K, Cooper G (1993) Cytoskeletal role in the contractile dysfunction of hypertrophied myocardium. *Science* 260(5108):682–687
214. Tsutsui H, Karasawa S, Okamura Y, Miyawaki A (2008) Improving membrane voltage measurements using FRET with new fluorescent proteins. *Nat Methods* 5(8):683–685
215. Undrovinas AI, Shander GS, Makielski JC (1995) Cytoskeleton modulates gating of voltage-dependent sodium channel in heart. *Am J Physiol* 269(1 Pt 2):H203–H214
216. van Oort RJ, Garbino A, Wang W, Dixit SS, Landstrom AP, Gaur N, De Almeida AC, Skapura DG, Rudy Y, Burns AR, Ackerman MJ, Wehrens XHT (2011) Disrupted junctional membrane complexes and hyperactive ryanodine receptors after acute junctophilin knockdown in mice. *Circulation* 123(9):979–988
217. Vandenberg JI, Walker BD, Campbell TJ (2001) HERG K⁺ channels: friend and foe. *Trends Pharmacol Sci* 22(5):240–246
218. Venetucci LA, Trafford AW, O'Neill S, Eisner DA (2007) Na/Ca Exchange: Regulator of Intracellular Calcium and Source of Arrhythmias in the Heart. *Annals of the New York Academy of Sciences* 1099(1):315–325

219. Viero C, Kraushaar U, Ruppenthal S, Kaestner L, Lipp P (2008) A primary culture system for sustained expression of a calcium sensor in preserved adult rat ventricular myocytes. *Cell Calcium* 43(1):59–71
220. Vogelstein JT, Watson BO, Packer AM, Yuste R, Jedynak B, Paninski L (2009) Spike inference from calcium imaging using sequential Monte Carlo methods. *Biophys J* 97(2):636–655
221. Volders PG, Vos MA, Szabo B, Sipido KR, de Groot SH, Gorgels AP, Wellens HJ, Lazzara R (2000) Progress in the understanding of cardiac early afterdepolarizations and torsades de pointes: time to revise current concepts. *Cardiovasc Res* 46(3):376–392
222. Vonesch C, Aguet F, Vonesch JL, Unser M (2006) The colored revolution of bioimaging. *IEEE Signal Processing Magazine* 23:20–31
223. Walker ML, Rosenbaum DS (2005) Cellular alternans as mechanism of cardiac arrhythmogenesis. *Heart Rhythm* 2(12):1383–1386
224. Wang L, Duff HJ (1997) Developmental changes in transient outward current in mouse ventricle. *Circ Res* 81(1):120–127
225. Wang Q, Curran ME, Splawski I, Burn TC, Millholland JM, VanRaay TJ, Shen J, Timothy KW, Vincent GM, de Jager T, Schwartz PJ, Toubin JA, Moss AJ, Atkinson DL, Landes GM, Connors TD, Keating MT (1996) Positional cloning of a novel potassium channel gene: KVLQT1 mutations cause cardiac arrhythmias. *Nat Genet* 12(1):17–23
226. Wang Q, Shen J, Splawski I, Atkinson D, Li Z, Robinson JL, Moss AJ, Towbin JA, Keating MT (1995) SCN5A mutations associated with an inherited cardiac arrhythmia, long QT syndrome. *Cell* 80(5):805–811
227. Wang SQ, Song LS, Lakatta EG, Cheng H (2001) Ca²⁺ signalling between single L-type Ca²⁺ channels and ryanodine receptors in heart cells. *Nature* 410(6828):592–596
228. Wang Z, Fermini B, Nattel S (1995) Effects of flecainide, quinidine, and 4-aminopyridine on transient outward and ultrarapid delayed rectifier currents in human atrial myocytes. *J Pharmacol Exp Ther* 272(1):184–196
229. Weber KT, Sun Y, Tyagi SC, Cleutjens JP (1994) Collagen network of the myocardium: function, structural remodeling and regulatory mechanisms. *J Mol Cell Cardiol* 26(3):279–292

230. Wehrens XHT, Lehnart SE, Reiken S, Vest JA, Wronska A, Marks AR (2006) Ryanodine receptor/calcium release channel PKA phosphorylation: a critical mediator of heart failure progression. *Proc Natl Acad Sci U S A* 103(3):511–518
231. Wehrens XHT, Lehnart SE, Reiken SR, Marks AR (2004) Ca^{2+} /calmodulin-dependent protein kinase II phosphorylation regulates the cardiac ryanodine receptor. *Circ Res* 94(6):e61–e70
232. Wei L, Hanna AD, Beard NA, Dulhunty AF (2009) Unique isoform-specific properties of calsequestrin in the heart and skeletal muscle. *Cell Calcium* 45(5):474–484
233. Wei S, Guo A, Chen B, Kutschke W, Xie YP, Zimmerman K, Weiss RM, Anderson ME, Cheng H, Song LS (2010) T-tubule remodeling during transition from hypertrophy to heart failure. *Circ Res* 107(4):520–531
234. Weinsberg F, Bauer CK, Schwarz JR (1997) The class III antiarrhythmic agent E-4031 selectively blocks the inactivating inward-rectifying potassium current in rat anterior pituitary tumor cells (GH3/B6 cells). *Pflugers Arch* 434(1):1–10
235. Wilson LD, Wan X, Rosenbaum DS (2006) Cellular alternans: a mechanism linking calcium cycling proteins to cardiac arrhythmogenesis. *Ann N Y Acad Sci* 1080:216–234
236. Woosley RL (1991) Antiarrhythmic drugs. *Annu Rev Pharmacol Toxicol* 31:427–455
237. Wu J, Biermann M, Rubart M, Zipes DP (1998) Cytochalasin D as excitation-contraction uncoupler for optically mapping action potentials in wedges of ventricular myocardium. *J Cardiovasc Electrophysiol* 9(12):1336–1347
238. Xu C, Ma H, Inesi G, Al-Shawi MK, Toyoshima C (2004) Specific structural requirements for the inhibitory effect of thapsigargin on the Ca^{2+} ATPase SERCA. *J Biol Chem* 279(17):17973–17979
239. Xu X, Yano M, Uchinoumi H, Hino A, Suetomi T, Ono M, Tateishi H, Oda T, Okuda S, Doi M, Kobayashi S, Yamamoto T, Ikeda Y, Ikemoto N, Matsuzaki M (2010) Defective calmodulin binding to the cardiac ryanodine receptor plays a key role in CPVT-associated channel dysfunction. *Biochem Biophys Res Commun* 394(3):660–666
240. Yaksi E, Friedrich RW (2006) Reconstruction of firing rate changes across neuronal populations by temporally deconvolved Ca^{2+} imaging. *Nat Methods* 3(5):377–383

241. Yamashita A, Maeda K, Maéda Y (2003) Crystal structure of CapZ: structural basis for actin filament barbed end capping. *EMBO J* 22(7):1529–1538
242. Yang F, Hanon S, Lam P, Schweitzer P (2009) Quinidine revisited. *Am J Med* 122(4):317–321
243. Yuan W, Ginsburg KS, Bers DM (1996) Comparison of sarcolemmal calcium channel current in rabbit and rat ventricular myocytes. *J Physiol* 493 (Pt 3):733–746
244. Zahradnikova A, Zahradnik I, Györke I, Györke S (1999) Rapid activation of the cardiac ryanodine receptor by submillisecond calcium stimuli. *J Gen Physiol* 114(6):787–798
245. Zahradnikova AZPZ (2007) Kinetics of calcium spikes in rat cardiac myocytes. *J Physiol* 578(Pt 3):677–691
246. Zalk R, Lehnart SE, Marks AR (2007) Modulation of the ryanodine receptor and intracellular calcium. *Annu Rev Biochem* 76:367–385
247. Zhou Z, Gong Q, Ye B, Fan Z, Makielski JC, Robertson GA, January CT (1998) Properties of hERG channels stably expressed in HEK-293 cells studied at physiological temperature. *Biophys J* 74(1):230–241
248. Zima AV, Blatter LA (2006) Redox regulation of cardiac calcium channels and transporters. *Cardiovasc Res* 71(2):310–321

Publications

During PhD period

1. **Tian Q**, Pahlavan S, Oleinikow K, Jung J, Ruppenthal S, Scholz A, Schumann C, Kraegeloh A, Oberhofer M, Lipp P, Kaestner L. Functional and morphological preservation of adult ventricular myocytes in culture by sub-micromolar cytochalasin D supplement. *J Mol Cell Cardiol.*, 2011. In press. Epub 2011 Sep 10.
2. **Tian Q**, Oberhofer M, Ruppenthal S, Scholz A, Buschmann V, Tsutsui H, Miyawaki A, Zeug A, Lipp P, Kaestner L. Optical Action Potential Screening on Adult Ventricular Myocytes as an Alternative QT-screen. *Cell Physiol Biochem.* 2011; 27(3-4):281-90. Epub 2011 Apr 1.
3. Kaestner L, **Tian Q**, Lipp P. Action potentials in heart cells. In: G. Jung (ed.) *Fluorescent Proteins II – from Fundamental Research to Bioanalytics*. Berlin, Heidelberg, New York: Springer, 2011. In press.
4. Kaestner L, **Tian Q**, Lipp P. Cardiac Safety Screens: Molecular, cellular and optical advancements. *Proc. SPIE.* 2011; 8089: 80890H.
5. Müller O, **Tian Q**, Zantl R, Kahl V, Lipp P, Kaestner L. A system for optical high resolution screening of electrical excitable cells. *Cell Calcium.* 2010; 47(3):224-33. Epub 2009 Dec 24.

During master degree period

1. **Tian Q**, Li J, Xie X, Sun M, Sang H, Zhou C, An T, Hu L, Ye RD, Wang MW. Stereospecific induction of nuclear factor-kappaB activation by isochamaejasmin. *Mol Pharmacol.* 2005 Dec;68(6):1534-42. Epub 2005 Sep 1.

Acknowledgment

Time elapsed silently without being caught. Fortunately, my life and my work went evenly in the last three years, which benefits greatly from the enthusiastic help of all people here:

First of all, Prof. Dr. Peter Lipp offered me the precious opportunity to be a PhD candidate in the university. During the entire PhD period, he gave me countless proposals and advices which ensured the advancements of all the projects as scheduled. Afterwards he helped me out in paper and thesis writing. Furthermore, he even helped a lot in experimental details.

Dr. Lars Kaestner contributed quite a lot in planning experiments, maintaining instruments and paper thesis writing. Besides the scientific help, he also helped me very much with my everyday life, some kind of life without any understanding of the native language: Deutsch.

Dr. Martin Oberhofer, Dr. Sandra Ruppenthal and Dr. Anke Scholz contributed important data and materials presented in this thesis, such as the electrophysiological data, the adenovirus of Mermaid and the actin staining data.

Dr. Andre Zeug helped me quite a lot with data fitting in MatLab.

Ms. Anne Vecerdea prepared almost all the cardiomyocytes used in the thesis. Ms. Tanja Kuhn contributed a lot in the preparation of molecular materials. Mr. Jörg Sauerbaum constructed all the custom-made mechanical devices used in this thesis. Ms. Karin Schumacher helped me a lot with official paperworks.

Dr. Oliver Müller, Mr. Xin Hui, Ms. Sara Pahlavan, Ms. Kathrina Wiesen, Mr. Benjamin Sauer, Mr. Jue Wang, Ms. Katharina Oleinikow and I shared very good cooperation with each other.

Now I would like to present my sincere gratitude to those people mentioned above. I would also like to present my appreciation for those people who had helped me but not listed here.

In the final, I would like to thank my parents and my sister. Without their support, it would be impossible to finish this thesis.

Attachments

A compact disk containing movies, programs and publications mentioned in this thesis is attached.

Movie list:

1. Figure 3.30: Fitting Example - Rat Ven Pixel-wise reconstructed (No Bgr).avi
2. Figure 3.30: Fitting Example - Rat Ven Pixel-wise reconstructed.avi
3. Figure 3.30: Fitting Example - Rat Ven Raw.avi
4. Figure 3.30: Fitting Example - Rat Ven Smoothn.avi
5. Figure 3.37: Ca-Mem-Overlay-FVBN.tif
6. Figure 3.37: Ca-Mem-Overlay-RacET.tif
7. Figure 3.37: FVBN Atrial Ca-Mem Overlay.avi
8. Figure 3.37: FVBN-RacET Ca Reconstruction.avi
9. Figure 3.37: FVBN-RacET Ca Reconstruction.tif
10. Figure 3.37: RacET Atrial Ca-Mem Overlay.avi
11. Figure 3.38: Rat Ven normal 1 over tau reproducibility.avi
12. Figure 3.38: Rat Ven normal amplitude reproducibility.avi
13. Figure 3.40: Ca Alternans - Severe, 1 over tau.avi
14. Figure 3.40: Ca Alternans - Severe, amplitude.avi
15. Figure 3.40: Ca Alternans - Slight, 1 over tau.avi

16. Figure 3.40: Ca Alternans - Slight, amplitude.avi
17. Figure 3.40: Ca Alternans Reconstruction Slight.avi
18. Figure 3.40: Ca Alternans Reconstruction, Severe.avi

Publication list:

1. Journal of Molecular and Cellular Cardiology 2011 (CytoD paper).pdf
2. Cell Physiol Biochem 2011 (Optical Action Potential Measurements).pdf
3. Book Chapter Online PDF (Action Potentials in Heart Cells).pdf
4. SPIE, 2011.01 (Cardiac safety screens).pdf
5. Cell Calcium 2010 (Müller et. al).pdf. A system for optical high resolution screening of electrical excitable cells.
6. Molecular Pharmacology 2005 (Isochamaejasmin induced NF-kB activation).pdf

Program/Macro list:

1. Calcium Confocal Linescan Analysis (Need MatLab 2009 or above.)
2. Caffeine data analysis (Need Igor Pro 6.0 or above.)
3. Contraction Analysis (Need Igor Pro 6.0 or above.)
4. F-actin Fourier Power Analysis (Need Igor Pro 6.0 or above.)
5. Imago Calcium Transient analysis (Need Igor Pro 6.2 or above.)
6. Optical AP duration analysis (Need Igor Pro 6.0 or above.)
7. PhotoMetry Data Analysis (Need Igor Pro 6.0 or above.)
8. Pixel-wise fitting (Need MatLab 2009 and dipimage toolbox.)
9. T-tubule Fourier Power Analysis (Need Igor Pro 6.0 or above.)